NANYANG TECHNOLOGICAL UNIVERSITY

SYNTHESIS AND TAILORING OF MULTIFUNCTIONAL LANTHANIDE NANOMATERIALS FOR NANOMEDICNE

ZHANG YAN

SCHOOL OF CHEMICAL AND BIOMEDICAL ENGINEERING

2012

SYNTHESIS AND TAILORING OF MULTIFUNCTIONAL LANTHANIDE NANOMATERIALS FOR NANOMEDICNE

ZHANG YAN

SCHOOL OF CHEMICAL AND BIOMEDICAL

ENGINEERING

A thesis submitted to the Nanyang Technological University
in partial fulfillment of the requirement for the degree of
Doctor of Philosophy

2012

ABSTRACT

The research work presented in this thesis focuses on the synthesis and tailoring lanthanide nanomaterials for nanomedicine, namely bio-imaging and cancer ablation. Owing to the sharp, intense up-conversion emission in wavelength ranging from ultra-violet to near-infrared, and unique magnetic properties, lanthanide doped nanomaterials have attracted strong research interests in nanomedicine.

Ytterbium enriched $NaYF_4$： Yb^{3+}, Er^{3+}/$NaDyF_4$: Yb^{3+} nanocrystals were first prepared as a powerful dual-mode contrast agent in fluorescence imaging and magnetic resonance imaging (MRI) by rational integration of different lanthanide ions within a single nanocrystal. The “poisonous” effect of Dy^{3+} on up-conversion emitters Er^{3+} has been successfully circumvented and the transverse relaxivities of the nanocrystals are much higher than other T_2 contrast agents, indicating their suitability as contrast agents in up-conversion fluorescence and MRI.

$NaDyF_4$:Yb^{3+}/ $NaGdF_4$:Yb^{3+}, Er^{3+} nanorods (NRs) were then synthesized. The NRs show excellent dark T_2 contrast enhancement due to the presence of Dy^{3+} ions. Interestingly, tunable positive and negative T_1 enhancement can be achieved by using different MRI sequences. They also show good up-conversion fluorescence, which indicate their potential as a new generation dual mode “smart” contrast agents in the area of optical/MRI bimodal imaging.

Near-UV and blue up-converting $NaYF_4$:Yb^{3+}, Tm^{3+} NCs have been optimized and further used to excited CdSe QDs in order to achieve tunable up-converting multicolor

emission in core-shell $NaYF_4$:Yb^{3+}, Tm^{3+}-CdSe nanocrystals. These nanocrystals are potential candidates as multicolor probes and contrast agents in imaging, fluorescence-based assay, optical barcodes for identifying analytes in multiplexed assays and chemosensing or biosensing. These nanocrystals open up new avenues as multicolor fluorescence in biolabeling in and biodetection applications.

Novel NIR-triggered N-TiO_2/$NaYF_4$:Yb^{3+},Tm^{3+} nanocomposites were synthesized. Their NIR-induced drug release and potential application in selective cancer cell killing have also been investigated. Under NIR laser irradiation, the NIR-to-Vis UCNPs ($NaYF_4$:Yb^{3+},Tm^{3+}) emit visible light (λ = 470 nm), which can excite N-doped TiO_2 to generate electron-hole pairs for redox reaction. A fluorescence dye, 7-methoxycoumarin-3-carboxylic acid, representing a model drug, was attached on the surface of N-TiO_2/$NaYF_4$:Yb^{3+},Tm^{3+} to investigate the NIR-triggered drug release. The current work also demonstrates that conjugating the NCs with anti-cAngptl4 antibody confer targeted anti-tumor property.

ACKNOWLEDGEMENTS

This thesis is an important milestone in my journey as a researcher. I could not achieve this without the support of many caring people. It is my great pleasure to extend my most sincere acknowledgement and gratitude to a number of people whose help, support and suggestions were immensely valuable in my research.

First and foremost, I would like to express my deepest gratitude to my supervisor, Asst/Prof. Timothy Tan and co-supervisor Dr Subramanian Tamil Selvan from the Institute of Materials Research and Engineering (IMRE) for their inexhaustible patience in providing help, support, encouragement and guidance to enhance my ability in research. I feel privileged to have the opportunity to work under their prudent supervision in one of the most exciting projects. Moreover, I would like to thank Asst/Prof Joachim Loo and Guo Jun from the School of Materials Sciences and Engineering for assisting with TEM characterization facilities. I am also thankful to Dr Kishore Bhakoo, Dr. Vimalan Vijayaragavan and Dr. Parasuraman Padmanabhan from the Singapore Bioimaging Consortium (SBIC) for their assistance in MRI measurements.

My special thanks to Dr Qingchi Xu and Ms Ziming He for their kind discussions and supports during these years. From them, I learned a lot which will be very useful for my research career. And of course, thanks to other members of my group

for their kind help and supports. Most importantly, a big thanks to all of my friends who have helped me in one way or another outside the graduate school during this period of study.

I also would like to thank the School of Chemical and Biomedical Engineering, Nanyang Technological University (NTU) for the award of a research scholarship.

Last but not least, a heartfelt gratitude goes to my family for their omnipresent love, trust and supports all through my life.

List of Publications

Journal Publications:

(1) **Zhang Y.**, Vijayaragavan V., Das G. K., BhaKoo K. K., Tan T. T. Y., *Single-Phase $NaDyF_4:Tb^{3+}$ Nanocrystals as Multifunctional Contrast Agent in High Field Magnetic Resonance and Optical Imaging,* European Journal of Inorganic Chemistry *(in press)*

(2) **Zhang Y.**, Vijayaragavan V., Padmanabhan P., Bhakoo K. K., Xu Q. C. Das G. K., Selvan S. T., Tan T. T. Y., *Tunable T_1-T_2 Contrast and Up-conversion Lanthanide Nanocrystals for Fluorescence and Magnetic Resonance Imaging.* (Submitted) (Chapter 5)

(3) **Zhang Y.**, Vijayaragavan V., Padmanabhan P., Guo J., Selvan S. T., Bhakoo K. K., Tan T. T. Y., *Dual Modal Ytterbium-Enriched Lanthanide Nanocrystals Prepared via a Two-step Synthesis for Efficient Up-converting Fluorescence and High Field T_2 Magnetic Resonance Imaging.* (Pending) (Chapter 4)

(4) **Zhang Y.**, Das G. K., Selvan S. T., Tan T. T. Y., *Color-Tunable Up-conversion Emission from Yb:Tm-codoped $NaYF_4$/CdSe Core-shell Nanocrystals.* (Patent pending) (Chapter 6)

(5) **Zhang Y.**, Xu Q. C., Rani K., Cleo C., Tan T. T. Y., N*ear Infrared-Induced Drug Release and Cancer Cell Killing on N-TiO_2/$NaYF_4$:Yb,Tm.* (US Provisional Application filed, manuscript submitted) (Chapter 7)

(6) Das G. K., **Zhang Y.**, D'Silva L., Padmanabhan P., Heng B. C., Loo J. S. C., Selvan S. T., Bhakoo K. K., Tan T. T. Y., *Single-Phase $Dy_2O_3:Tb^{3+}$ Nanocrystals*

as Dual-Modal Contrast Agent for High Field Magnetic Resonance and Optical Imaging. Chemistry of Materials **2011**, *23*, 2439-2446

(7) Janczewski D., **Zhang Y.**, Das G. K., Yi D. K., Padmanabhan P., Bhakoo K. K., Tan T. T. Y., Selvan S. T., *Bimodal Magnetic–Fluorescent Probes for Bioimaging.* Microscopy Research and Technique **2011**, *74*, 563-576

(8) Xu Q. C., Ng Y. H., **Zhang Y.**, Loo J. S. C., Amal R., Tan. T. T. Y., A *Three-way Synergy of Triple-Modified Bi_2WO_6/Ag/N-TiO_2 Nanojunction Film of Enhanced Photogenerated Charged Utilization*. Chemical Communications. **2011**, *47*, 8641-8643

Conference Proceedings

(1) Zhang Y., Das G. K., Selvan S. T., Tan T. T. Y., *Novel Lanthanide-based Nanoheterostructures for Imaging, Sensing and Catalytic Applications*, International Conference on Materials for Advanced Technologies **2011**, June 2011, Singapore.

(2) Zhang Y., Das G. K., Selvan S. T., Tan T. T. Y., *Reverse Micelles Synthesis and Characterization of Magnetic-luminescent Bifunctional Core/shell Nanocomposite*, The International Symposium on Advanced Bio, Nano, and Pharmaceutical Science and Technology **2009**, May 2009, Beijing, China.

(3) Zhang Y., Das G. K., Selvan S. T., Tan T. T. Y., *Up-converting Nanoparticles as Optical Imaging Nanoprobes and T_1, T_2 Magnetic Resonance Imaging Contrast Agent*, The International Symposium on Nanotechnology **2010**, May 2010, Singapore.

TABLE OF CONTENT

Chapter 1: Introduction 1

Chapter 2: Literature Review 9

2.1 Introduction 9

2.2 Lanthanide in MRI 13

2.2.1 Principle of MRI 13

2.2.2 Relaxation Mechanism 15

2.2.3 Contrast Agents in MRI 20

2.3 Lanthanides in Optical Imaging 25

2.3.1 Properties of fluorophores 25

2.3.2 Luminescence Mechanism 26

2.3.3 Down- and Up-conversion Fluorescence 28

2.3.4 The Luminescent Properties of Lanthanide Ions 30

2.3.5 Fluorescence Mechanism in Lanthanide Materials: Ion-ion Interactions. 32

2.3.6 Synthesis of Lanthanide NPs 35

2.4 Lanthanides in Multimodal Imaging 38

2.4.1 Lanthanide in MRI/optical Imaging Probes 38

2.4.2 Other Multimodality Contrast Agents 46

2.4.3 Therapeutic Applications of Lanthanide Multifunctional Nanomaterials 47

2.4.4 Design of Nanoparticles for Molecular Imaging 58

2.5 Motivations of This Work 63

Chapter 3: Synthesis Methodology and Characterization 65

3.1 Synthesis Methodology 65

3.1.1 Dual Modal Ytterbium-enriched Lanthanide Nanocrystals Prepared via a Two-step Synthesis for Efficient Up-converting Fluorescence and High Field T_2 Magnetic Resonance Imaging 65

3.1.2 A Strategy to Achieve Simultaneous Up-conversion Fluorescence and Tunable T_1-T_2 Magnetic Resonance Imaging Contrast in Lanthanide Nanocrystals 67

3.1.3 Color-tunable Up-conversion Emitting Yb,Tm Codoped $NaYF_4$/CdSe Core/shell Nanocomposites 70

3.1.4 Anti-cAngptl4 Ab-conjugated N-TiO_2/$NaYF_4$:Yb^{3+},Tm^{3+} Nanocomposite Near Infrared-Triggered Drug Release and Enhanced Targeted Cancer Cell Ablation 72

3.2 Characterization Techniques 76

3.2.1 Transmission Electron Microscopy (TEM) 76

3.2.2 Energy-dispersive X-ray (EDX) Analysis 77

3.2.3 Spectrofluorophotometer 78

3.2.4 Powder X-ray Diffraction (XRD) Analysis 78

3.2.5 Inductive Coupled Plasma-Atomic Emission Spectroscopy (ICP-AES) 81

3.2.6 Magnetic Resonance Imaging (MRI) 81

3.2.7 X-ray Photoelectron Spectroscopy (XPS) 82

3.2.8 Fourier Transform Infrared (FTIR) Spectroscopy 84

3.2.9 UV-Vis-NIR Diffuse Reflectance Spectra (DRS) 85

Chapter 4: Dual Modal Ytterbium-Enriched Lanthanide Nanocrystals for Efficient Up-converting Fluorescence and High Field T_2 Magnetic Resonance Imaging..... 86

4.1 Introduction 86

4.2 Results and Discussion 89

4.3 Conclusions 97

Chapter 5: A Strategy to Achieve Simultaneous Up-conversion Fluorescence and Tunable T_1-T_2 Magnetic Resonance Imaging Contrast in Lanthanide Nanocrystals98

5.1 Introduction 98

5.2 Results and Discussion 101

5.3 Conclusions 111

Chapter 6: Color-Tunable Up-conversion Emission from Yb,Tm Codoped $NaYF_4$/CdSe Core/shell Nanocrystals 113

6.1. Introduction 113

6.2 Results and Discussion 116

6.3 Conclusions 124

Chapter 7: Anti-cAngptl4 Ab-conjugated N-TiO_2/$NaYF_4$:Yb,Tm Nanocomposite Near Infrared-Triggered Drug Release and Enhanced Targeted Cancer Cell Ablation125

7.1 Introduction 125

7.2 Results and Discussion 127

7.3 Conclusions 140

Chapter 8: Conclusions and Recommendations 142

8.1 Conclusions 142

8.2 Recommendations 144

REFERENCES 150

LIST OF FIGURES

Figure 2.1 The major areas of nanomedicine…… ……..9

Figure 2.2 Schematic illustration of the inner sphere relaxation mechanism…….16

Figure 2.3 Schematic illustration of the outer sphere relaxation mechanism…….17

Figure 2.4 Structures of the commercially available Gd(III)-based contrast agents…… ..21

Figure 2.5 Mechanism of down-conversion and up-conversion fluorescence…...29

Figure 2.6 Dieke diagram for lanthanide ions……31

Figure 2.7 Ion-ion Interactions of fluorescence mechanism in lanthanides……...32

Figure 2.8 (1) Schematic illustration of the $NaYF_4$: Yb/Er (UCNP) NPs-based drug delivery system. (a) oleic acid capped $NaYF_4$: Yb/Er NPs; (b) Poly(maleic anhydride-alt-1-octadecene)-PEG-FA functionalized UCNPs; (c) DOX loading on $NaYF_4$: Yb/Er NPs; (d) Release of DOX from $NaYF_4$: Yb/Er NPs triggered by decreasing ph……...53

Figure 3.1 Bragg's law and the interaction of the X-rays with the atoms in crystal……..79

Figure 3.2 A scheme shows the principles of X-ray photoelectron spectroscopy……83

Figure 4.1 TEM images of $NaYF_4:Yb^{3+},Er^{3+}$ (A) and $NaYF_4:Yb^{3+},Er^{3+}/NaDyF_4:Yb^{3+}$ (B) NCs……90

Figure 4.2 EDS analysis of elemental composition of (A) $NaYF_4:Yb^{3+},Er^{3+}$ and (B) $NaYF_4:Yb^{3+},Er^{3+}/NaDyF_4:Yb^{3+}$ NCs……...90

Figure 4.3 XRD patterns of as-synthesized (A) β-$NaYF_4:Yb^{3+},Er^{3+}$ and (B) $NaYF_4:Yb^{3+},Er^{3+}/NaDyF_4:Yb^{3+}$……..91

Figure 4.4 UC luminescence spectra of $NaYF_4:Yb^{3+},Er^{3+}$ (A); $NaYF_4:Yb^{3+},Er^{3+}/NaDyF_4:Yb^{3+}$ (B); (Yb absent) $NaYF_4:Yb^{3+},Er^{3+}/NaDyF_4$ (C) and triple dopant $NaYF_4:Yb^{3+},Er^{3+},Dy^{3+}$ NCs following 980 nm excitation……..92

Figure 4.5 (A) Photograph shows the transparency of the $NaYF_4:Yb^{3+},Er^{3+}/NaDyF_4:Yb^{3+}$ NCs in hexane solution. The UC luminescence

photograph of a cuvetter showing green emission of $NaYF_4:Yb^{3+},Er^{3+}/NaDyF_4:Yb^{3+}$ (B); (Yb absent) $NaYF_4:Yb^{3+},Er^{3+}/NaDyF_4$ (C) and triple dopant $NaYF_4:Yb^{3+},Er^{3+},Dy^{3+}$ NCs at 980 nm excitation……..92

Figure 4.6 Proposed up-conversion mechanism in $NaYF_4:Yb^{3+},Er^{3+}$; $NaYF_4:Yb^{3+},Er^{3+}/NaDyF_4:Yb^{3+}$; $NaYF_4:Yb^{3+},Er^{3+}/NaDyF_4$ and triple dopant $NaYF_4:Yb^{3+},Er^{3+},Dy^{3+}$ NCs following 980 nm excitation……..94

Figure 4.7 T_2-weighted MR images of silanized $NaYF_4:Yb^{3+}$, $Er^{3+}/NaDyF_4:Yb^{3+}$ NCs in 1% agarose gel with increasing concentrations……..96

Figure 4.8 The transverse relaxivity (r_2) plot of $NaYF_4:Yb^{3+}$, $Er^{3+}/NaDyF_4:Yb^{3+}$ NCs obtained at various concentrations in 1% agarose gel…….97

Figure 5.1 (A) Schematic illustration of the general strategy to achieve tunable MRI T_1-T_2 contrast and Up-conversion Lanthanide Nanocrystals; (B) TEM images of $NaDyF_4:Yb^{3+}$ NCs and (C) $NaDyF_4:Yb^{3+}$/ $NaGdF_4:Yb^{3+},Er^{3+}$ NRs.…….....102

Figure 5.2 XRD patterns of as-synthesized $NaDyF_4:Yb^{3+}$ NRs (A) and $NaDyF_4:Yb^{3+}$ /$NaGdF_4:Yb^{3+}$, Er^{3+} NRs (B)……..103

Figure 5.3 The energy-dispersive X-ray spectroscopy (EDX) analysis of (A) $NaDyF_4$: Yb^{3+} and (B) $NaDyF_4:Yb^{3+}/NaGdF_4:Yb^{3+}$, Er^{3+} NRs……104

Figure 5.4 (1)Up-conversion fluorescence spectra of the (A) $NaGdF_4:Yb^{3+}$, Er^{3+}, (B) $NaDyF_4:Yb^{3+}/NaGdF_4:Yb^{3+}$, Er^{3+}; (C) Yb^{3+} absent $NaDyF_4/NaGdF_4:Yb^{3+}$, Er^{3+} and (D) triple dopant $NaGdF_4:Yb^{3+}$, Er^{3+}, Dy^{3+} NRs at the excitation of 980 nm, (2) Photographs of green emissions of the (A) $NaGdF_4:Yb^{3+}$, Er^{3+}; (B) $NaDyF_4:Yb^{3+}/NaGdF_4:Yb^{3+}$, Er^{3+}; (C) Yb^{3+} absent $NaDyF_4/NaGdF_4:Yb^{3+}$, Er^{3+} and (D) triple doped $NaGdF_4$: Yb^{3+}, Er^{3+}, Dy^{3+} NRs……106

Figure 5.5(A) Bright T_1–weighted images using a gradient echo sequence; (B) dark T_1–weighted images using a spin echo sequence and (C) T_2–weighted images of $NaDyF_4:Yb^{3+}/NaGdF_4:Yb^{3+}$, Er^{3+} NRs…….107

Figure 5.6(A) T_1 relaxivities of the $NaDyF_4:Yb^{3+}/NaGdF_4:Yb^{3+}$, Er^{3+} NRs using gradient echo sequence and spin echo sequence; (B) T_2 relaxivity plot of $NaDyF_4:Yb^{3+}/NaGdF_4:Yb^{3+}$, Er^{3+} NRs……108

Figure 6.1 a) Photograph of UC blue luminescence of $NaYF_4$: Yb^{3+},Tm^{3+} in hexane solution; b) Schematic illustration of the strategy to achieve multicolor tunable UC emission; c) Photographs of the multicolor emissions of core/shell $NaYF_4$: Yb^{3+},Tm^{3+}/CdSe NPs excited at 980 nm; d) Photographs of the multicolor emissions of core/shell $NaYF_4$: Yb^{3+},Tm^{3+}/CdSe excited at 365 nm; e) TEM image

and HRTEM (insert) of monodisperse $NaYF_4$: Yb^{3+},Tm^{3+} core NPs and (f) TEM image and HRTEM (insert) of monodisperse $NaYF_4$: Yb^{3+},Tm^{3+}/CdSe core/shell NPs……117

Figure 6.2 The energy-dispersive X-ray spectroscopy analyze of (A) $NaYF_4$: Yb^{3+},Tm^{3+} core and (B) $NaYF_4$:Yb^{3+},Tm^{3+}-CdSe core/shell NPs……118

Figure 6.3 XRD patterns of $NaYF_4$: Yb^{3+},Tm^{3+} core and $NaYF_4$: Yb^{3+},Tm^{3+}/CdSe core/shell NPs……119

Figure 6.4 Room temperature UC spectra of $NaYF_4$: 20% Yb^{3+}, 0.2–5 mol% Tm^{3+} NPs in cyclohexane solution (1 wt%) under 980 nm excitation……...120

Figure 6.5 Room temperature UC spectra of $NaYF_4$: 20-40%Yb^{3+}, 0.2% Tm^{3+} NPs dispersion in cyclohexane solution (1 wt%) under 980 nm excitation…….121

Figure 6.6 The UC emission of $NaYF_4$: Yb^{3+},Tm^{3+} (20%, 0.2%, blue line) core and $NaYF_4$: Yb^{3+},Tm^{3+}/CdSe core/shell NCs (green, yellow and red traces), excited at 980 nm. Insert: PL spectra of LnQD NCs excited at 365 nm……...122

Figure 6.7 Proposed energy transfer UC processes for the emission of $NaYF_4$: Yb^{3+}, Tm^{3+} core and subsequent energy transfer to CdSe……123

Figure 7.1 FTIR spectra of N-TiO_2; TGA-N-TiO_2; $NaYF_4$:Yb^{3+},Tm^{3+} and N-TiO_2/$NaYF_4$:Yb^{3+},Tm^{3+} NPs…….128

Figure 7.2 TEM images of the (a) $NaYF_4$:Yb^{3+},Tm^{3+} and (b) N-TiO_2/$NaYF_4$:Yb^{3+},Tm^{3+} NPs…….129

Figure 7.3 EDX pattern of the (a) $NaYF_4$:Yb^{3+},Tm^{3+} and (b) N-TiO_2/$NaYF_4$:Yb^{3+},Tm^{3+} NPs…….130

Figure 7.4 XRD spectra of TiO_2; N-TiO_2; $NaYF_4$:Yb^{3+},Tm^{3+} and N-TiO_2/$NaYF_4$:Yb^{3+},Tm^{3+} NPs…….131

Figure 7.5 N1s XPS spectra of N-TiO2……131

Figure 7.6 a) Room temperature UC emission spectra of: (A) $NaYF_4$:Yb^{3+},Tm^{3+}; (B) N-TiO_2/$NaYF_4$:Yb^{3+},Tm^{3+}; (C) N-TiO_2 NPs……..133

Figure 7.7 UV-Vis and NIR (inset) diffuse reflectance spectra of the N-TiO_2; $NaYF_4$:Yb^{3+},Tm^{3+} and N-TiO_2/$NaYF_4$:Yb^{3+},Tm^{3+} NPs……134

Figure 7.8 Spectra of the terephthalic acid solution containing N-TiO_2; $NaYF_4$:Yb^{3+},Tm^{3+} and N-TiO_2/$NaYF_4$:Yb^{3+},Tm^{3+} after NIR irradiation (120 min)……...134

Figure 7.9 (a) Variation in absorbance spectra of MB catalyzed by N-TiO_2/$NaYF_4$:Yb^{3+},Tm^{3+} NPs as a function of NIR irradiation time; (b) Comparison of the normalized concentration of MB decomposed by N-TiO_2; $NaYF_4$:Yb^{3+},Tm^{3+}; and N-TiO_2/$NaYF_4$:Yb^{3+},Tm^{3+} NPs under 980 nm NIR laser irradiation……..135

Figure 7.10 Fluorescence spectra of the 7-methoxycoumarin-3-carboxylic acid released from N-TiO_2/$NaYF_4$:Yb^{3+},Tm^{3+} NPs (a) before and (b) after 980 nm NIR irradiation……..136

Figure 7.11 FACS analysis of apoptotic A-5RT3 cells (Annexin V^+/PI^+ and Annexin V^+/PI^-) when treated with anti-cAngptl4 Ab nanoparticles and unconjugated nanoparticles, in and in the absence of NIR exposure…….....138

LIST OF TABLES

Table 2.1 The characteristics of every modality…….11

Table 2.2 Comparison of different types of fluorophore……27

Table 2.3 Comparison of the synthetic methods for lanthanide NPs…….38

Table 2.4 Typical strategies and surface molecules used for making hydrophilic NPs……..62

LIST OF SCHEMES

Scheme 7.1 Diagram showing the release principle of a fluorescent dye from the N-TiO_2/$NaYF_4$:Yb^{3+},Tm^{3+} NPs upon NIR irradiation……..128

Scheme 7.2 Proposed UC processes for the emission of $NaYF_4$: Yb^{3+}, Tm^{3+} core and subsequent energy transfer to N-TiO_2 under 980 nm NIR excitation……140

NOMENCLATURE

θ	diffraction angle
λ	wavelength
φ	work function
ω_0	larmor precession frequency
$\triangle\omega_M$	hydrogen chemical shift difference between Ln-bound water and free water
τ_M	residence time
τ_R	rotational correlation time
μ_0	external spin magnetic moment
μ_B	electron Bohr magneto
μm	micrometer
μs	microsecond
υ	frequency of light
A	angstrom
ANOVA	analysis of variance
APTMS	aminopropyl trimethoxysilane
B_0	external magnetic field
BE	binding energy
C	celcius or concentration of the paramagnetic center
CB	conduction band
CT	computed tomography
CNT	carbon nanotube
d	crystal plane distance
DC	down-conversion
DOX	doxorubicin
DMSO	dimethyl sulfoxide
DTPA	diethylenetriaminepentaacetate

e	electron
em	emission
ex	excitation
eV	electron volt
E	energy
E_b	binding energy
E_i	higher-energy singlet state (i^{th}) in energy level
E_{kin}	kinetic energy
EG	ethylene glycol
ET	energy transfer
EDS	energy dispersive X-ray spectroscopy
ESA	excited state absorption
ETU	energy transfer up-conversion
EDTA	ethylenediamine tetraacetic acid
FITC	fluorescein isothiocyanate
FTIR	fourier transformation infrared spectroscopy
FWHM	full width at half maximum of the diffraction peaks
g	gram
g_e	electron g factor
G	ground-state energy level
Gd	gadolinium
GE	gradient echo
GFP	green fluorescent protein
GSA	ground-state absorption
GSH	glutathione
h	hour or Planck's constant
H	applied magnetic field
HRTEM	high resolution transmission electron microscope

IS	inner spheres
IR	infra red
IBU	ibuprofen
ICP-AES	induction couple plasma-atomic emission spectroscopy
K	Kelvin or the Scherer constant
K_BT	thermal energy
K_{eff}	magnetic anisotropy constant
K_{ex}	exchange rate
L	total orbital angular momentum of the ion
Ln	lanthanide
LnQD	lanthanide/QDs
LPS	lipopolysaccharide
LSCM	laser scanning confocal microscopy
m	magnetic moment
mm	millimeter
M	magnetization
mM	millimolar
MB	methylene blue
MRI	magnetic resonance imaging
MSN	mesoporous silica NP
nm	nanometer
N_A	avogadro constant
NC	nanocrystal
NP	nanoparticle
NR	nanorod
NCT	neuron-capture therapy
NIR	near infrared-red
NMR	nuclear magnetic resonance

OS	outer sphere
PA	photon avalanche
PL	photoluminescence
PBS	phosphate buffer saline
PDT	photodynamic therapy
PEG	polyethylene glycol
PEI	polyethylenimine
PET	positron emission tomography
PTT	photothermal therapy
q	number of bound water molecules
QDs	quantum dots
QY	quantum yield
r_1	longitudinal relaxivity
r_2	transverse relaxivity
$R_{i(obs)}$	global relaxation rate of the aqueous system
RF	radio frequency
ROS	reactive oxygen species
S	spin
SE	spin echo
SAED	selected area electron diffraction
SPIO	superparamagnetic iron oxide
SWNH	single-wall carbon nanohorns
SPECT	single photon emission computed tomography
T	temperature
T_1	longitudinal relaxation time of water proton
T_2	transverse relaxation time of water proton
TE	echo time
TR	repetition time

TEM	transmission electron microscope
TGA	thioglycolic acid
TOP	trioctylphosphine
TOPO	trioctylphosphine oxide
UC	up-conversion
UV	ultraviolet
UCNP	up-conversion nanoparticle
VB	valence band
VIS	visible
W	watt
Xe	xenon
XPS	X-ray photoelectron spectroscopy
XRD	X-ray diffraction

Chapter 1: Introduction

Nanotechnology, the understanding and manipulating of matter at dimensions of roughly 1-100 nm, has been one of the most popular research frontiers in the past decades.[1] In nanomaterials, the distinct chemical and physical properties significantly differ from their corresponding bulk counterparts. As the size diminishes to the nanoscale, certain properties of matter become size-dependent, for example: optical property, conductivity, magnetism, surface energy and conductivity.[2] Therefore, nanomaterials have been actively studied for various optoelectronics, photovoltaics, communications and biomedical applications.[2-4]

In biomedical applications, these nanoscale materials are small enough to facilitate unique interactions with most biological components (e.g. viruses, proteins, DNA) at the molecular level.[5,6] In addition, these nanomaterials are able to detect diseases and deliver therapeutic agents to targeted cells through carefully design and engineering.[6,7] Currently, many researches is ongoing and significant achievements have been made in the field of molecular imaging, diagnostics, detection, drug discovery, delivery and cell/gene therapy, etc., showing their great potential in the emerging area known as nanomedicine.[5,8,9]

In nanomedicine, molecular imaging is important as it provides visualizing, characterizing and monitoring the abnormalities or biological processes at the molecular and cellular level.[8,10,11] It offers great potential in detecting molecular and cellular changes caused by the disease before the abnormalities are large enough to

cause change in the anatomic structure that can be detected by the imaging modalities. Various imaging modalities (e.g. positron emission tomography (PET), single photon emission computed tomography (SPECT), magnetic resonance imaging (MRI), optical, ultrasound) have been widely used clinically to understand and diagnose various diseases. MRI, for example, has become a powerful clinical imaging technique as it can provide greater topographic information of whole body and soft tissue contrast, therefore, distinguish pathological tissues from normal tissues.[12,13] It provides high spatial resolution and depth for *in vivo* imaging. Moreover, it is harmless to the patient as it is non-invasive, fast and avoids the use of ionizing radiation or radiotracers. However, it suffers from low sensitivity.[12,13] Optical imaging, on the contrary, has very high sensitivity but suffers from low tissue penetration depths.[14,15] Every imaging modality has its own advantages and disadvantages and no single technique possesses the full capacities to obtain comprehensive and accurate biological information. Hence, the combination of imaging modalities that integrates the strengths and offsets the deficiencies of individual modality is clearly attractive.

Contrast agents are generally used in imaging modalities to help identify particular biomarkers or pathways with high sensitivity and selectivity.[16] Although small molecules, such as organic dyes and radioisotopes conjugated to targeting ligands have been widely used as contrast agents in research and clinics, inorganic nanoparticles (NPs) are receiving increasing attention recently, because their properties can be easily adjusted by tailoring their composition, size, structure and shape in the same object.[8] A single material cannot realize multiple functions due to

the difference in their properties; therefore, integrating multiple components into a single NP by certain techniques, can afford multifunctional nanoplatform.[16-19] Multi- or bi-functional NPs, in which several different materials are combined at nanoscale, can not only show integrated properties of the original components but possess novel and collective performances not found in the original components. The development of multimodal contrast agents for *in vivo* imaging is growing rapidly. The pioneering work of Weissleder's group showed the formation of triple-label NPs combining near infra-red (NIR) fluorescent dyes on a dextran coated superparamagnetic iron oxide (SPIO) NPs, conjugated with diethylenetriaminepentaacetate (DTPA) chelate and PET tracer ^{64}Cu, forming a PET, MRI and NIR fluorescent detectable imaging agent.[20]

In particular, lanthanide NPs combining fluorescence and MRI have been under extensive investigation due to their potential applications as novel drug-delivery vehicles, imaging and therapeutic agents. Lanthanide ions, such as Gd^{3+}, Dy^{3+}, Pr^{3+}, Sm^{3+}, Ho^{3+} can alter the relaxation of water protons of the nearby tissues, which can be potentially applied as contrast agents in MRI.[21] MRI contrast agents fall into two categories, T_1 and T_2 contrast agents. T_1 contrast agents, include paramagnetic materials such as Gd-complex, Gd NPs, manganese oxide NPs. They normally induce brightness by shortening the longitudinal relaxation time (T_1). T_2 contrast agents, such as superparamagnetic iron oxide (SPIO) NPs, produce darken MR images by shortening of the transverse relaxation time (T_2) of the surrounding water protons.[21] Besides magnetism, lanthanides exhibit sharp and intense fluorescence owing to their shielded intra-4f electronic structure and energy levels.[22] They are extensively used as

optical markers. Lanthanide NPs exhibit several unique characteristics: (i) a much longer emission lifetime compared to other fluorescent agents such as dyes, fluorescent protein and QDs (μs to ms), which help to diminish spontaneous background fluorescence from the biological specimen; (ii) the emission intensity can be tuned by changing the type of host matrix, dopant and dopant concentration; (iii) multicolor luminescence can be easily realized by varying the dopant and host matrix. Moreover, unlike the size-dependent emission of QDs, the emission of lanthanide ions is not sensitive to particle size; (iv) up-conversion (UC) luminescence from Er^{3+}, Tm^{3+} and Ho^{3+} etc can be realized besides common down-conversion (DC) behavior.[22] UC fluorescence is a process that converts two or more low energy photons, usually NIR to high-energy emission through sequential absorption and energy transfer steps.[15,23-25] It provides tremendous advantages compared to DC emission when it comes to biomedical application, because: i) longer-wavelength NIR emissions are more efficient in penetrating the human tissue than visible light, therefore, resulting in significantly lower background autofluorescence from tissues. Other advantages of adopting UC fluorescence in bioimaging include reduced light scattering, photobleaching, and photodamage to biological specimens; ii) it allows *in vivo* observation with substantially high spatial resolution; iii) it can be induced by a low cost NIR diode laser source for the generation of simultaneous two-photon process by single wavelength excitation (980 nm).[23]

Several strategies have been reported to synthesize lanthanide magnetic-fluorescent NPs.[24] Examples include embedment of optical and MR imaging agents in a nanoscale

matrix, formation of heterodimers, and core-shell naonocrystals (NCs) for combined optical and MR imaging.[23] However, up to now, the development of multimodal lanthanide NPs is still in its infancy. Most reported multimodal contrast agents are SPIO-based NPs or Gd-conjugated NPs and most of them are used in a low magnetic field in MRI. NPs that possess both excellent contrast enhancement in high magnetic field and efficient UC properties in a single lanthanide-based NCs are highly-desirable. In addition, excitation in the ultraviolet (UV) region has significant drawbacks, such as strong background autofluorescence, low detection sensitivity, low light-penetration depth in tissue and high photodamage to the living organisms.[15] By choosing appropriate dopant, lanthanides NPs can be tuned to emit in the UV or blue region using NIR excitation. Tuning these emissions as excitation sources for other semiconductors is an interesting research direction with many potential applications, such as up-converting light emitting displays, biological imaging and cancer ablation.

In this study, we use sodium fluorides based NPs as the host matrix and aim to synthesize and tailor novel multifunctional lanthanide nanomaterials for nanomedicine, mainly for biological imaging and cancer cell ablation. This thesis is divided into the following sections. Following this chapter, a brief review will be presented in Chapter 2 on nanomedicine with the emphasis on molecular imaging and therapy. Advantages and limitations of each imaging modality will be presented, highlighting the benefits of MRI and optical imaging modalities. The use of lanthanides in MRI is reviewed, including the factors that can affect their relaxivities. Optical imaging, luminescence process and function of these lanthanide nanomaterials in optical imaging are

reviewed. Finally, lanthanides in multimodal imaging and their applications are discussed.

The preparation methods and basic principle of different materials characterization techniques used throughout the study are presented in Chapter 3.

In Chapter 4, a novel ytterbium-enriched lanthanide NPs is presented as dual mode contrast agents for optical and MR imaging. The overall aims of this study are: 1) to synthesize and tailor new types of contrast agents that are suitable for high magnetic field MR imaging; and 2) to achieve efficient UC fluorescence without compromising the MRI contrast enhancement. In a higher magnetic field, MRI sensitivity is increased; therefore, a higher spatial resolution, a better signal-to-noise ratio and reduced scan time can be achieved. The sensitivity of the as-synthesized contrast agents, namely r_2 value, is higher than that of existing ones, proving their efficiency as contrast agents in MRI. In addition, by growing an ytterbium-enriched secondary magnetic layer on the first layer, the UC fluorescence was found to significantly increase.

MRI contrast agents exhibit either T_1 positive or T_2 negative contrast enhancement. T_1 contrast agents depict anatomical details conserving high spatial resolution. The bright signal can be clearly detected and distinguished from other pathogenic or biological conditions. However, the bright signal they generated also suffers from some disadvantages, such as inducing artifacts in the bowel lumen.[26,27] T_2 contrast agents,

commonly magnetite NPs, generate dark contrast which is often confused with a low level MR signal arising from adjacent tissues such as bone or vasculature. [26] Recent studies have reported the synthesis of dual contrast T_1 and T_2 NPs that incorporate the benefits of both types of contrast agents in MRI.[26,28] In search for a new type of contrast agents that incorporates the unique features of trivalent lanthanide ions, a simple strategy has been undertaken to synthesize and tailor the lanthanide nanocrystals for both UC fluorescence and tunable T_1-T_2 dual mode contrast enhancement in MRI. To the best of our knowledge, this is the first work to demonstrate the possibility of embedding UC emitters into the lanthanide nanocrystals which can be tuned to achieve both positive and negative T_1 and negative T_2 properties, as well as UC fluorescence, in a single nanocrystal. Details of this work are presented in Chapter 5.

Chapter 6 presents color-tunable up-converting emission arisen from $NaYF_4$: Yb^{3+}, Tm^{3+}–CdSe core-shell nanocrystals. The key feature of this study is to achieve multicolor emission of QDs by tuning the UC emissions of $NaYF_4$: Yb^{3+}, Tm^{3+} NCs. The optimal UV and blue emission are used to excite the QDs to re-emit at various visible ranges. This system of lanthanide/QDs (LnQD) core/shell NCs offers numerous benefits such as high photochemical stability and high signal-to-noise detection. Multicolor emissions of NCs have found applications in light emitting displays, lasers, optoelectronic devices and biological imaging.

Chapter 7 reports the synthesis and application of NIR-triggered N-TiO_2/$NaYF_4$:Yb^{3+},Tm^{3+} NPs in drug release and cancer cell killing. Under NIR laser irradiation, the blue emissions from $NaYF_4$: Yb^{3+}, Tm^{3+} UCNPs are absorbed by N-doped TiO_2 to generate electron-hole pairs for redox reaction and their potential applications in triggered drug release and targeted cancer cells ablation are successfully demonstrated.

Lastly, Chapter 8 summarizes the major findings of this study, followed by recommendations for future work.

Chapter 2: Literature Review

2.1 Introduction

Nanomedicine is a discipline that applies nanotechnology to medicine. It involves the use of nanotechnology for imaging, monitoring, treatment and diagnosis of biological systems.[6] When the size of materials is scaled down to nano-range, their physical and chemical properties can significantly improve or change, which promise their unique medical effects, for example, the ability to cross biological barriers or the passive targeting of tissues.[5] Such medical effects are promising due to their abilities to overcome some of the limitations found in traditional therapeutic and diagnostic agents. Currently, there are a lot of ongoing efforts to design novel nanodevices capable of diagnosing and detecting diseases at their early stage.[6,7,16] The major areas in nanomedicine are summarized in Figure 2.1.

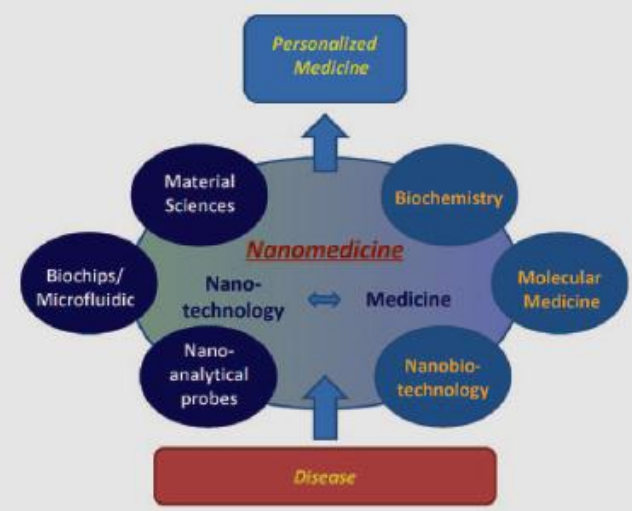

Figure 2.1 The major areas of nanomedicine.[7]

In these applications, molecular imaging and diagnostics are rapid growing research areas. Imaging modalities, such as PET, SPECT, MRI, CT, ultrasound, optical

imaging, have been developed and widely used as important tools to understand and diagnose various diseases.[16,29,30] The characteristics of these modalities have been summarized in Table 2.1. Each imaging modality has its own advantages and deficiencies and no single technique possesses the full capabilities to obtain comprehensive and accurate biological information. For example, MRI and CT have the advantages of exhibiting high spatial resolution and deep penetration depth; but they are limited by low sensitivity. Optical imaging, on the other hand, has shown high sensitivity in a non-invasive manner; but it suffers from limit penetration depth. By combining different imaging modalities into a single system, the strengths of every imaging modality are integrated while limitations are offset. For example, PET/CT is one of the well-known multimodal imaging techniques. The first PET/CT scanner developed in 1998 by Townsend and colleagues in collaboration with Siemens Medical was commercially available in 2001.[16] By 2003, PET/CT instruments were available from all major clinical instrument manufactures, namely GE, Philips, CTI and Siemens. Today, more than 95% of new PET scanners installed are PET/CT scanners. SPECT/CT was introduced commercially in 2004. PET/MRI instruments, which promise improved patient safety and imaging capacity over PET/CT, are also on the horizon.

Target specificity, non-invasiveness, high spatial resolution, three-dimensional tomography and real-time imaging are some of the important requirements for next-generation biomedical imaging technology. Therefore, the development of enhanced sensitivity, specificity and real-time imaging agents is crucial, not only to

Table 2.1 The characteristics of each modality[31]

Modality	Resolution	Depth	Cost	Time	Imaging agents
PET	1-2 mm	No limit	High	Minutes	Radioisotope (^{18}F, ^{64}Cu, ^{99m}Tc, ^{124}I);
SPECT	1-2 mm	No limit	High	Minutes	Radioisotope (^{18}F, ^{124}I, ^{64}Cu, ^{99m}Tc);
MRI	10-100 μm	No limit	High	Minutes-Hours	Paramagnetic ions (Gd^{3+}, Mn^{2+}); Paramagnetic NPs; Superparamagnetic NPs (Iron oxide)
Optical	1 μm	< 400 μm	Low	Seconds-Minutes	Organic dyes; Fluorescent protein; Lanthanide chelate; QDs; Lanthanide nanomaterials; Carbon nanotube;
CT	50 μm	No limit	Medium	Minutes	Iodine; Gadolinium; Gold NPs; Bismuth sulfide nanoplate;
Ultrasound	50 μm	mm	Medium	Minutes	Microbubble; Perfluorocarbon NPs;

understand the fundamental biological processes, but also to successfully diagnose various diseases. Inorganic NPs that have been developed to meet these demands have seen remarkable progress in molecular imaging in recent decades. Their nanosize and unique material properties allow the NPs to interact, monitor and trace biological

systems at the molecular level, making them useful as probes for biological diagnostics and therapeutics.

With the advent of multimodal imaging technology, the design and development of new functional molecular imaging probes are of great importance. Many possible combinations of imaging modalities result in different types of imaging contrast agents. Increasing number of work has been reported on the fabrication of different multimodal contrast agents. Examples include iron oxide NPs conjugated with dye molecules,[32,33] iron oxide/ QDs heterodimers,[34-37] and paramagnetic ion (Mn^{2+}) doped QDs.[38,39]

Lanthanide, a series comprising fifteen chemical elements in the periodic table from lanthanum to lutetium, have the general electronic structure, with minor exceptions, [Xe] $4f^n6s^2$ with n=0 (la) to 14 (lu), and their most stable oxidation state is +3 with a [Xe] $4f^n$ configuration.[40] These orbitals are shielded from the interaction with atom's environment by the 5s and 5p electrons. Consequently, they exhibit interesting magnetic and optical properties.

Since the main focus of the thesis is the synthesis and tailoring multifunctional lanthanide nanomaterials for nanomedicine, namely biological imaging and therapy, we will firstly review the principle and mechanism of MRI, highlighting the use of lanthanide materials in MRI; secondly, the use of lanthanide materials in optical imaging will be introduced, with an emphasis on the UC luminescence of lanthanide

nanomaterials. Methods to synthesize lanthanide NPs will also be reviewed. Thirdly, types of multimodal lanthanide fluorescent-magnetic NPs and other types of multimodal lanthanide NPs will be presented; and lastly their applications as drug delivery systems and imaging devices to increase the efficacy per dose of therapeutic or imaging contrast agents will be introduced.

2.2 Lanthanide in MRI

MRI is a prominent technique in diagnostic and biological research due to its greater soft tissue contrast, good depth penetration and higher resolution (as good as tens of micrometers for preclinical studies and ~ 1 mm for clinical studies without the use of ionizing radiation which are used in X-ray and CT scanning).[41] Therefore, it has been widely used for imaging brain and central nervous systems for assessing cardiac function and detecting abnormal tissues such as tumors. However, low sensitivity for the detection of targeted agents hampers its further usage in comparison with PET and SPECT. MRI is now becoming more popular as a non-invasive imaging modality, thanks to the recent development of powerful, innovative contrast agents.

2.2.1 Principle of MRI

MRI relies on the magnetic properties of hydrogen atoms in water, one of the most abundant atoms in human body. When an external magnetic field is applied to these protons which are oriented in random direction, they align with the external magnetic field. They can align either along or opposite to the magnetic field. The oriented spins remain constant and form net magnetization. The magnetization can be disturbed from

its equilibrium state using a radio frequency (RF) pulse. When the pulse is removed from the system, the protons realign to the equilibrium states and MRI machines measure these relaxation time. The contrast obtained in MR images is due to the differences in the density and relaxation time of water protons within the body. There are two types of relaxation time depending on different pulses used, namely, T_1 (longitudinal relaxation, the time taken for the protons to realign with the external magnetic field) and T_2 (transverse relaxation, the time taken for the protons to exchange energy with other nuclei).[21] MRI signal tends to increase with decreasing relaxation time T_1 and decrease with decreasing relaxation time T_2.

Contrast agents that can distinguish and enhance the difference between normal and malignant tissues have been used to increase MRI sensitivity and they can be divided into two categories: T_1 contrast agents and T_2 contrast agents. The signal enhancement of contrast agents depends on their relaxivity (r_1 and r_2), which is defined as the increase of relaxation rate ($r_1=1/T_1$; $r_2=1/T_2$) produced by 1 mmol per liter of contrast agent (unit: $s^{-1}mmol^{-1}$). The relaxivity is the main parameter considered in the development of an efficient contrast agent, and it depends on the size, chemical structure of a contrast agent molecule and on the accessibility of water molecules to the magnetic center.

$$R_{i(obs)} = 1/T_{i(obs)} = 1/T_{i(diam)} + r_i C;\ i = 1 \text{or } 2 \qquad \text{(Eq. 2.1)}$$

Where:

$R_{i(obs)}$ and $1/T_{i(obs)}$ = overall relaxation rate of the aqueous system (s^{-1})

$T_{i(diam)}$ = relaxation time of the system before addition of the contrast agent (s)

C = the concentration of the paramagnetic center ($mmol^{-1}$)

r_i = the relaxivity (s^{-1} $mmol^{-1}$)

The requirements for an ideal contrast agent in MRI are adequate relaxivity, susceptibility effects, tolerance, safety, low toxicity, stability, optimal biodistribution, and easy elimination. A lot of research is undergoing.

2.2.2 Relaxation Mechanism

2.2.2.1 Paramagnetic Relaxation

The paramagnetic relaxation is explained by two mechanisms: "inner spheres" (IS) and "outer sphere" (OS) relaxations.[21,42-44] The principle of "inner spheres relaxation", as shown in Figure 2.2, relies on a chemical exchange during one (or several) water molecule in contact with the electronic spins, leavening the first coordination sphere of the paramagnetic center replaced by other molecules (residence time τ_M). Gadolinium (Gd), a lanthanide element, has seven unpaired electrons and relatively long electronic relaxation time, rendering it favorable as the most extensively used element in MRI.

2.2.2.1.1 Inner Sphere Relaxivity

Inner sphere relaxation effectively controlled the relaxivity of a contrast agent at commonly used imaging field (0.5-1.5T).[21,42-44] The contribution of this relaxation is shown in the equation: [13]

$$R_{1P}^{IS} = \frac{Cq}{55.6} \frac{1}{T_{1M} + \tau_M} \qquad \text{(Eq. 2.2)}$$

Where:

IP subscript: inner paramagnetic effect

IS superscript: inner sphere relaxivity

C: molar concentration of paramagnetic compound

q: number of bound water molecules

T_{1M}: longitudinal relaxation time of the bound water protons

τ_M: Coordinated water residence time, slower tumbling of the contrast agents leads to faster relaxation rates, controlled by the molecular rotational correlation time

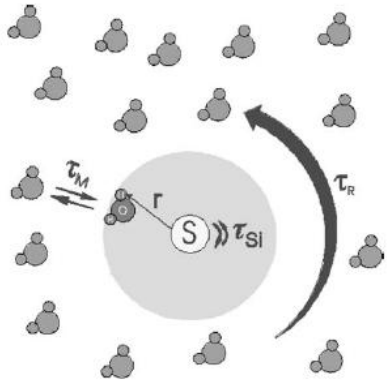

Figure 2.2 Schematic illustration of the inner sphere relaxation mechanism.[42]

From the above equation, it can be seen that hydration number, electron nuclear spin distance, water exchange, rotation and coordinated water residence time affect the relaxivities of contrast agents. With increasing the hydration number q, the

inner-sphere relaxivity is increased. However, it also decreases the thermodynamic stability. The distance between water proton and the unpaired electron spin (r) is difficult to measure and control. Rotation is probably the most critical variable in the equation. Slow rotation has been proven to improve relaxivity. Coordinated water residence time (τ_M) is based on an exchange between water molecules surrounding the complex and the water molecules coordinated to the lanthanide. Hence, the exchange rate ($K_{ex} = 1 / \tau_M$) is essential to understand the relaxation effect of the solvent. The details of this relaxation can be found in some excellent reviews.[21,27,45-47]

2.2.2.1.2 Outer Sphere Relaxivity

Contrast agents can display relaxivity even when q=0, as shown in Figure 2.3. This occurs by two mechanisms: second sphere relaxation and outer sphere relaxation. Second-sphere relaxation occurs when water molecules are in the second coordination spheres.[21,44,45] Outer-sphere relaxation arises due to diffusion of water molecules in the bulk near to the Gd(III) complex. However, separation of the two contributions is not so obvious, and sometimes the second spheres contribution is ignored.

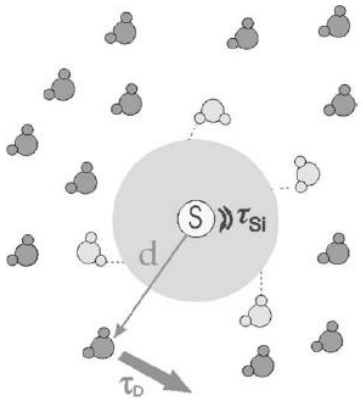

Figure 2.3 Schematic illustration of the outer sphere relaxation mechanism.[44]

2.2.2.2 Transverse Relaxation

Relaxation rate enhancement induced by a paramagnetic lanthanide compound is the sum of four different contributions – diamagnetic (R_{idia}), dipolar (R_{iD}), contact (R_{iC}), and curie (R_{iv}), as expressed in equation 2.3: [48]

$$R_i = R_{idia} + R_{iD} + R_{iC} + R_{iv} \; ; \; R_i = 1/T_i; \; i = 1; 2 \qquad \text{(Eq. 2.3)}$$

The diamagnetic contribution to the relaxation rate enhancement is usually negligible for water protons. The dipolar component is a spatial effect that is the result of dipolar coupling between the spin of the unpaired electrons of lanthanide ions and nuclear spins. It is described by the Solomon–Bloembergen–Morgan equations. The contact effect is transmitted through chemical bonds by scalar coupling between the unpaired electrons and the nuclear spins. The curie spin relaxation arises from the dipolar interaction of the nuclei with the thermal average of electron spin polarization (‘‘Curie Spin”). It becomes an important factor to the water relaxivity when used in high magnetic field. Molecules must be virtually immobile during the time T_{1e}, which require that $\tau_R >> T_{1e}$ (τ_R is the rotational correlation time). For dysprosium (Dy^{3+}) ions, they have high magnetic moment and its τ_R is always much larger than T_{1e}, therefore, the relaxation process induced by the Curie moments is unaffected by the electronic relaxation time and becomes important.[48]

In Dy^{3+}, the inner sphere terms for transverse relaxivity is given by: [48]

$$R_2^{IS} = fq\frac{1}{\tau_M}\frac{\frac{1}{T_{2M}^2} + \frac{1}{\tau_M T_{2M}} + \Delta\omega_M^2}{\left(\frac{1}{\tau_M} + \frac{1}{T_{2M}}\right)^2 + \Delta\omega_M^2}. \qquad \text{(Eq. 2.4)}$$

Where:

$T_{2M} = 1/ R_{2M}$ (transverse relaxation rate of the Ln^{3+} coordinated water) ($R_{2M} = R_{2D} + R_{2\chi}+R_{2C}$)

$\triangle\omega_M$: the hydrogen chemical shift difference between Ln-bound water and free water

At low magnetic fields, where $\tau_M\triangle\omega^2 << 1/ T_{2M}$ and $\tau_M\triangle\omega^2 << 1$, the above equation can be written as:

$$R^{IS}_2 = fqR_{2M} \qquad \text{(Eq. 2.5)}$$

At intermediate or high magnetic field, the relaxivity is dominated by the water exchange mechanism, where:

$$R^{IS}_2 = fq/\tau_{2M} \qquad \text{(Eq. 2.6)}$$

The slow water exchange holds a limit, where $\tau_{2M} >> T_{2M}$ and $R^{IS}_2 = R^{IS}_1$

The transverse relaxivity also has an outer-sphere contribution (R^{os}_2), consisting of a dipolar term (R^{os}_{2D}) and a curie term (R^{os}_{2D}). [48]

Currie law is written as: [49]

$$X_M = \mu_0 N_A \mu^2_B g^2_e * S(S+1) / 3KT \qquad \text{(Eq. 2.7)}$$

Where:

X_M: the intensity of magnetization

μ_0: The external spin magnetic moment

N_A: Avogadro constant

μ_B: The electron Bohr magnetic moment

g_e: the electron g factor

S: spin

T: temperature

The longitudinal relaxivity of Dy^{3+} complex increases with increasing magnetic field strength due to the Curie mechanism, but even at the highest field strengths in MRI, it is still significantly lower than the r_1 of commercial Gd^{3+} complex. Therefore, Dy^{3+} compounds are mainly used as T_2 contrast agents in MRI.

2.2.3 Contrast Agents in MRI

2.2.3.1 Positive Contrast Agents

Positive contrast agents include gadolinium or manganese based chelates or NPs. These contrast agents have unpaired electrons which give them paramagnetic properties. Most of the Gd^{3+} complexes are chelated with some ligands to reduce the toxicity of the metal. Of the six clinically approved contrast agents used worldwide for intravenous administration, four of them are Gd-based chelates.[21] Figure 2.4 shows these four Gd based positive contrast agents. Gd-DTPA complex, for example, has found applications in detecting the disruption of the blood brain barrier and the degree of vascularity, flow dynamics and vascular perfusion.

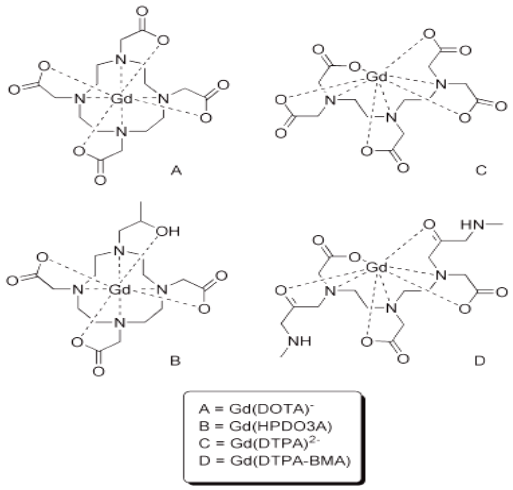

Figure 2.4 Structures of the commercially available Gd(III)-based contrast agents.[21]

Despite the significant achievements in the development of Gd-chelate, Gd (III) based NPs are now ardently pursued. They exhibit stronger ability of positive contrast enhancement, better pharmacokinetic parameters and a better control of biodistribution than those of Gd complexes. Gadolinium (III) possesses seven unpaired electrons, and they execute efficient exchange of magnetic fields with surrounding water protons, hence, efficiently alter the relaxation times of surrounding protons. Increasing the number or concentration of Gd(III) ions in the nanoparticles will greatly increase their ability to exchange magnetic field with the protons, and hence leading to the improvement of the relaxation. Gd complexes or Gd ions encapsulated into high-density lipoprotein NPs,[50-52] or polymeric NPs,[47,53] zeolites,[54-56] fullerenes,[57,58] carbon nanotubes (CNTs),[59] mesoporous silica NPs,[60-62] quantum dots (QDs),[63,64] chitosan particles,[65] and gold NPs[66,67] were synthesized and studied. They are all characterized by an increase of the molecular weight and of the amount of Gd(III) ions per contrast agent. As a consequence of their structure, some of them

were easily functionalized by biotargeting groups and/or fluorescent molecules, rendering them additional attractive features. Inorganic gadolinium based NPs, such as gadolinium oxide (Gd_2O_3), gadolinium fluoride NPs, and gadolinium carbonate, have been recently investigated.

Roberts and Watkins were amongst the first to study Gd_2O_3 NPs, revealing their potential as positive contrast agents in MRI.[68] Later, Tillement's group used a polyol route to synthesize Gd_2O_3 NPs and functionalized them with a PEGylated polysiloxane shell.[69] The NPs could be traced after intravenous injection into mice and rats by fluorescence imaging (due to Cyanine 5 covalently bound to the polysiloxane network) and MRI (due to the presence of Gd(III) ions). *In vivo* imaging experiments revealed that the particles freely circulated in the bloodstream without undesirable non-specific accumulation in liver, spleen and lungs. Moreover, these NPs were rather quickly removed from body by renal excretion, revealed that the NPs were safe for *in vivo* MRI. Gd_2O_3 NPs in CNTs were obtained after thermal treatment of gadolinium acetate entrapped in single-wall carbon nanohorns (SWNHs).[70] It induced a significant positive contrast enhancement in T_1-weighted images of the phantoms.

Superparamagnetic hollow and paramagnetic porous Gd_2O_3 NPs were synthesized using gelatin particles as shape and structure directors.[71] Hollow spheres produced better positive contrast enhancement (r_1 = 17.7 $mM^{-1}s^{-1}$ and r_2/r_1 = 1.50) than porous particles did (r_1 = 16.8 $mM^{-1}s^{-1}$ and r_2/r_1 = 1.87). These NPs were promising for drug encapsulation for controlled drug release during magnetic delivery. Yet in another

study, the same group synthesized $Gd_2O(CO_3)_2 \cdot H_2O$/silica/Au hybrid particles for MR imaging and photothermal destruction of cancer cells.[72] *In vitro* T_1-weighted MRI measurement showed that the relaxivity r_1 of NPs increased as the Au shell thickness decreased. In addition, the Au shell thickness also strongly influenced the NIR optical absorption and photothermal effect. At a fixed particle number, particles with a 63 nm Au shell exhibited the best photothermal performance. When the particle weight was fixed, 12 nm Au shell particles led to the optimum photothermal cancer destruction. Therefore, $Gd_2O(CO_3)_2 \cdot H_2O$/silica/Au hybrid particles are promising as a combined MR imaging and therapeutic agent.

Lanthanide ions, such as Tb, Eu, Er, Ho and Tm, show excellent fluorescence; therefore, many research groups doped or encapsulated Gd ions into the lanthanide NPs, which function as multimodal imaging agents. This will be further discussed in section 2.4.

2.2.3.2 Negative Contrast Agents

Negative contrast agents include SPIO NPs and dysprosium (Dy) chelates or NPs. SPIO NPs are the only clinically used nanoparticulate contrast agents up to now. Though SPIO NPs represent the classic T_2 contrast agent, we focus on the review of lanthanide Dy (III) complex or NPs as negative contrast agents.

Vymazal and coworkers studied transverse relaxation of Dy-DTPA-BMA (Dy-diethylenetriaminepentaacetic acid-bis[methylamide]) and Dy-PL-DTPA (Dy-

poly-L-lysine- diethylenetriaminepentaacetic acid) under magnetic field of 0.04-1.5T.[73] And their r_2 relaxivity increased with the field strength but was still very small at this field range. Bulte and coworkers had also presented an interesting study of the relaxivity of 5 ammonia-core polyamidoamine (PAMAM) dendrimer linked to the bi-functional Dy^{3+} complex (Dy-DOTA-PAMAM) in the same magnetic field range.[74] This is a macromolecular ligand with molecular weight of 21.6 kDa, and thus had a longer half-life in blood than low molecular weight Dy-DOTA and Dy-DTPA chelates. Furthermore, the measured transverse relaxivity (r_2) of Dy-DOTA-PAMAM is higher than those of Dy-DOTA and Dy-DTPA. The relatively high r_2 of Dy-DOTA-PAMAM compared to that of low molecular weight Dy chelates can be ascribed to its longer s_R, which is the main element of the curie spin contribution. Water-soluble endohedral fullerenols with a lanthanide ion trapped inside [$Ln@C_{82}(OH)_n$] have also been proposed as contrast agents in MRI, although Ln^{3+} ions in the fullerenol cages do not contact directly with water.[75] Among these metallofullerenols, $Dy@C_{82}(OH)_n$ shows a relatively large effect on transverse proton relaxivity (r_2 = 20 mM^{-1} s^{-1} at 9.4 T), which also increases with increasing external magnetic field. This effect is ascribed to the outer sphere curie mechanism.

Although Dy^{3+} ions are highly suitable as negative contrast agents, relatively high dosage of these complexes is required for inducing sufficient negative contrast enhancement. Their biocompatibility (reduced toxicity and particle uptake by organism) remains a challenging issue. Furthermore, the balancing of factors (the chemical shift, the residence time, particle size, surface charge density, etc) in order to

optimize r_2 is required for further usage of Dy^{3+} complex. Fine tuning these parameters may lead to promising contrast agents for high field MRI. The use of the Dy^{3+} compounds as negative contrast agents is still new, thus more work needs to be done.

2.3 Lanthanides in Optical Imaging

Optical imaging, which is based on the detection of light photons after their interaction with the tissue, has been used in biomedical diagnostics for years. It provides high sensitivity for detection in non-radiative manner and imaging instruments are relatively cheap and easy to use. However, its limitations include short penetration depth and scattering of light in the tissue.[76] Therefore, the development of different fluorophores, compounds that are designed to improve the sensitivity of detection, is clearly important. A wide variety of fluorophores for bioimaging is available nowadays. Organic dyes, fluorescent proteins, and lanthanide chelates are conventional fluorophores, which are still the most commonly used fluorescent labels. Novel inorganic fluorophores, such as quantum dots (QDs) and lanthanide-doped inorganic NPs, have gained tremendous interests due to their unique properties.

2.3.1 Properties of fluorophores

Organic dyes, such as fluorescein isothiocyanate (FITC), rhodamine, were used for fluorescence labeling due to their advantageous properties such as small size, easy attachment to biomolecules and high quantum yield. However, their low photostability hinders long term monitoring and excitation and emission spectra for some organic

dyes were overlapped.[76] Fluorescent protein provides the advantages of being able to genetically fuse to the protein of interest so that the protein can be tracked in real time. But their limitations include low quantum yield and low fluorescence lifetime.[24] Lanthanide-chelates have been investigated as commonly used imaging probes. However, water molecules or hydroxyl groups tend to quench the fluorescence of lanthanide ions when embedded in chelates. [24]

Novel inorganic fluorophores, including QDs and lanthanide-doped inorganic NPs, on the contrary, have the potential to overcome the problems of the above fluorophores. QDs exhibit good fluorescence quantum yield (QY) with narrow emission spectrum. However, they have limitations such as photoblinking and high cytotoxicity.[76] Lanthanide NPs have many superior properties compared to their predecessors. They exhibit unique characteristics: (i) a much longer emission lifetime (up to μs to ms); (ii) tunable emission intensity by control of host matrix, dopant and dopant concentration; (iii) multicolor luminescence by simply varying the lanthanide dopant and host matrix; (iv) up-conversion (UC) luminescence from Er^{3+}, Tm^{3+} and Ho^{3+} can be realized besides common down-conversion (DC) behavior. The advantages and limitations of the above-mentioned fluorophores are summarized in Table 2.2.

2.3.2 Luminescence Mechanism

When a fluorophore is excited by quanta of specific energy, electrons are transferred from a ground state (G) to a higher energy state (i.e. E_1, E_2). The excited electron can relax by various competing pathway. It can undergo non-radiative relaxation, in which

the excitation energy is dissipated as heat or by emitting a photon of lower energy. In the later case, fluorescence takes place.

Table 2.2 Comparison of different types of fluorophore [76]

Types of fluorophores	Advantages	Limitations
Organic Dyes	Ease of attachment to biomolecules; High absorptivity; High fluorescent QY; Excellent solubility in water;	Susceptible to photobleaching; Broad emission spectrum; Low photostability; PH sensitivity;
Green Fluorescence Protein (GFP)	Easy modulation to the environment; Capability to be expressed *in situ;* Trackable in real time	Low quantum yield; Low fluorescence lifetime; Potential cellular toxicity; Short time blinking;
Lanthanide Chelates	Tunable emissions; Long life time; Sharp emission spectra; Large stokes shifts; High quantum yield;	Photochemical instability; Quenching due to the ligands;
Quantum Dots (QDs)	Excellent sensitivity and stability; Stable; Multicolor emission; Low autofluorescences; Suitable for *in vitro* detection	Cytotoxicity; Surface modifications needed to render them biocompatible; Photoblinking;
Lanthanide doped NPs	Multicolor emission; Low toxicity; UC fluorescence at NIR excitation; Deep penetration depth; Long fluorescence lifetimes; Sharp emission spectra;	Applications of lanthanide doped NPs is yet in its infancy and more works need to be done

The excitation and emission process can be written:

Excitation: $G + hc_{ex} \rightarrow E_i$ (i= 1, 2, 3……) (Eq. 2.8)

Emission (fluorescence): $E_i \rightarrow G + h\upsilon_{ex}$ (Eq. 2.9)

Where:

hυ: a generic term for photon energy

h : planck's constant

υ: frequency of light (The specific frequencies of exciting and emitted light are dependent on the particular system)

G: the ground state

E: the excited state

2.3.3 Down- and Up-conversion Fluorescence

The difference between the position of the band maxima of the excitation and emission spectra of the same electronic transition is known as the Stokes's shift. A fluorescence emission can be either of Stoke's (DC) or anti-Stoke's type (UC).[77] The mechanism of UC and DC is depicted in Figure 2.5.

DC fluorescence occurs when the energy of the emitting photon is lower than that of an exciting photon, which follows the principle of the Stokes's law. In other word, the input energy is higher than output energy. This principle is valid only when one excited ion system is considered. On the other hand, UC fluorescence is a process that converts two or more low energy photons, usually near infrared (NIR) to high-energy

emission through sequential absorption and energy transfer steps. It provides tremendous advantages over the DC emission when it comes to bioapplications, because: i) NIR excitation is more efficient in penetrating the human tissue than visible light, resulting in significantly lower background autofluorescence from tissues and reduced light scattering, photobleaching and photodamage to biological specimens are also expected in UC fluorescence; ii) *in vivo* observation with substantially high spatial resolution is allowed; iii) UC process can be induced by a low cost NIR diode laser source for the generation of simultaneous two-photon process by 980 nm excitation. Two-photon absorption (TPA) is the simultaneous absorption of two photons of identical or different frequencies in order to excite a molecule from one state (usually the ground state) to a higher energy electronic state. The energy difference between the involved lower and upper states of the molecule is equal to the sum of the energies of the two photons. Two-photon absorption is a third-order process several orders of magnitude weaker than linear absorption. It differs from linear absorption in that the strength of absorption depends on the square of the light intensity, thus it is a nonlinear optical process.

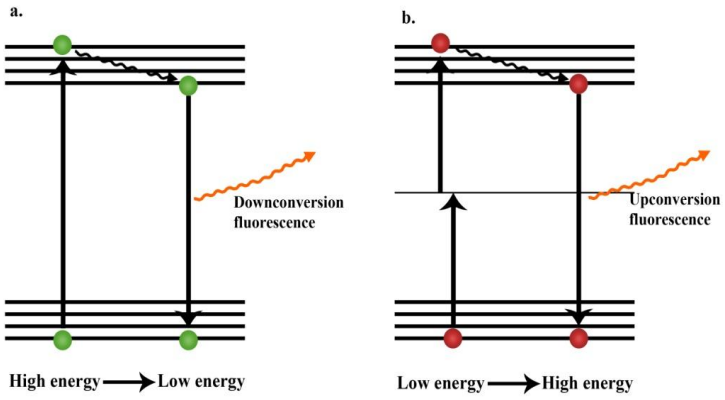

Figure 2.5 Mechanism of down-conversion and up-conversion fluorescence

A number of mechanisms, such as excited state absorption (ESA), energy transfer UC (ETU), cooperative UC and photon avalanche (PA) has been proposed to account for UC. This will be further reviewed in section 2.3.5.

2.3.4 The Luminescent Properties of Lanthanide Ions

Lanthanide exist in a trivalent state (except for cerium and europium) and their distinct optical properties arise from the electronic transitions within the 4f shell or from 4f-5d shell. The electron-phonon coupling is weak and radiative transition of lanthanide ions in solid hosts resembles those of the free ions. The positions of the lanthanide electronic levels are influenced more by spin-orbit interactions than by applied crystal field. The intra-4f transitions are generally parity forbidden and are partially allowed by crystal field interactions mixing opposite parity wavefunctions. For the reasons above, lanthanide ions produce long luminescence life times and narrow emission line-width. Figure 2.6 shows energy level diagrams for the individual lanthanide ions of each of the 13 lanthanides from cerium (ce) to ytterbium (yb) with partially filled 4f orbitals. A conventional way to denote energy levels of lanthanide ions is $^{2s+1}L_j$, which is labeled according to their angular momentum and spin quantum numbers. In symbol, the letter L refers to the total orbital angular momentum of the ion obtained by combining the orbital angular momentum of the individual electrons in the ion according to the Clebsch-Gordan series. The left superscript, presented as *2S+1*, is the number of possible orientations of the total spin of the ion, where *S* is the total spin of

the ion. The right subscript j represents the total angular momentum of the ion and is determined using the Russell-Saunders coupling scheme.

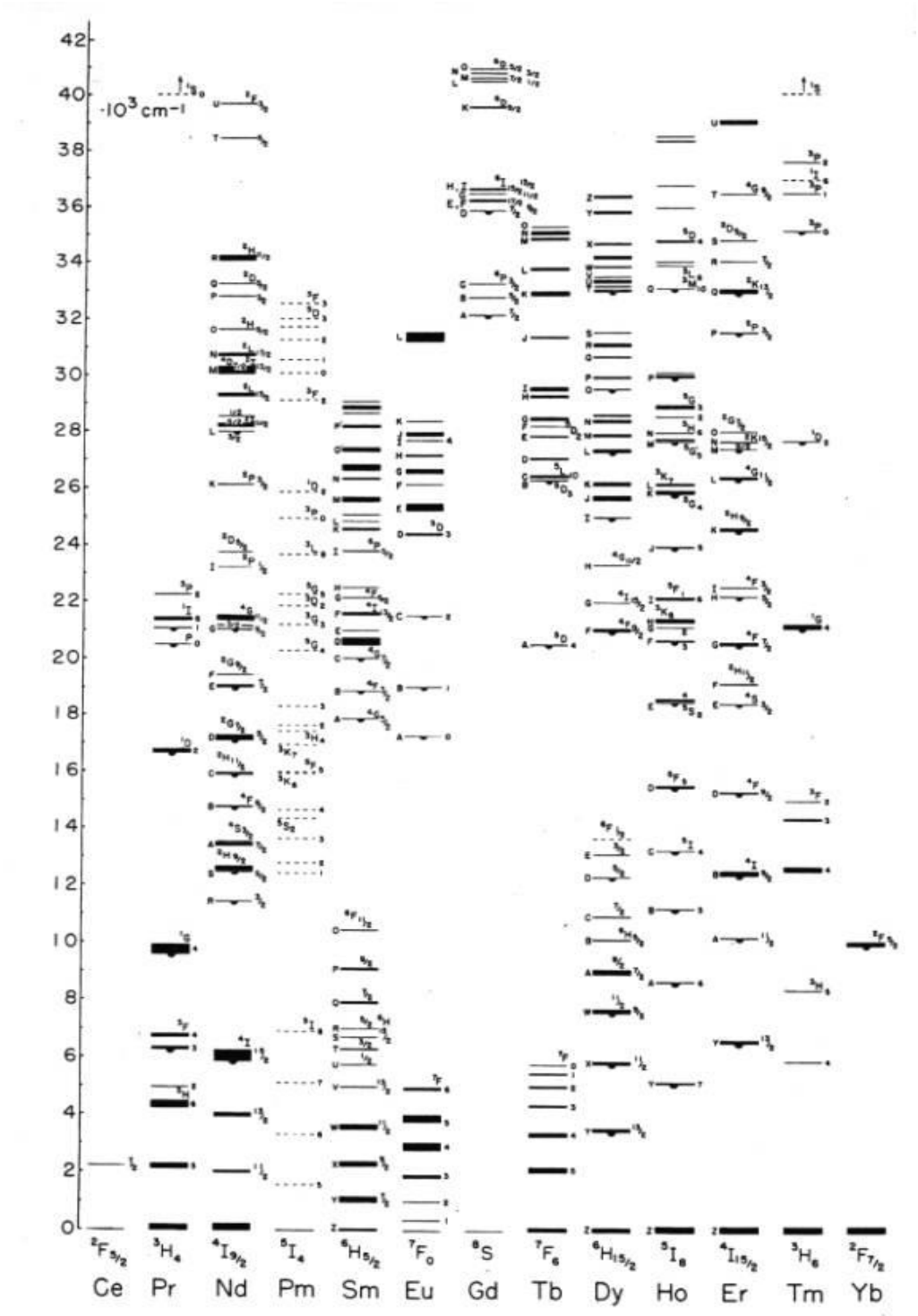

Figure 2.6 Dieke diagram for lanthanide ions.

2.3.5 Fluorescence Mechanism in Lanthanide Materials: Ion-ion Interactions.

In lanthanide doped nanomaterials, a number of ion-ion interaction could occur which leads to different electronic transition pathways.[23,77] Simple diagrams are presented in Figure 2.7 to illustrate the most important interactions.

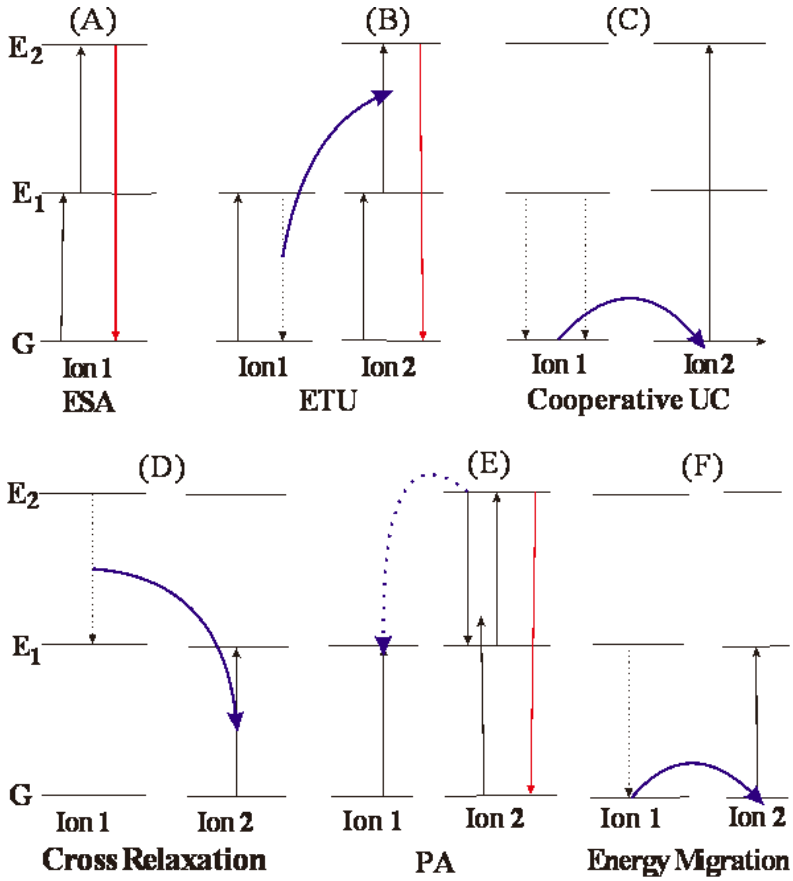

Figure 2.7 Ion-ion interactions of fluorescence mechanism in lanthanides. The black solid line, and dashed lines represents photon excitations, and relaxation respectively. The blue arrow shows energy transfer process between ions and the red arrow represents emissions.

2.3.5.1 Excited State Absorption (ESA)

In ESA, excitation takes the form of successive absorption of pump photon by a single ion. The energy diagram of the ESA is shown in Figure 2.7 (A). If excitation energy is resonant with the transition from ground level G to excited metastable level EI, photon absorption occurs and populates E1 from G in the process known as ground state absorption (GSA). A second pump photon promotes the ion from T_1 to higher-lying state E_2. The relaxation may result in emission.

2.3.5.2 Energy Transfer Up-Conversion (ETU)

ETU is similar to ESA because both processes utilize sequential absorption of two photons to populate the metastable level. The essential difference between ETU and ESA is that the excitation in ETU is realized through energy transfer between two neighboring ion. In an ETU process, each of two neighboring ions can absorb a pump photon of the same energy, thereby populating the metastable level E1, as shown in Figure 2.7 (B). A non-radiative energy transfer process promotes one of the ions to upper emitting state E2 while the other ion relaxes back to ground state G. The dopant concentration that determines the average distance between the neighboring dopant ions has a strong influence on the UC efficiency of an ETU process.

2.3.5.3 Cooperative Up-Conversion

Cooperative up-conversion is a special type of luminescence in which two interacting ions in the excited state return to the ground state simultaneously, exciting one ion to an energy state which is the sum of the energies of the two interacting ions.[78-80] The first observation of cooperative luminescence was reported by Nakazawa et al. for

Yb^{3+} pair in $YbPO_4$.[81] A simple schematic for the cooperative UC mechanism is present in Figure 2.7 (C).

2.3.5.4 Cross-Relaxation

In a cross-relaxation process, excitation energy from an ion decaying from a highly excited state promotes a nearby ion from the ground state to the metastable state. For example, the energy gap between two consecutive the energy levels E_2 or E_1 is close to energy gap between E_1 to G (Figure 2.7 (D)). At sufficiently high concentration of excited ions in level E_2, the population of the metastable state E_1 could increase by the decay of ions from the E_2 level which transfer its equivalent energy to promote nearby ions from the ground state G to metastable state E_1.

2.3.5.5 Photon Avalanche (PA)

The phenomenon of PA was first discovered by Chivian and co-workers in Pr^{3+}-based infrared quantum counters.[82] PA-induced UC features an unusual pump mechanism that requires a pump intensity above a certain threshold value. The PA process starts with population of level E_1 by non-resonant weak GSA, followed by resonant ESA to populate upper visible-emitting level E_2 (Figure 2.7 (E)). After the metastable level population is established, cross relaxation energy transfer (or ion pair relaxation) occurs between the excited ion and a neighboring ground state ion, resulting in both ions occupying the intermediate level E_1. The two ions readily populate level E_2 to further initiate cross-relaxation and exponentially increase level E_2 population by ESA, producing strong UC emission as an avalanche process.

2.3.5.6 Energy Migration

An ion 1 in the metastable state can interact with a nearby ground state ion 2, promoting it to a higher energy state (Figure 2.7 (F)). Although radiative emission may still occur from ion 2, the probability of non-radiative decay is increased with each successive transfer.

The efficiency of UC luminescence in these processes varies. ESA is the least efficient UC process. Efficient UC is possible in PA with metastable, intermediate levels that can act as a storage reservoir for pump energy. However, the PA process suffers from a number of drawbacks, including pump power dependence and slow response to excitation (up to several seconds) due to numerous looping cycles of ESA and cross-relaxation processes. In contrast, ETU is instant and pump power independent, and thus has been widely used to offer highly efficient UC over the past decade.

2.3.6 Synthesis of Lanthanide NPs

Lanthanide NPs can be synthesized by numerous methods, such as co-precipitation, thermal decomposition, microemulsion, etc. Co-precipitation has the advantage of controlling the particles size with nucleation and growth starting from atomic levels in homogenous solution. Roux's group extended the method to prepared Y_2O_3: Eu and Gd_2O_3: Eu NPs.[83] This method consists of two important steps: hydrolysis of $LnCl_3$ in diethylene glycol, which avoided particle agglomeration, and an elevated temperature that gets rid of water component during the reactions. Green fluorescent Gd_2O_3: Tb NPs were synthesized using a similar protocol.[83] This method improves the

dispersibility and size distribution of lanthanide oxide and oxysulfide NPs. Hydrothermal strategy can be used to obtain colloidal nanocrystals. YVO_4:Eu NPs were precipitated directly from the mixture of Ln-nitrate and sodium vanadate, and a further autoclave aging process resulted in highly crystallized zircon-type YVO_4: Eu NPs.[84] Besides direct precipitation methods, decomposition of the precursor can be employed to synthesize lanthanide doped fluoride NPs. Yan et.al synthesized LaF_3 by using lanthanide trifluoroacetates.[85] When the ion concentration in solution reached a critical point, burst nucleation occurred. Afterward the coordinating solvent (oleic acid) together with the non-coordinating (1-octadecene) leads to a slow but long growth stage of LaF_3 before Ostwald ripening. This approach was readily extended to other pure or doped fluoride NPs. Veggel et al. obtained water-soluble and bio-functionalized fluoride NPs from a one-pot reaction.[86] They grafted biotin onto hetero-bifunctional spacer molecules in advance to control NPs precipitation. Hasse and co-workers obtained cubic phase $NaYF_4$: Yb, Er NPs for the first time via the organic solvent route.[87] Two stock solutions which contained cationic and anionic-educt, respectively, were mixed and heated for the nanocrystals growth. Yi et al. reported co-precipitation of $LnCl_3$ and NaF in aqueous conditions with the aid of ethylenediamine tetraacetic acid (EDTA) and the crude deposits annealed at 400 ^oC to form $NaYF_4$: Yb, Er NPs.[88]

Cubic α-phase of $NaYF_4$ (metastable high-temperature phase) and hexagonal β-phase shape (thermodynamically stable low-temperature phase) nanocrystals have been synthesized so far. In the cubic structure, the cation sites are equal and Na^+ and RE^{3+}

cations are randomly distributed in the cationic sublattice, while in hexagonal structure, the cation sites are of three types: a one-fold site occupied by RE^{3+} (1a), a one-fold site occupied randomly by 1/2 Na^{+} and 1/2 RE^{3+} (1f), and a two-fold site occupied randomly by Na^{+} and vacancies (2h). Sites 1a and 1f have C_{3h} symmetry, whereas site 2h has Cs symmetry. The crystal structure of fluoride has an important effect on the optical properties. Much efforts have been dedicated to facilitate a α-to-β phase transition. A simple solvothermal route have been developed of which the NPs synthesized had a uniform size of 50 nm and were dispersible in ethanol.[89] Other methods were also demonstrated. Chen et al. adopted lanthanide-oleate and NaF to synthesize β-$NaYF_4$ NPs with liquid/solid heterogeneous reaction.[90] The nucleation and growth processes were localized at the two-phase interface, and an interface transfer mechanism was proposed to explain the narrow size distribution. Yan and co-workers demonstrated a general strategy for synthesizing monodisperse $NaLnF_4$ (Ln= Pr to Lu, Y) NPs via thermal decomposition of metal trifluoroacetate multi-precursors.[91] High-quality α- or β-phase $NaYF_4$: Yb, Er NPs were synthesized in one step by varying the ratio of CF_3COONa/ $Ln(CF_3COO)_3$ and the solvent composition. Comparison of the synthetic methods for lanthanide NPs is summarized in Table 2.3.

Table 2.3 Comparison of the synthetic methods for lanthanide NPs.

Synthetic methods	Co-precipitation	Thermal decomposition	Microemulsion	Hydrothermal synthesis
Synthesis	Simple, ambient condition	Complicated, Inert atmosphere	Complicated, Ambient condition	Simple, high pressure
Reaction Temperature(℃)	20-90	100-320	20-50	220
Reaction Time	minutes	Hours-days	Hours	Hours-days
Solvents	Water	Organic compounds	Organic compounds	Water or ethanol
Surface-capping Agents	Needed, added during or after the reaction	Needed, added during the reaction	Needed, added during the reaction	Needed, added during the reaction
Size Distribution	Relatively narrow	Very narrow	Relatively narrow	Very narrow
Shape control	Not good	Very good	Good	Very good
Yield	Highly scalable	Highly scalable	Low	Medium

2.4 Lanthanides in Multimodal Imaging

Integration of two or more imaging modalities results in multimodal imaging probes, are more comprehensive and better reliable biological data can be obtained for diagnosis. Lanthanide based multimodal imaging contrast agents have a good prospect of being used as labels in multimodal imaging. Recent examples include: 1) lanthanide in MRI/optical imaging probes; 2) lanthanide NPs for PET/MR and CT/MRI.

2.4.1 Lanthanide in MRI/optical Imaging Probes

Lanthanides, due to their unique properties, have been widely investigated in the last decade as MRI/optical imaging probes. Examples include Gd^{3+}-based multifunctional nanomaterials, SPIO and Dy-based multifunctional NPs.

2.4.1.1 Gd^{3+}-based Multifunctional Nanomaterials

Gadolinium is extensively used as T_1 contrast enhancement element in MRI. Many researchers have devoted their effort to develop new types of Gd-based multifunctional nanomaterials, combining QDs, mesoporous silica, silica NPs and other types of fluorescent NPs.

2.4.1.1.1 QDs as the Fluorophore

QDs have been shown to be excellent fluorophore, owing to their high fluorescence efficiency, high quantum yield and tunable multicolor.

Gd-DOTA (1,4,7,10-tetraazacyclododecane-1,4,7,10-tetraacetic acid) complex was functionalized on the surface of glutathione (GSH) -coated QDs.[92] The labeled QDs were reported to have high r_1 relaxivity of 365 $mM^{-1}s^{-1}$. However, it is based on per mole QDs, not Gd ions. Yang and co-workers grafted Gd (III) ions on the ZnS-passivated CdS: Mn QDs.[93] N-(Trimethoxysilylpropyl)ethyldiamine triacetic acid trisodium salt (TSPETE) was attached to the QDs. A yield of 107 Gd ions per QDs was reported. The MR relaxivities of the QDs were r_1 =20.5 $mM^{-1}s^{-1}$ at 4.7 T and r_2= 151 $mM^{-1}s^{-1}$. A water-soluble and paramagnetic Gd-based micelles were coated on the QDs by Mulder and co-workers.[94] The core/shell CdSe/ZnS QDs exhibited excellent optical properties. Coating the micelles with a paramagnetic shell rendered the NPs MR-detectable, water-soluble and biocompatible. MR results showed that the NPs had high r_1 relaxivity which was three times higher than that of Gd-DTPA. Paramagnetic QDs were later conjugated with cyclic arginine-glycine-aspartic acid (RGD) peptides

and were successfully targeted to human endothelial cells *in vitro*. This suggested that the NPs may be useful for the detection of tumor angiogenesis. In another study, Gerion and co-workers coated 10 nm QDs with a 1-2 nm thick PEGylated silica shell and amine reactive Gd-DOTA complexes that were cross-linked using sulfosuccinimidyl-4-(N-maleimidomethyl)cyclohexane-1-carboxylate(sulfo-SMCC).[95] MR relaxivities of the Gd-DOTA-modified QDs were r_1= 1019 $m^{-1}M^{-1}s^{-1}$ (0.5 T) and r_2= 2348 $m^{-1}M^{-1}s^{-1}$ (1.4 T). Prinzen et al. reported another QDs based magnetic-fluorescent NPs for visualization of cell death and activated platelets.[96] A biotinylated construct consisting of a lysine wedge with Gd-DTPA complexes was conjugated to biotinylated ANXA5 coupled to streptavidin coated QD-based NPs. In the newly designed structure with an increase in the load of Gd-DTPA and the particles exhibited large r_1 relaxivity of 3000−4500 $mM^{-1}s^{-1}$ per NP as well as excellent fluorescence.

2.4.1.1.2 Silica and Mesoporous Silica NPs

The accessibility of the magnetic center to water molecules is a key issue to design highly efficient T_1 contrast agents. Mesoporous materials provide an ideal platform for the development of MR–enhancing hybrid materials due to their high surface areas, tunable pore structure, rigid structure, larger pore volume, great surface-modification capability and good biocompatibility.

Tsai et al. fabricated paramagnetic Gd^{3+}-dye@mesoporous silica nanorods (MSN-R) for multifunctional cell-imaging.[97] The nanorods displayed relaxivities with r_1=22

$mM^{-1}s^{-1}$ and r_2= 41 $mM^{-1}s^{-1}$ at 0.47 T, which are about five and ten times higher than the values of the complex $[Gd(DTPA)]^{2-}$. The low r_2: r_1 ratio suggested that Gd-dye@ MSN-R served as a good dual-contrast agent for both T_1- and T_2-weighted MR imaging. Hsiao and co-workers reported Gd-fluorescein isothiocyanate mesoporous silica NP (Gd-Dye@MSN) as a delivery system of Gd for human stem cell tracking.[98] The NPs possess both green fluorescence and paramagnetism. MR imaging result showed that it was an ideal T_1 agent for stem-cell tracking with MRI using the clinical 1.5 T MRI instrument. Gd-Si-DTTA complex was grafted onto MSNs via siloxane linkage in another study.[99] The MR relaxivities of the particles were measured using both 3.0 T and 9.4 T MR scanner. On a per millimolar Gd basis, the particles had r_1 relaxivities of 28.8 $mM^{-1}s^{-1}$ at 3T and 10.2 $mM^{-1}s^{-1}$ at 9.4 T while r_2 relaxivities of 65.5 $mM^{-1}s^{-1}$ at 3T and 110.8 $mM^{-1}s^{-1}$ at 9.4 T, respectively. The larger relaxivities were attributed to the ready access of water molecules through the nanochannels of the MSN-Gd particles. MSN-Gd showed a highly efficient T_1 contrast effect for intravascular MR imaging and an excellent T_2 contrast effect of soft tissue when applied at a higher dosage.

Rieter et al. reported high payloads of paramagnetic hybrid dye-doped silica NPs with a magnetic layer as multimodal imaging agents.[100] Hybrid silica NPs which contained a luminescent $[Ru(bpy)_3]Cl_2$ core (bpy=2,2'-bypyridine) and a paramagnetic silylated Gd complex monolayer was prepared using a reverse microemulsion method. MR relaxivities results showed that the NPs had a r_1 of 19.7 $mM^{-1}s^{-1}$ and a r_2 of 60.0 $mM^{-1}s^{-1}$ on Gd^{3+}-ion basis, which indicated high payloads of Gd(III) magnetic centers.

Incorporating high payload magnetic center for detection to increase the sensitivity of MRI is more desirable in multimodal imaging. Therefore, the same group increased the relaxivities of Gd^{3+}-chelated silica NPs using the layer-by-layer polyelectrolyte deposition method.[101] The r_1 and r_2 values per particle were increased proportionally with the increased number of layers.

2.4.1.1.3 Single Phase Gd-based Fluorescent Nanomaterial

High payload of Gd ions on the surface of single NP is more desirable for their application in targeting and imaging. Surface grafting processes usually result in a low payload of Gd^{3+} complex on a single NP surface. Therefore, codoping Gd^{3+} ions inside fluorescent NPs is a more straightforward and effective route to obtain effective multifunctional NPs for dual modal imaging.

Li et al. synthesized dual modal optical and MR imaging agent CdSe: Gd NPs and showed that the T_1 relaxation of the CdSe: Gd NPs had much larger r_1 value than that of conventional Gd-DTPA.[102]

Lanthanide oxides have also been shown to be promising multimodal contrast agents. Examples include Gd_2O_3 encapsulated within a shell of organic fluorophores,[103] Gd_2O_3/ carbon hollow shells,[104] Gd_2O_3 NPs embedded within single-walled carbon nanohorn (SWNHs),[105] Gd_2O_3 ultrasmall nanorods doped with lanthanide ions[106,107] and Y_2O_3 doped with Gd^{3+} ions.[108] Jean-Luc Bridot's group presented a pioneering work on Gd_2O_3 NPs and introduced them as multimodal contrast agents.[103] The

possibility to incorporate a large number of Gd ions makes the NPs an attractive candidate as positive contrast agents in MRI. In their work, ultrasmall Gd_2O_3 core was embedded in a polysiloxane shell where the outer part was functionalized by PEG and inner part by organic dyes. The relaxivities decreased with increasing core size. Thus, the 2.2 nm Gd_2O_3 core showed greatest contrast in MRI. Gd_2O_3/C hollow nanoshells have also been synthesized using biological gelatin as core templates through a two-step thermal treatment.[104] Interestingly, the Gd_2O_3/C nanoshells showed brightened images of kidney cortex and liver in mice whereas the Gd_2O_3/C@PSMA nanoshells showed darken liver signal. Both Gd_2O_3/C and Gd_2O_3/C@PSMA nanoshells had no significant toxicity and were eliminated after 24 h. The nanoshells can effectively target malignant A549 lung cancer cells and kill them by photothermolysis due to their large extinction coefficient at 808 nm with good absorbance. Gd_2O_3 NPs were also embedded within single-walled carbon nanohorn (SWNHs).[105] Das and co-workers reported a simple strategy for synthesizing paramagnetic-fluorescent ultranarrow Gd_2O_3 nanorods as multimodal contrast agents.[109] DC and UC fluorescence can be achieved by changing the lanthanide dopants. The Yb/Er codoped Gd_2O_3 NPs exhibited good T_1-weighted MRI contrast, comparable to the commercial product Gadovist™.

Fluoride host materials provide some distinct advantages over the oxide materials as the fluoride matrix has low absorbance and the emitter can be excited directly. Quenching of the excited state of the lanthanide ions will be minimized when they are doped into fluoride hosts, which leads to long emission lifetimes and high

luminescence quantum yields even in the case of IR emitting ion.[110] Kumar and co-workers reported lanthanide ions doped $NaYF_4$ NPs for optical and MR bioimaging.[111] Lanthanide ions Gd^{3+} and Er^{3+}/Yb^{3+}/ Eu^{3+} were co-doped into fluoride NPs. Gd^{3+} codoped NPs imparted strong T_1 contrast effect and strong UC fluorescence. Thus, these fluoride NPs doped with lanthanide ions can be used as dual-modal contrast agents in optical and MR imaging. Yet in another study, by replacing yttrium (Y) with paramagnetic gadolinium (Gd), Heyon reported core/ shell $NaGdF_4$: Yb, Er/ $NaGdF_4$ NPs as bimodal contrast agents.[112] The NPs were found to be extremely resistant to photobleaching and no photoblinking occurred. The bimodal NPs in T_1-weighted MRI showed a good contrast in T_1-weighted MRI was got in 1% agarose solution and in cells (SK-BR-3). Li et al reported hybrid NPs consisting of an up-converting lanthanide doped $NaYF_4$ nanocrystal core and a Gd-based paramagnetic complex shell.[113] The uniform core-shell structured $NaYF_4$: Yb, Er@Si-DTTA (3-aminopropyl(trimethoxysilyl) diethylenetriamine tetraacetic acid) NPs were firstly prepared and Gd ions were then loaded onto the NPs. The NPs had strong and stable fluorescence although the intensity decreased slightly due to the out Si-DTTA shell. The NPs had the relaxivities r_1 of 20.1 $mM^{-1}s^{-1}$ and r_2 of 55.0 $mM^{-1}s^{-1}$ on a per milimolar Gd^{3+}-ion basis. In addition, MR signal intensity increased with increasing concentration of NPs in the T_1-weighted mode while signal became weaker with increasing concentration of NPs in the T_2-weighted mode, which suggested that the NPs may be useful as contrast agents for both T_1- and T_2- weighted MR imaging.

2.4.1.2 SPIO-based or Dy-based Multimodal Imaging Agents.

SPIO NPs are representatives of T_2 contrast agents in MRI. Doped with different lanthanide elements or coated a shell with lanthanide elements, the new "two-in-one" bifunctional NPs are able to act as T_2 contrast agents as well as fluorescence labeling agents. Yu and co-workers reported water-soluble Fe_3O_4@LaF_3: Ce, Tb nanocrystals with the average diameter around 30 nm.[114] These NPs showed strong DC luminescence and good magnetism. Zhang et al. reported Tb-doped γ-Fe_2O_3 NPs that combined superparamagnetism and luminescence into the same nanocrystals.[115] Vaccaro et al. synthesized dextran-coated europium and terbium doped ultrasmall iron oxides.[116] The presence of lanthanide in the iron oxide matrix conferred attractive optical properties for long-term multi-labeling studies. Besides, they offered high photostability, a narrow emission band and a broad absorption band combining high sensitivity of time-resolved fluorescence with high spatial resolution of MRI. However, most of these types of bifunctional NPs synthesized to date are composed of DC phosphors and iron oxide NPs. Besides iron oxide NPs could quench the fluorescence from phosphors. In addition, DC fluorescence has some intrinsic limitations, such as autofluorescence, low penetration depth and photondamage to the biological specimen, limiting their applications in biolabeling. Cheng et al. reported $NaYF_4$: Yb, Er coated iron oxide NPs that possessed magnetic, UC fluorescence and bioaffinity.[117] However, no MR imaging was preformed.

Dysprosium (Dy) element has been extensively used in MRI to enhance T_2 contrast, especially in high magnetic field MRI. Das et al. reported a single-phase bimodal Dy_2O_3: Tb NPs as dual mode contrast agents in MRI and fluorescence imaging. [118]

Instead of dark contrast enhancement, the NPs showed interesting bright negative images due to the low r_2 relaxivity. This may be useful to circumvent some problems associated with the normal negative T_2 contrast agent images. In another study, Dy-DOTA chelate coupled to the surface of a noncytotoxic indium phosphide/zinc sulfide (lnP/ZnS) QDs was synthesized for fluorescence detection and MR imaging.[119] The bimodal nanomaterial functioned as a self-transfecting contrast agent for nonspecific intracellular labeling.

2.4.2 Other Multimodality Contrast Agents

Fabrication of other multimodality contrast agents is still in their infancy although they hold great promise in preclinical and clinical studies. Only a few works have been reported on lanthanide ions based multimodal imaging nanomaterials.

Gustafsson and co-workers reported gadolinium based MRI contrast agents and iron oxide based probes that labeled with ^{64}Cu for PET imaging which had potential for dual mode PET/MRI imaging of vascular inflammation.[120] Another example is multimodal imaging contrast agents for CT and MRI.[121] Gold NPs were functionalized within a multilayered organic shell which gadolinium chelates were bound through disulfide bonds. The contrast enhancements in MRI arise from Gd ions and gold core provided a strong X-ray absorption. The study revealed that the particles were suited for dual modality imaging and could freely circulate in the blood vessels without undesirable accumulation in the lungs, spleen and liver.

2.4.3 Therapeutic Applications of Lanthanide Multifunctional Nanomaterials

Lanthanide nanomaterials have found potential applications in various biomedical areas, such as imaging, cell targeting, labeling, drug delivery, diagnostics and therapy.[15,16,122-129] Fluorescent NPs are often embedded into the nanocarriers to make them observable in order to get better understanding, diagnosis and treatment of the diseases. Lanthanide-based NPs have also been investigated in cancer cell ablation. Examples include photodynamic therapy (PDT), which exploits NIR UC emission and a suitable photosensitiser to cause cell apoptosis, and neuron-capture therapy (NCT), a form of cancer therapy involving radiation.[130] In addition, lanthanide-based NPs have also been investigated in gene therapy and other therapeutic applications.

2.4.3.1 Lanthanide NPs as Drug Delivery System

2.4.3.1.1 Lanthanide NPs as Drug Delivery System

Lanthanide NPs have been investigated as drug delivery system. A novel class of layered hydroxide nanosheets with the general composition $Ln_2(OH)_5NO_3 \cdot H_2O$ (Ln= Gd and Dy), for example, have been investigated as drug delivery systems.[131] The nanosheets underwent facile anion exchange reactions with a wide variety of amino acid and antibodies at room temperature, which suggested that they could potentially be used as inorganic drug carriers for many different pharmaceutical active compounds such as amino acids and antibiotics. CaF_2: Ce^{3+}/Tb^{3+} hollow spheres were developed for storage and delivery of ibuprofen (IBU), a well-known non- steroidal anti-inflammatory drug.[132] Photoluminescence (PL) emission spectra of the resultant nanocystals revealed that the PL intensity increased with increasing drug release time

and reached a maximum when IBU was completely released, which was attributed to the quenching effect of the organic groups in IBU to the emission of Tb^{3+} in the system. This characteristic can be used to monitor the drug release process.

The emission of upconverting $NaYF_4$: Yb/Tm NPs was used to trigger the release of molecules from "caged" forms.[133] The light-triggered release of molecules from "caged" compound offered significant benefits. These compounds could be spatially and temporally controlled to provide "on-demand" and in situ drug delivery using light as a means of trigger release. $NaYF_4$: Yb/Tm NPs provided the most intense emission band at 333-355 nm to excite the cage molecules and consequently, the caged-decorated NPs were able to release the molecules from the cage. This approach overcame the problem associated with UV or visible light excitation that was needed to trigger the release from small molecules systems and therefore, strong background autofluorescence, low detection sensitivity, low light-penetration depth in tissue and photodamage to the living organisms were circumvented.

2.4.3.1.2 Silica-based Systems

Silica NPs, especially mesoporous silica NPs (MSNs), have been investigated as drug carriers for years as they provide an excellent reservoir for drug storage owing to their large surface area, stable chemical structure and tunable porous size and volumes.[134-136] Multifunctional MSNs that encapsulate not only drug molecules but also fluorescent, magnetic particles into the silica matrix offer better platform as drug carriers.[137] The materials not only have large surface area for the storage and delivery

of drugs but also possess magnetic and fluorescence entities that can be used to track and evaluate the efficiency of the drug release.[137] The composites may target delivery path and provide insights of how the drugs can be delivered and drug release can be achieved. The design of MSNs loaded with drug, fluorescent and magnetic agents has attracted a lot of research interest and significant advancements have been made.

Yang's group conducted a series of experiments by conjugating $CaWO_4:Ln^{3+}$ (Ln = Eu^{3+}, Dy^{3+}, Sm^{3+}, Er^{3+}, Tb^{3+}) and $YVO_4:Eu^{3+}$ NPs into different silica NPs (MCM41 and SBA15) and their drug delivery properties were investigated.[138-142] Drug absorption behavior of the NPs was affected by the morphology, particle size, mesoporous structure of the adsorbent and the PH value of the buffer solution. The emission intensity of the NPs increased with an increase in the cumulative released amount of drug and reached a maximum when the drug was completely released, making the extent of drug release easily identified, tracked and monitored by the change of luminescence. Yang and Kong coated MSNs onto UC Yb/Er codoped lanthanide fluoride NPs,[143,144] and used them for drug delivery applications.

Functionalized MSNs with magnetic and fluorescent properties have also received considerable attention. Superparamagnetic NPs can be incorporated into these materials by depositing mesoporous silica around the NPs. Yang et al. developed sandwich-like structured materials with a magnetite core that served as seeds to grow nonporous silica layers and mesoporous silica was then further coated outside.[145] YVO_4: Eu NPs were deposited onto the surface of the mesoporous silica shell. Gai and

coworkers attached $NaYF_4$: Yb, Er NPs onto the surface of mesoporous silica shell.[146] In both case, the multifunctional NPs were used for the controlled release of IBU by an external magnetic field. The NPs acted as a multifunctional drug carrier system, which could realize targeting and monitoring of drugs simultaneously.

2.4.3.1.3 Other Hybrid Lanthanide-based Systems

Other nanosize drug delivery systems, such as carbon nanotubes (CNTs), bioactive mesoporous materials and polymer-based NPs have been explored as drug carriers in biomedical research.

CNTs have been used as a platform for carrying drugs for years due to their unique properties, including appropriate dimensionality and chemical stability.[147-149] Multiwalled carbon nanotubes (MWCNTs) with a hollow structure have inner diameters on the order of 50-150 nm which were explored as drug delivery.[150] However, CNTs exhibited weak infrared (IR) emission and Y_2O_3:Eu NPs were therefore deposited onto the surface of MWCNTs. This method opened up the possibility of designing functionalized CNTs for simultaneously drug delivery and bioimaging. Other bioactive mesoporous materials, such as bioactive glasses (MBG), hydroxyapatite [HAp, $Ca_{10}(PO_4)_6(OH)_2$)] and strontium hydroxyapatite have also been investigated as drug carriers for the delivery of various molecules.[151-153] They have high pore volume for storage and delivery of drugs.[154] Polymer-based nanomaterials, another type of drug carriers, have also under extensive investigation for medical imaging and diagnosis.[155,156] Typical polymer nanomaterials were core-shell structures,

where the hydrophobic core entrapped the hydrophobic drugs and hydrophilic chain in the shell formed hydrogen bonds with the surrounding to form a tight shell around the core. Therefore, the hydrophobic cores are effectively protected against hydrolysis and enzymatic degradation.[157] Moreover, polymers can be functionalized with different agents, achieving multifunctional purpose for tumor therapy. Rieter and coworkers investigated polymer systems for the delivery of platinum (Pt) based drug to cancer cells.[158] Pt-based drugs are still used as the frontline treatment for cancer. The polymers were constructed from Tb^{3+} ions and Pt-containing bridging ligands. Amorphous silica shell was further stabilized the polymers to prevent rapid dissolution and to effectively control the release of Pt species. Tb^{3+} ions were used as luminescent centers. The release of Pt drug could be controlled by encapsulating the polymers in shells of amorphous silica. This approach allowed for the design of polymer-based NPs as effective delivery vehicles for a variety of biologically and medically important cargoes such as therapeutic and imaging agents.

2.4.3.2 Lanthanide NPs in Cancer Therapy

Lanthanide NPs have also found applications in chemotherapy, NCT and PDT. Wang et.al loaded PEGylated $NaYF_4$: Yb/Er NPs with a commonly used chemotherapy molecules, doxorubicin (DOX) via physical adsorption upon simple mixing.[159] Figure 2.8 (1) shows the schematic illustration of the drug delivery system. The loading and releasing of DOX from the NPs were determined by varying pH values. The DOX loading increased with pH values while decreased pH values increased the DOX releasing. Intracellular drug delivery and UC imaging were studied by using HeLa

cells. HeLa cells were incubated with the NPs for different time, shown in Figure 2.8 (2). Bright UC signals first emerged inside cells after 2 h incubation, and increased as the time progressed. Free DOX was able to enter cells rapidly with strong DOX fluorescence signal observed (Figure 2.8 (3)). The toxicity of the UCNP-DOX was reduced due to the less efficient cellular uptake of NPs compared with the free DOX. Therefore, targeted cell imaging and drug delivery can be achieved with folic acid conjugated UCNPs. Photosensitizers, such as Ce6, TCPP, can also be loaded into this system for potential NIR light mediated PDT. Therefore, this strategy provided a facile and flexible way to load and deliver different therapeutic molecules.

Besides chemotherapy, NCT has gained interests in recent year and it uses radiation emitted from gadolinium-157 (^{157}Gd) for its neutron-capture reaction with thermal neutrons.[130] Integration of MRI and NCT seems possible as ^{157}Gd has the highest thermal neutron-capture cross section and has been widely used as MRI contrast agents.

PDT is a light-activated treatment for cancer and other diseases. It utilizes a light sensitive drug (i.e. photosensitizer) that preferentially localizes in malignant tissues to treat the tissues upon the irradiation of light with a specific wavelength.[160-162] The generally-accepted mechanism of PDT is based on the interaction between the excited photosensitizer and surrounding molecules, generating reactive oxygen species (ROS), such as singlet oxygen. ROS can cause oxidative damage to biological substrates and ultimately cell death. The main drawback of this therapy is that currently approved

PDT photosensitizers absorb in the visible spectral region below 700 nm, where light only penetrates a few millimeters into skin. This problem may be overcome using UCNPs conjugated with the photosensitizer.

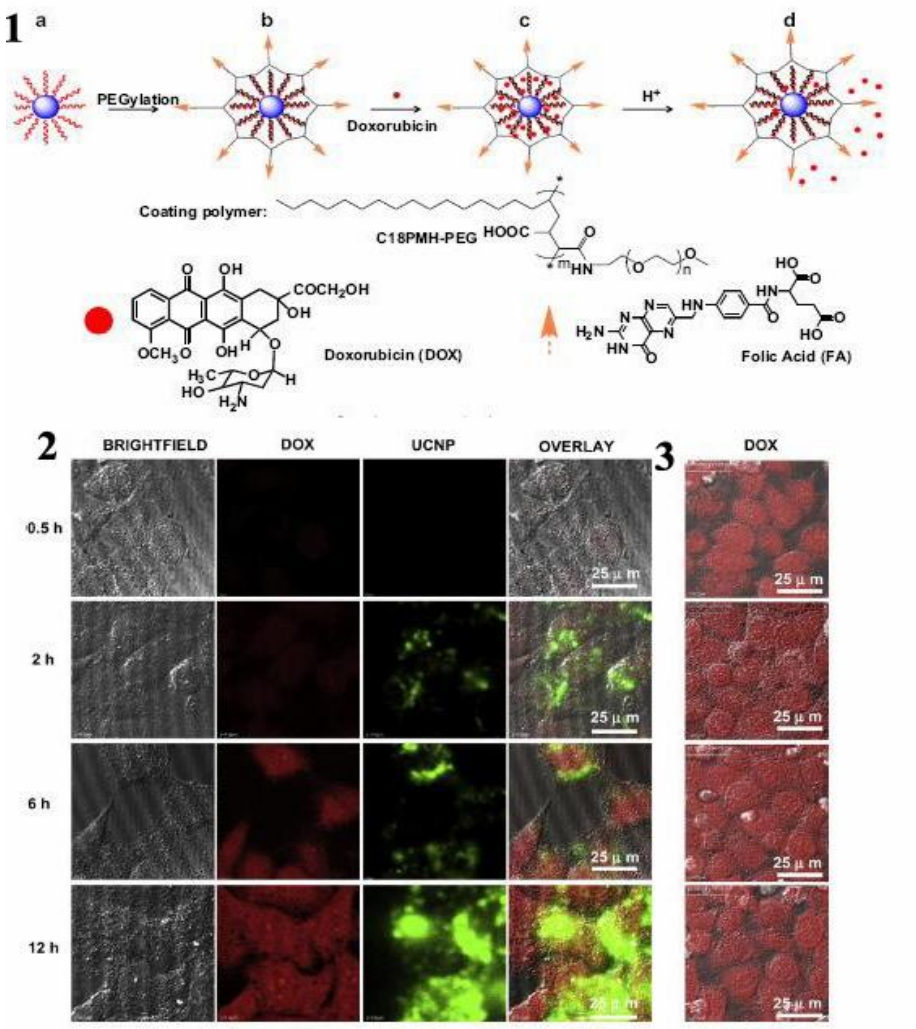

Figure 2.8 (1) Schematic illustration of the $NaYF_4$: Yb/Er (UCNP) NPs-based drug delivery system. (a) oleic acid capped $NaYF_4$: Yb/Er NPs; (b) Poly(maleic anhydride-alt-1-octadecene)-PEG-FA functionalized UCNPs; (c) DOX loading on $NaYF_4$: Yb/Er NPs; (d) Release of DOX from $NaYF_4$: Yb/Er NPs triggered by decreasing pH. Laser scanning confocal microscopy (LSCM) images of HeLa cells

incubated with (2) UCNP-DOX and (3) free DOX for 30 min, 2 h, 6 h and 12 h at 37 ^{0}C. Emissions from UCNPs (green colored) and DOX fluorescence (red colored) were recorded in the wavelength ranges of 500-700 nm and 500-600 nm, under 980 nm and 488 nm laser excitations, respectively.[159] (reprinted with permission from ref. 158. Copyright 2011, Elsevier)

Zhang et al. encapsulated photosensitizing molecules merocyanine 540 (M-540) into a $NaYF_4$: Yb/Er NPs deposited onto silica NPs.[162] Merocyanine 540 (M-540) can produce $^1O_2$ and other reactive oxygen species. The green emission from the core excited the M-540 and generated $^1O_2$ which was detected by using the disodium salt of 9,10-anthracenedipropionic acid (ADPA) as a probe molecule. The decrease of ADPA fluorescence intensity over time confirmed the $^1O_2$ generation from the M-540-coated NPs under IR excitation. They further extended this study to other $NaYF_4$:Yb/Tm NPs.[163] Zinc-phthalocyanine (ZnPc) photosensitizers were attached to polyethyleneimine-modified $NaYF_4$: Yb/Er and they were used as nanotransducers for PDT of cancer cells.[164] However, the above studies suffer from some limitations. It is not only difficult to control the amount of photosensitizers incorporated into the silica shell but the efficiency of PDT for these particles is low as the nonporous silica shell blocks the cell generated reactive $^1O_2$ species out. Therefore, Zhang's group employed mesoporous silica coated $NaYF_4$: Yb/Er NPs and ZnPc were incorporated into the porous silica shell. The NPs can efficiently convert NIR light to red light that was responsible for activating the photosensitizer to produce $^1O_2$ to induce cell death.[165] They further studied the photodynamic effect of the NPs loaded with ZnPc on murine

bladder cancer cells (MB49).[166] High reactivity of $^1O_2$ toward biomolecules played a major role in determining the efficiency of PDT against cancer. The ZnPc-loaded $NaYF_4$ NPs, once uptake by the cells, could produce more $^1O_2$ than those without ZnPc, indicating that a greater extent of apoptosis would be expected in the PDT-treated cells. Cell nuclear morphology change provided an accurate indicator in the involvement of cell death. Morphological changes in cell nuclei reflected chromatin condensation in compact masses with change in the nuclear shape occurring at an early point in the series of apoptotic morphological events as observed in PDT-treat cells of the present study. Besides, loss of DNA integrity was another indicator of apoptosis. The gel-electrophoresis using DNA extracted from apoptotic cells displayed a characteristic internucleosomal ladder of DNA fragments after treatment of MB49 cells by PDT. Mitochondrion was another indicator of apoptosis. Upon receiving an apoptotic stimulus, cytochrome c, which was localized between the inner and outer mitochondrial membranes, triggered its release from the mitochondria into the cytosol, forming caspases which would in turn activate caspase-3 and other caspases to induce apoptosis terminally. These results suggested that UCNPs could efficiently work as a carrier for photosensitizer and they can be used in PDT to treat cancer and also some other diseases.

2.4.3.4 Lanthanide NPs for Gene Therapy

RNA interference (RNAi) is being widely explored as a means of tumor therapy due to specific and potent silencing of targeted genes. The major obstacle to therapeutic application of RNAi is delivering siRNA to the target tissue due to fast degradation of

siRNA in the physiological environment, its poor cellular uptake, inefficient endosomal escape, insufficient dissociation from the carriers and the lack of targeting ability.[167,168]

Silica-coated $NaYF_4$:Yb/Er NPs were developed and used for fluorescence imaging and the delivery and tracking of siRNA by Jiang and co-workers.[168] The silencing effect of siRNA on luciferase gene was studied after they were delivered into the cells. The results showed that the NPs could be used as both fluorescent imaging probes and efficient delivery agents of siRNA. In another study, the same group utilized $NaYF_4$: Yb/Er NPs as energy donor and BOBO-3 as energy acceptor to study intracellular release and biostability of siRNA in live cells by using fluorescence resonance energy transfer (FRET) method.[169] The $NaYF_4$: Yb/Er/siRNA-BOBO-3 complex was developed where BOBO-3-stained siRNA was attached onto the surface of amino-group-modified silica/$NaYF_4$: Yb/Er NPs. Energy was transferred from the UCNPs to BOBO-3 under NIR excitation. The efficiency of FRET in the UCNP/siRNA-BOBO-3 depended on the siRNA/UCN ratio and dye/bp ratio. This technique provided a promising outlook for *in vitro* and even *in vivo* detection of biological molecules.

Other gene delivery systems carrying lanthanide ions have also been reported. Kenny et al. described a liposome-entrapped siRNA (LEsiRNA) NPs for delivering anticancer survivn siRNA to tumor cells.[170] Gd-DOTA was embedded into the PEG-coated LEsiRNA NPs to make them MR sensitive. The MR relaxivity value of

the NPs was superior to the clinical agents Dotarem. The NPs accumulated in the tumors by MR contrast image enhancements 24 h post-administration, which was further confirmed with ex-vivo fluorescence microscopy. It showed colocalization of NPs and siRNA within the tumor reduced survivin expression. Therefore, the nanovehicles not only allowed for the functional delivery of siRNA but incorporated MRI and fluorescence labels for the simultaneous monitoring of drug delivery. Their ability to significantly reduce the tumor growth showed their potential use in cancer therapy. In another study, Li and his workers synthesized a nanoplex carrying Gd based MRI reporter for *in vivo* detection and optical reporters for microscopy to image the delivery of siRNA and a functional prodrug enzyme in breast tumors to achieve image-guided molecular targeted cancer therapy.[171] The results suggested that the combination of siRNA and prodrug enzyme had great potential in improving the therapeutic efficiency of cancer treatment with minimum normal tissue damage.

2.4.3.5 Other Therapeutic Applications of Lanthanide NPs

Gadolinium ions exhibit similar properties to that of calcium in biological systems, presumably due to the comparable ionic radius as calcium. They can displace calcium from its binding site on the external surface of the plasma membrane and have been found to inhibit phagocytosis in liver macrophages,[172-174] and to induce apoptosis of macrophages *in vitro*.[175] Roland and co-workers used hepatic kupffer cells isolated from rats to study the secretary response to lipopolysaccharide (LPS) with gadolinium which was found to inhibit calcium flux and calcium dependent PGE2 synthesis.[173] In another study, Epstein and co-workers prepared nanosuspensions of alendronate with

Gd which inhibited macrophage cell line growth in a dose-response manner in comparison to the various agents in solution and in liposomes and were found to attenuate neointimal hyperplasia and stenosis in rats.[176] This result correlated with the significant reduction of circulating monocytes. The nanosuspensions possessed the advantages of having no additives for minimal provocation of side effects, and the potential of immunomodulating inflammatory disorders.

Lanthanide NPs have also been reported to inhibit the progression of reactive oxygen intermediates induced cell death, protect cells against bacterial, viral and oxidative stress.[177,178] Man and co-workers elicited that lanthanide oxide NPs had an autophagic response in a dose- and time-dependent relation in HeLa cell line and the autophagy induction was a common biological effect for the lanthanides.[178] The autophagy induced by NPs was complete and accompanied by vacuolization within the cytoplasm. Therefore, lanthanide oxide can be used as a new class of autophagy inducers.

2.4.4 Design of Nanoparticles for Molecular Imaging

Biodistribution of NPs has to be considered and optimized, because it is impossible for all the injected NPs to be accumulated at the diseased tissues. Typically, inorganic NPs administrated intravenously are mostly taken up by the liver and spleen; the amount of accumulated particles and their indispensable elimination are strongly dependent on their size, shape, chemical composition and surface chemistry.

2.4.4.1 Size and Shape Control of Nanoparticles

NPs can be easily taken up into cells via endocytotic vesicles and exert influence over the biodistribution and pharmacokinetics of drug molecules within the body. NPs have much larger surface area than their counterparts, which enables them efficiently bind, absorb, and carry biomolecules. Experimental findings from animal models suggest that sub-150 nm, neutral or slightly negatively charged entities can move through tumor tissue. For effective cancer therapy, it is generally thought that the size of therapeutic nanomaterials should be in the range of 10-100 nm, as larger particles have limited diffusion in the extracellular space. Besides, the removal of the NPs after a therapeutic process is important as the accumulation of the residual particles may impose hazardous risks to the patient and they are largely dependent on the size of NPs. Furthermore, the shape of the NPs is another issue that can influence their therapeutic efficiency. On the basis of dimensionality, basic motifs of the inorganic NPs fabricated falls into 0-dimensional cubes, spheres, polyhedrons; 1-D wires and rods; 2-D prisms, plates, discs; and some complex structures such stellations and tetrapods.[179-181] The formation mechanism behind different shape formation is complicated and current perceptive is incapable to present details for the evolution pathways. However, typical NPs formation mechanism can be broken down into three distinct phases: (1) nucleation, (II) evolution of nuclei into seeds which are something larger than nuclei, and (III) growth of seeds into NPs.[179-181] The final shape of the NPs depends primarily on the inherent crystal structure of the corresponding seed crystals. Inherent anisotropy of the crystal structure, crystal surface reactivity, dipolar interactions, and binding affinity of the capping ligands plays significant role in

forming different shapes. Non-spherical particles with rough edges and irregular surfaces typically have more surface area than spherical particles with smooth surfaces. The surface area can also affect the binding capacity of the particles to cancerous cells and tissues.

2.4.4.2 Mechanical Properties

A NP required a certain mechanical integrity for survival within the turbulent dynamics of the bloodstream. NPs held together only by charge-based forces will certainly be disrupted rapidly. Crosslinking by covalent bonds lead the necessary stiffness and cohesion to survive bloodstream turbulence, and also guarantees the stability of NPs at the target site, where stationary accumulation of stable NPs is essential for molecular imaging. However, a NP can be so stable that its clearance from the organism is possible only by macrophages, which prolongs the duration of exposure to any toxins (such as gadolinium) that are present in the NP. An ideal signaling NP would remain intact the target site until its molecular imaging role is fulfilled, then disintegrate rapidly and vanish from the organism within hours, for example, by renal excretion. The crystalline of NPs affects NPs optical properties. For example, hexagonal phase $NaYF_4$ offers about one-order-of-magnitude enhancement of upconversion efficiency relative to their cubic phase counterpart. Their applications in light-involved therapy, such as photodynamic therapy are exclusively based on hexagonal phase $NaYF_4$.

2.4.4.3 Surface Functionalization.

NCs intended for bioapplications often require surface functionalization with different ligands to render them biocompatible. NCs prepared by high-temperature routes usually lack functional moieties for dispersion in aqueous media. Hydrophilic ligands are commonly used to functionalize the NCs surface prior to disperse in aqueous media or attachment with biomolecules. Different strategies have been explored. Table 2.4 summarized typical strategies and surface molecules used for making hydrophilic NPs

Ligand exchange has been demonstrated by Yi et al. for up-converting $NaYF_4$ NCs where they used polyethylene glycol 600 diacid (HOOC-PEG-COOH) to replace the surface amine ligand (oleylamine) with carboxyl-functional groups.[182] The carboxyl-functional groups on the NP surface render them to water-dispersible. Chen et. al developed ligand oxidation technique alternative to ligand exchange.[183] The same group later reported a strategy based on epoxidation of the double bond followed by the reaction with PEG-amines to render the NCs water dispersible.[184] A limitation of this process is that it can only be applied to ligands containing unsaturated carbon-carbon bonds and not applicable to all ligands in general. A ligand attraction proves was reported by Yi et al. where they coat the core-shell NCs with 25% octylamine and 40% isopropylamine modified poly(acrylicacid) (PAA).[185] Wang et al reported layer-by-layer assembly technique which is based on the adsorption of alternatively charged polyions on the NCs surface.[186] They reported sequential adsorption of poly(allylamine hydrochloride) and negatively charged poly(sodium 4-styrenesulfonate) onto the $NaYF_4$ surface to generate water-dispersible NCs.

Table 2.4 Typical strategies and surface molecules used for making hydrophilic NPs. (Reprinted with permission from ref. [23]. Copyright 2009, the Royal Society of Chemistry (RSC))

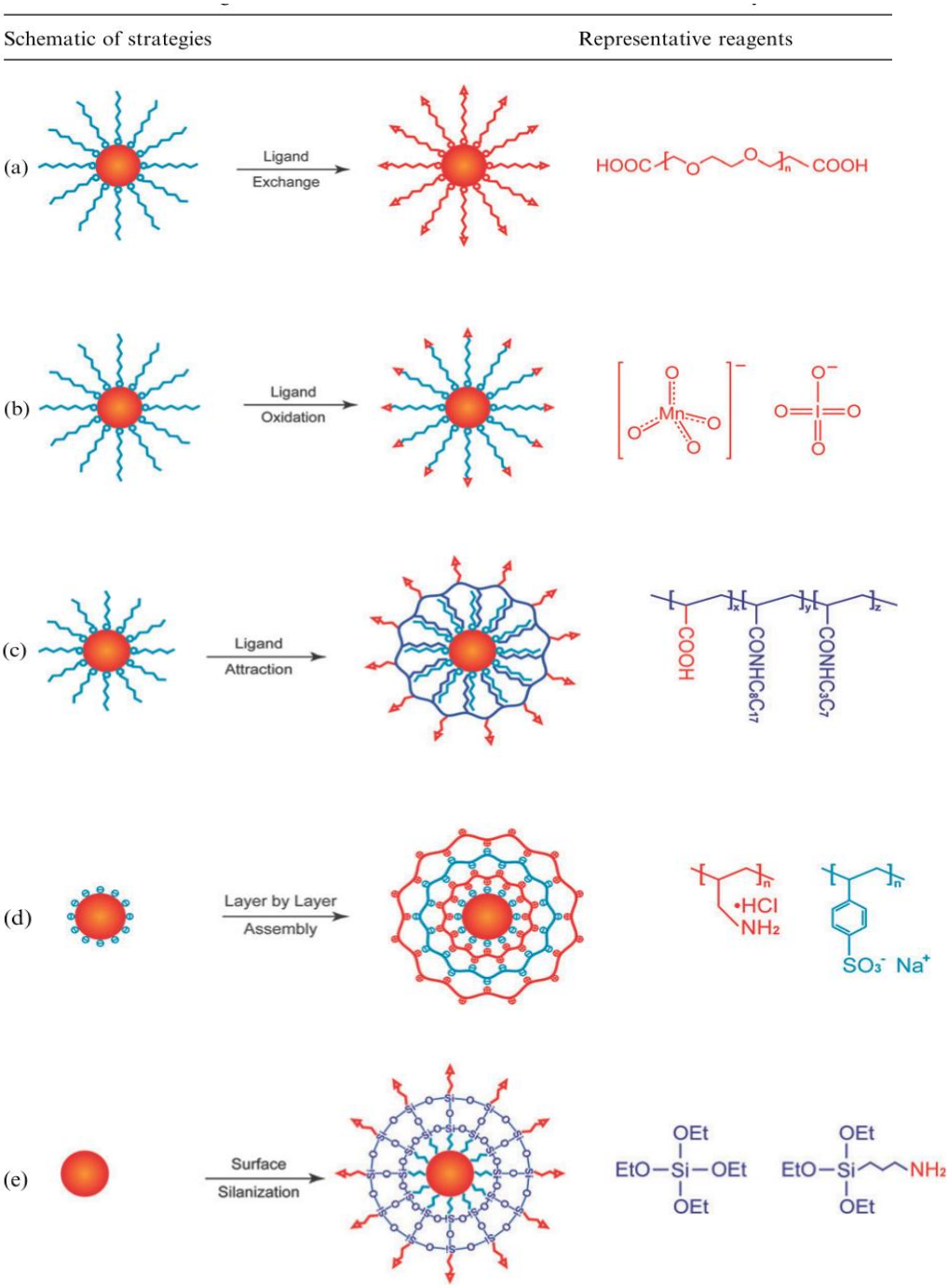

Silanization techniques provide a versatile and applicable for both hydrophobic and hydrophilic NCs. The Stober method is a popular silanization technique for hydrophilic NPs while reverse-microemulsion technique has been adopted for silanization of hydrophobic NPs.[187] The silanization process is based on the hydrolysis and polycondensation of silica precursor (e.g. tetraethoxysilane, TEOS) in presence of alkali hydroxide (e.g. ammonium hydroxide, NH_4OH). In the surface silanization process, organosilanes with amine functional groups are assembled onto NPs surface, making the NPs water-dispersible and biocompatible.[188] This method is attractive due to the biocompatibility of silica coating and can easily be conjugated to a wide range of biomolecules conveniently. Some example of silanization include silica coating of PVP-stabilized $NaYF_4$: Yb,Er [189] and a thin layer of silica formation on Fe_2O_3-CdSe magnetic quantum dots.[190]

2.5 Motivations of This Work

The development of multifunctional NPs for nanomedicine, specifically in integrated imaging and therapy, is still in its early age. However, their unique magnetic and UC fluorescence properties, coupled with the promise of high efficiency in detection, imaging and therapy have motivated the current work to undertake rational design strategies to conceptualize, synthesize and tailor novel classes of lanthanide nanomaterials.

Some of these nanomaterials will be capable of producing efficient UC fluorescence as well as strong MRI signals, especially in high magnetic field, which potentially can

lead to more accurate diagnosis. Nanomaterials are promising candidates as MRI contrast agents because they have the possibility to deliver high MRI relaxivity per molecular binding site. In high magnetic fields, a higher spatial resolution, better signal-to-noise ratio and reduced scanning time can be obtained. Furthermore, conventional contrast agents respond only in a single imaging mode and frequently encounter ambiguities in the MR images. A multimodal contrast agent that is tunable to different MRI modes and possesses excellent upconversion fluorescence is a potential disruptive technology that can contribute to greater understanding and improvement in designing bimodal imaging probes for future studies.

Furthermore, near-infrared (NIR) radiation is more suitable for bio-applications due to its low phototoxicity, low absorption and deep penetration of tissues. Using a NIR 980 nm laser, the upconversion emissions of lanthanides in the near UV and/or blue region can further excite QDs or nitrogen-doped TiO_2. This eliminates intrinsic problems associated direct UV or blue irradiation onto biological specimens. Such desirable property motivates us to design new upconverting lanthanide nanomaterials, such as multicolor upconverting lanthanide QDs as potential biolabels, and nontoxic upconverting lanthanide-titania photocatalyst for NIR-triggered drug release and cancer cells ablation.

Chapter 3: Synthesis Methodology and Characterization

This chapter describes the synthesis methodology and the characterization technique used throughout the study. The basic principles, operating conditions and methods of sample preparation will also be illustrated.

3.1 Synthesis Methodology

3.1.1 Dual Modal Ytterbium-enriched Lanthanide Nanocrystals Prepared via a Two-step Synthesis for Efficient Up-converting Fluorescence and High Field T_2 Magnetic Resonance Imaging

3.1.1.1 Chemicals

All chemicals were used directly without further purification. Yttrium (III) chloride hexahydrate (99.9%), ytterbium (III) chloride hexahydrate (99.9%), erbium (III) chloride hexahydrate (99.9%), dysprosium (III) chloride hexahydrate (99.9%), NaOH (reagent grade, 97%, beads), NH_4F (99.9%), sodium oleate (90%), octadecene (tech., 90%), oleic acid (tech., 90%), tetramethylammonium hydroxide (25wt% in methanol) (TMAH) and Igepal CO-520 (Polyoxyethylene (5) nonylphenylene), 3-aminopropyltrimethoxysilane (APS, 97%) were purchased from Sigma-Aldrich. Acetone, ethanol and hexane (AR grade) were purchased from VWR International Ltd.

3.1.1.2 Synthesis methodology

3.1.1.2.1 Synthesis of the seed $NaYF_4$: Yb^{3+}, Er^{3+} NPs

The method for preparation of $NaYF_4$:Yb^{3+}, Er^{3+} NPs were reported elsewhere. Briefly, lanthanide chloride hexahydrate (YCl_3 $6H_2O$ (0.8 mmol), $YbCl_3$ $6H_2O$ (0.18 mmol), $ErCl_3$ $6H_2O$ (0.02mmol)) were dissolved in 15 ml oleic acid and 15 ml 1-octadecene at 160 ℃ until a clear solution formed. The temperature was cooled to 50 ℃. A solution of 4 mmol NH_4F and 2.5 mmol NaOH in 10 ml methanol was added into the above solution and kept for 30 min. The methanol in the mixed solution was evaporated before the solution was degassed at 100 ℃ for 20 min, followed by heating it to 300 ℃ and maintaining it for 1h under N_2 gas. The solution was then allowed to cool down to room temperature, after which the $NaYF_4$: Yb^{3+}, Er^{3+} NPs could be precipitated out with acetone and centrifuged out of the solution. $NaYF_4$: Yb^{3+}, Er^{3+} NPs were dispersed in hexane.

3.1.1.2.2 Synthesis of the $NaYF_4$: Yb^{3+}, Er^{3+}/$NaDyF_4$: Yb^{3+} NPs

0.8 mmol $DyCl_3$ $6H_2O$ and 0.2 mmol $YbCl_3$ $6H_2O$ were dissolved in 15 ml oleic acid and 15 ml 1-octadecene at 160 ℃, 1mmol $NaYF_4$: Yb^{3+}, Er^{3+} NPs in 10 ml hexane were then added to the solution, and the hexane solution was removed by evaporation. While keeping the temperature at 50 ℃, a solution of 4 mmol NH_4F and 2.5 mmol NaOH in 10 ml methanol was added into the solution and kept for 30 min. The methanol in the mixed solution was evaporated before the solution was degassed at 100 ℃ for 20 min, followed by heating it to 300 ℃ and maintaining it for 1h under N_2 gas. The solution was then allowed to cool down to room temperature, after which the $NaYF_4$: Yb^{3+}, Er^{3+}/$NaDyF_4$: Yb^{3+} NPs could be precipitated out with acetone. The

final $NaYF_4$: Yb^{3+}, Er^{3+}/$NaDyF_4$: Yb^{3+} NPs were readily dispersed in organic solvents, such as hexane, cyclohexane, toluene or chloroform.

3.1.1.2.3 Silanization of the $NaYF_4$: Yb^{3+}, Er^{3+}/$NaDyF_4$: Yb^{3+} nanocomposites

Reverse micelles were prepared by dissolved 0.2 g of Igepal CO-520 in 4 ml of cyclohexane with vigorous stirring for 30 min, 1 ml of $NaYF_4$: Yb^{3+}, Er^{3+}/$NaDyF_4$: Yb^{3+}, Er^{3+} NPs (disperse in chloroform at 10 mg/ml) were then added to the micelle solution and stirred for 15 min. Subsequently, 60 μL of APS was added and the mixture was stirred for 1 h. Then 60 μL of TMAH in methanol was added. After additional 1 h of stirring, 30 μL of deionized water was added and stirred for 30 min. At this stage, globules of silanized NPs were formed and settled at the bottom of the flask. The globules were then collected and the transparent organic phase was discarded. Silanized NPs were washed with chloroform and ethanol for the complete removal of excess surfactant and other reactants. And final NPs were dispersed in deionized water.

3.1.2 A Strategy to Achieve Simultaneous Up-conversion Fluorescence and Tunable T_1-T_2 Magnetic Resonance Imaging Contrast in Lanthanide Nanocrystals

3.1.2.1 Chemicals

All chemicals were purchased from Aldrich, and used as received without further purification. Gadolinium (III) chloride hexahydrate (99.9%), ytterbium (III) chloride hexahydrate (99.9%), erbium (III) chloride hexahydrate (99.9%), dysprosium (III) chloride hexahydrate (99.9%), NaF (99.9%), sodium oleate (90%), octadecene (tech.,

90%), oleic acid (tech., 90%), tetramethylammonium hydroxide (25wt% in methanol) (TMAH) and Igepal CO-520 (Polyoxyethylene (5) nonylphenylene), 3-aminopropyltrimethoxysilane (APS, 97%) were purchased from Sigma-Aldrich. Acetone, ethanol and hexane (AR grade) were purchased from VWR International Ltd.

3.1.2.2 Synthesis methodology

3.1.2.2.1 Synthesis of the $NaDyF_4$:Yb^{3+} NPs

Thermal decomposition of lanthanide-oleate complex was used to synthesize the desired NRs. Briefly, dysprosium chloride hexahydrate (0.8 mmol) and ytterbium chloride hexahydrate (0.2 mmol) were dissolved in a solvent mixture composed of ethanol (7 ml), distilled water (7ml) and hexane (15 ml). The resulting solution was heated to 70 ℃, an excess (2 mmol) of sodium oleate was added into the solution and reacted at 70 ℃ for 4 h. When the reaction was completed, the upper organic layer containing the lanthanide-oleate complex was washed with distilled water in a separatory funnel three times. After washing, a complex in a solid waxy form was formed after evaporating off hexane. The lanthanide-oleate complex was then dissolved in oleic acid and 1-octadecane at room temperature. After adding sodium fluoride into the flask, the solution was degassed under vacuum with magnetic stirring for 30 min. After degassing to remove residual water and oxygen, the flask was purged with N_2 gas and then the reaction mixture was heated to 300 ℃ and kept at that temperature for 2 h. The resulting solution was cooled to room temperature and

the nanoparticles were obtained after washing with ethanol and hexane three times. Finally, the nanoparticles were dispersed in hexane.

3.1.2.2.2 Synthesis of the $NaDyF_4:Yb^{3+}/NaGdF_4:Yb^{3+}$, Er^{3+} nanocomposites

The core nanorods (1 mmol), Gd-oleate complex (0.8 mmol), NaF (5 mmol), Yb-oleate complex (0.18 mmol), Er-oleate complex (0.02 mmol), oleic acid (15 ml) with octadecene (15 ml) were mixed in three-necked reaction flask and stirred vigorously until the solution mixed well. The solution was degassed under vacuum with magnetic stirring for 30 min. Then, the flask was purged with N_2 and heated to 300 ℃, and kept at this temperature for 2 h under vigorous stirring to form the core/shell NRs. After the reaction, the solution was cooled down to room temperature, and washed with ethanol and hexane for three times. The NRs were obtained after washing and they were readily dispersed in organic solvents such as hexane, cyclohexane, toluene or chloroform.

3.1.2.2.3 Silanization of the $NaDyF_4:Yb^{3+}/NaGdF_4:Yb^{3+}$, Er^{3+} nanocomposites

Reverse micelles were prepared by dissolved 0.2 g of Igepal CO-520 in 4 ml of cyclohexane with vigorous stirring for 30 min, 1 ml of $NaDyF_4:Yb^{3+}/NaGdF_4:Yb^{3+}$, Er^{3+} NPs (disperse in chloroform at 10 mg/ml) were then added to the micelle solution and stirred for 15 min. Subsequently, 60 μL of APS was added and the mixture was stirred for 1 h. Then 60 μL of TMAH in methanol was added. After additional 1 h of stirring, 30 μL of deionized water was added and stirred for 30 min. At this stage, globules of silanized NPs were formed and settled at the bottom of the flask. The

globules were then collected and the transparent organic phase was discarded. Silanized NPs were washed with chloroform and ethanol for the complete removal of excess surfactant and other reactants. And finally NPs were dispersed in deionized water.

3.1.3 Color-tunable Up-conversion Emitting Yb,Tm Codoped $NaYF_4$/CdSe Core/shell Nanocomposites

3.1.3.1 Chemicals

All chemicals were purchased from Aldrich, and used as received without further purification. Yttrium (III) chloride hexahydrate (99.9%), ytterbium (III) chloride hexahydrate (99.9%), Thulium (III) chloride hexahydrate (99.9%), NaOH (99.9%), NH_4F (99%), octadecene (tech., 90%), oleic acid (tech., 90%), CdO (99.9%), stearic acid (99%), TOPO (90%), HAD (90%), Se (99.9%) and TOP (90%) were purchased from Sigma-Aldrich. Toluene, methanol, ethanol (AR grade) and cyclohexane were purchased from VWR International Ltd.

3.1.3.2 Synthesis Methodology

3.1.3.2.1 Synthesis of $NaYF_4:Yb^{3+},Tm^{3+}$ NPs

The synthesized ß-$NaYF_4:Yb^{3+},Tm^{3+}$ NPs via a modified literature procedure.[191] Typically, 0.8 mmol of $YCl_3.6H_2O$, 0.2 mmol of $YbCl_3.6H_2O$, 0.002 mmol of $TmCl_3.6H_2O$ were mixed in a 100 ml flask with 15 ml oleic acid and 15 ml of 1-octadecene. The mixture were stirred at 160 ℃ for 30 min. Afterward, the mixture was cooled down to room temperature and a solution of 2.5 mmol NaOH and 4 mmol

NH_4F dissolved in 10 ml methanol was added and stirred for 30 min at 80 ℃ to remove methanol and then heated to 300 ℃ under nitrogen flow for 1.5 h. The resulting mixture cooled to room temperature, precipitated and washed with ethanol and the synthesized nanocrystals dried at 70 ℃ for subsequent CdSe shell growth.

3.1.3.2.2 Synthesis of the $NaYF_4:Yb^{3+},Tm^{3+}$-CdSe Core/Shell nanocomposites

$NaYF_4:Yb^{3+},Tm^{3+}$-CdSe core/shell nanocomposites were synthesized using a method developed by Selvan et al. with some modifications.[192] 20 mg of CdO and 180 mg of stearic acid were taken in a 100 ml 3-neck flask and stirred slowly. The mixture was purged with nitrogen for 30 min and then heated to 180 ℃ to form Cd-stearate complex. The complex cooled to room temperature. 30 mg of as-synthesized dried $NaYF_4:Yb^{3+},Tm^{3+}$ NPs together with 7.76 g TOPO and 7.76 g HAD were added to this complex. The resulting mixture was then heated to 300 ℃ under nitrogen flow. At 300 ℃, a solution of 39.5 mg of Se powder dissolved in 1.2 ml of TOP was quickly injected. The shell of the CdSe nanocrystals made of individual nanocrystals grown very quickly after injection. Samples were quickly collected by a syringe and then put in 10 ml toluene to stop further growth. The green, yellow and red emitting CdSe shell were grown at 30, 50, and 120 s after injection of the Se precursor. Finally, the samples were washed with ethanol and chloroform several times and dispersed in cyclohexane for further characterizations.

3.1.4 Anti-cAngptl4 Ab-conjugated N-TiO_2/$NaYF_4$:Yb^{3+},Tm^{3+} Nanocomposite Near Infrared-Triggered Drug Release and Enhanced Targeted Cancer Cell Ablation

3.1.4.1 Chemicals

Ethylene glycol (EG, 99%), NaCl (99%), YCl_3 $6H_2O$ (99.9%), $YbCl_3$ $6H_2O$, $TmCl_3$ $6H_2O$, Branched polyethyleminine (PEI, 25 KDa), thioglycolic acid, titanium n-butoxide, HNO_3 solution (69%), acetyl acetone, NH_4F (99%), terephthalic acid (99%), NaOH (99%) and 7-methoxycoumarin-3-carboxylic acid were purchased from Sigam-Aldrich Co. Isopropanol, toluene, triethylamine and dimethyl sulfoxide were purchased from Merck. 3-Aminopropyltriethoxysilane was purchased from Alfa Aesar.

3.1.4.2 Synthesis Methodology

3.1.4.2.1 Preparation of Yb, Tm-doped $NaYF_4$ NPs

The synthesis of ß-$NaYF_4$:Yb^{3+},Tm^{3+} NPs were synthesized via a modified literature procedure.[191] Typically, 1.2 mmol of NaCl, 0.48 mmol of YCl_3 $6H_2O$, 0.108 mmol of $YbCl_3$ $6H_2O$, 1 µmol of $TmCl_3$ $6H_2O$ and 0.15 g of PEI were dissolved in 9 mL EG solvent. The mixture solution was dropped into a stoichiometric amount of NH_4F in 6 mL of EG. The resulting mixture was agitated for another 10 min, then transferred to a 20 mL Teflon-lined autoclave, and subsequently heated at 200 ℃ for 2 h. Acetone was added into the obtained solution and the $NaYF_4$:Yb^{3+},Tm^{3+} NPs were collected by centrifugation. Finally, the $NaYF_4$:Yb^{3+},Tm^{3+} NPs were washed with ethanol and DI water for several times, and dispersed in DI water at concentration of 1.0 wt%.

3.1.4.2.2 Preparation of N-doped TiO_2 NPs (N-TiO_2) and Thioglycolic Acid Functionalized N-TiO_2 NPs (TGA-N-TiO_2)

Pure N-TiO_2 NPs were prepared by a hydrothermal reaction. Typically, a mixture of 5.0 mL of titanium n-butoxide and 5.0 mL of isopropyl alcohol was added dropwise into 30 mL HNO_3 solution (0.2 M) containing 1.0 mL of acetyl acetone, and kept continuous stirring for 12 h. After that, 5.0 mL of triethylamine was added into the mixture solution and kept continuous stirring for another 12 h. Then, the mixture was put into a Teflon-lined stainless autoclave and hydrothermally treated at 160 ℃ for 12 h. The powder was filtered, washed with DI water five times. The N-TiO_2 NPs was treated with thioglycolic acid (TGA) at room temperature and kept continuous stirring for 3 h. After that the TGA-N-TiO_2 was washed with DI water for several times and dispersed on DI water at concentration of 1.0 wt%.

3.1.4.2.3 Preparation of N-TiO_2/$NaYF_4$:Yb^{3+},Tm^{3+} NPs

The $NaYF_4$:Yb^{3+},Tm^{3+} NPs and TGA-N-TiO_2 (w/w = 2/1) were mixed in 50 mL DI water and heated at 160 ℃ for 3 h. Then the N-TiO_2/$NaYF_4$:Yb^{3+},Tm^{3+} NPs were collected by centrifugation (10000 rpm, 5 min) and washed with DI water for several times. Finally, the obtained yellow powder was dried in an oven at 70 ℃ for 12 h.

3.1.4.2.4 Detection of Photogenerated OH Radicals

Typically, 10 mg of N-TiO_2/$NaYF_4$:Yb^{3+},Tm^{3+} NPs were added in 5 mL mixture solution of terephthalic acid (8 X 10^{-4} M) and NaOH (4 X 10^{-4} M). The mixture was ultrasonicated for 30 min to disperse the N-TiO_2/$NaYF_4$:Yb^{3+},Tm^{3+} NPs uniformly in

the solution. Then the mixture was irradiated with a NIR laser (power = 3 W and λ = 980 nm). At every 30 min, 0.5 mL of the suspension was collected and centrifuged (10000 rpm, 5 min). Then 0.3 mL of the transparent solution was diluted 20 times for the PL measurement. The concentration of hydroxyterephthalate anion was measured by fluorometer (Fluoromax-4 Spectrophotometer, Horiba Jobin Yvon) with an excitation wavelength of 320 nm. Pure N-TiO_2, $NaYF_4$:Yb^{3+},Tm^{3+} and blank were also analyzed under the same conditions for comparison.

3.1.4.2.5 Photocatalytic Activities Measurement

The photocatalytic activities of the N-TiO_2/$NaYF_4$:Yb^{3+},Tm^{3+}, N-TiO_2 and $NaYF_4$:Yb^{3+},Tm^{3+} NPs were measured by the degradation of methylene blue (MB) in an aqueous solution. 10 mg of sample was suspended in a 5 mL aqueous solution of MB (10 ppm). Prior to irradiation, the suspension was stirred in the dark for 24 h to establish an adsorption/desorption equilibrium between the photocatalyst and MB. Then the mixture was irradiated with a NIR laser (BWOF-2, B&W TEK Inc., power = 2 W and λ = 980 nm) for different hours. The concentration variation of MB was obtained according to the concentration-absorbance (at λ = 664 nm) relationship. At 6 h intervals, 3.0 mL MB aqueous was taken out and placed in the UV-Vis spectrophotometer for analysis, and then put back after measurement was taken.

3.1.4.2.6 Attachment of Fluorescent Dye on N-TiO_2/$NaYF_4$:Yb^{3+},Tm^{3+} NPs

A modified method was used to attach a fluorescent dye on the N-TiO_2/$NaYF_4$:Yb^{3+},Tm^{3+} NPs. Firstly, the N-TiO_2/$NaYF_4$:Yb^{3+},Tm^{3+} NPs were

refluxed in 10 mM 3-aminopropyltriethoxysilane (APTES) -toluene solution for 24 h at 70 ℃, which led to a saturated APTES monolayer on the surface of the N-TiO_2/$NaYF_4$:Yb^{3+},Tm^{3+} NPs. Then the APTES-N-TiO_2/$NaYF_4$:Yb^{3+},Tm^{3+} NPs were collected by centrifugation and washed with dimethyl sulfoxide (DMSO) for several times. After that the APTES-N-TiO_2/$NaYF_4$:Yb^{3+},Tm^{3+} NPs were refluxed in a fluorescent dye (7-methoxycoumarin-3-carboxylic acid)-DMSO solution for 2 h at 70 ℃. Finally, the yellow precipitate was collected by centrifugation, cleaned by immersing in DMSO for 30 min and dried at 70 ℃ for 24 h.

3.1.4.2.7 NIR-triggered Release of Dye

14.0 mg of fluorescent dye-modified N-TiO_2/$NaYF_4$:Yb^{3+},Tm^{3+} NPs were suspended in a 3.5 mL DI water in a quartz cuvette. The mixture was ultrasonicated for 30 min to disperse the powder uniformly in the solution. Then the mixture was irradiated with a NIR laser. After 10 min, 3.0 mL of the suspension was collected and centrifuged. The transparent solution was diluted 20 times for the PL measurement with an excitation wavelength of 320 nm. In order to confirm that no dye was released without NIR irradiation, 7.0 mg of fluorescence dye-modified N-TiO_2/$NaYF_4$:Yb^{3+},Tm^{3+} NPs were immersed in a 3.5 mL DI water for 2 h. After removing the powder, the water was irradiated with UV laser, but no fluorescence was detected.

3.2 Characterization Techniques

3.2.1 Transmission Electron Microscopy (TEM)

Transmission electron microscopy (TEM) is a microscopy technique which operates on the same basic principles as the light microscope but uses electrons instead of light. The use of electrons makes it possible to get a resolution a thousand times higher than that of a light microscope.

An electron gun at the top of the microscope ejects the electrons that travel through a vacuum in the column of the microscope towards the specimen. Instead of using glass lenses to focus the light in the light microscope, a TEM uses electromagnetic lenses to focus the electrons into a very fine beam. Depending on the density of the material present, some of the electrons are scattered while some penetrates through the sample. The unscattered electrons hit a fluorescent screen at the bottom of the microscope, which give rise to a shadow that provides morphological features at low resolution and lattice/atomic arrangements at high resolution for nanostructured materials. The image can be studied directly or photographed with a charge couple device (CCD) camera. In addition, this technique can be very powerful in providing electron diffraction patterns, and elemental information of the specimen. The electron diffraction X-ray spectroscopy (EDS) data can be collected with a nanometer resolution, which enables the construction of detailed elemental maps of the nano-object under study.

For the specimen preparation in current study, a few drops of NPs were dispersed onto a holy carbon film supported one 200 mesh copper grid and were allowed to dry in air

at room temperature. The carbon grid with sample was then mounted into the vacuum chamber for imaging and selected area electron diffraction (SAED). The observation was carried out in JOEL JEM-2100F microscope, operating at an accelerating voltage of 200kv.

3.2.2 Energy-dispersive X-ray (EDX) Analysis

The energy-dispersive x-ray analysis (EDS or EDX) is an analytical technique used for the elemental analysis or chemical characterization of a sample. It relies on the investigation of sample through interaction between electromagnetic radiation and matter, analyzing x-rays emitted by the matter in response to being hit with charged particles. Its characterization capabilities are due in large part to the fundamental principle that each element has a unique atomic structure allowing x-rays that are characteristic of an element's atomic structure to be identified uniquely from one another.

A high energy beam of charged particles such as electrons or protons or a beam of x-rays is focused into the sample to stimulate the emission of characteristic x-rays from a specimen. At rest, an atom within the sample contains ground state electrons in discrete energy levels or electron shells bound to the nucleus. The incident beam may excite an electron in an inner shell, ejecting it from the shell while creating an electron hold where the electron was. An electron from an outer, higher-energy shell then fills the hold, and the difference in energy between the higher-energy shell and the lower energy shell may be released in the form of an X-ray. The number and energy of the

X-rays emitted from a specimen can be measured by an energy-dispersive spectrometer. As the energy of the X-rays is characteristic of the difference in energy between the two shells, and of the atomic structure of the element from which they were emitted, this allows the elemental composition of the specimen to be measured.

3.2.3 Spectrofluorophotometer

Luminescence arises from the emission of photons from a substance that is at electronically excited states as discussed earlier in section 2.3.2, 2.3.4 and 2.3.5. In this study, only up-conversion fluorescence of the lanthanide NPs has been investigated. NPs samples were dispersed in cyclohexane in a standard square quartz cuvette at room temperature. The up-conversion fluorescence spectra were obtained using a Fluoromax-4, Horiba Jobin Yvon Spectrofluorometer, which employs a photon-counting detecting system for the detection of fluorescence emission. To obtain emission spectra, sample excitation was accomplished using a diode laser, BWF-2 (980 nm, P_{max} = 2.0W at 3.0 A, B&W TEK Inc) couple to a 100 μm (core) optical fiber. The emission spectra in the visible region were obtained with a resolution of 1 nm and a laser power of 0.75 W.

3.2.4 Powder X-ray Diffraction (XRD) Analysis

Powder X-ray diffraction (XRD) is an analytical technique primarily used for phase identification of a crystalline material and can provide information about unit cell. X-ray diffraction is based on constructive interference of monochromatic X-rays and a crystalline sample. These X-rays are generated by a cathode ray tube, filtered to

produce monochromatic radiation, collimated to concentrate and direct toward the sample. The interaction of the incident X-rays with the sample produces constructive interference (and a diffracted ray) when conditions satisfy Bragg's law:

$$n\lambda = 2d \sin\theta \qquad \text{(Eq 3.1)}$$

Where:

λ is the wavelength of incident X-ray;

d is the crystal plane distance;

θ is the diffraction angle.

Bragg's law relates the wavelength of electromagnetic radiation to the diffraction angle and the lattice spacing in a crystalline sample. These diffracted X-rays are then detected, processed and counted. By scanning the sample through a range of 2θ angles, all possible diffraction directions of the lattice should be attained due to the random orientation of the powdered materials. Conversion of the diffraction peaks of d-spacing allows identification of the materials because each material has a set of unique d-spacing. Typically, this is achieved by comparison of d-spacing with standard reference patterns.

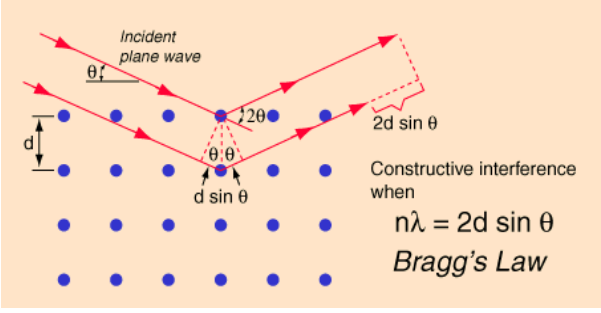

Figure 3.1 Bragg's law and the interaction of the X-rays with the atoms in crystal.[193]

In a powder XRD, the sample is prepared in the form of fine homogenous powder. As a result, the sample contains a large collection of very small crystals which should be orientated in every possible direction relative to the beam of radiation. For the specimen preparation in this study, approximately, 40-50 mg of a sample of the NPs were then spread mortar to break up lumps. The powdery samples of the NPs were then spread evenly onto a zero-background holder. Step-scan X-ray power diffraction data were collected over the range of 2θ of 10-85^{o} On a D8 Advance Bruker powder X-ray diffractometer with Cu Ka (operated at 40 kV, 40 kA) radiation (λ = 0.15406 nm) with 6 nm divergence slit, 1 mm scattering slit, and 0.2 mm receiving slit. The scanning step size is 0.02^{o} in 2θ with a counting time of 1 s per step.

The diffraction peaks can be used to calculate the average crystallite size, Dp by Scherrer Formula:

$$Dp = K\lambda / FWHM \cos\theta \qquad \text{(Eq. 3.2)}$$

Where:

K: the Scherrer constant that falls in the range of 0.87-1.0;

λ: the wavelength of X-ray;

FWHM: full width at half maximum of the diffraction peaks;

θ: the diffraction angles.

3.2.5 Inductive Coupled Plasma-Atomic Emission Spectroscopy (ICP-AES)

The principle of this analytical technique is based on the excitation of electrons of the element by electronically generated plasma to higher level of energies above the ground state. Plasma is an electrically neutral, highly ionized gas that consists of ions, electrons and atoms. When an electron returns to ground state, a photon with a particular wavelength corresponding to the difference in the energy levels is emitted. There is an empirical correlation between the powers of the emitted radiation to the quantity of the corresponding element in the sample. Such information is then used to generate a mass spectrum for the quantitative analysis of inorganic components in a solution. In this work, the solid samples were first dissolved in 2% nitric acid solution to obtain clear solutions containing metal cations of the samples. The measurement was conducted in a Teledyne Prodigy ICP-AES using argon plasma as an excitation source.

3.2.6 Magnetic Resonance Imaging (MRI)

MRI is a non-invasive diagnostic tool which has an excellent spatial resolution and is harmless to human body. The basic principle of MRI is based on nuclear magnetic resonance (NMR) together with the relaxation of proton spins in a magnetic field. In MRI, contrast agents have been widely used to enhance image contrasts. The basic principles of MRI have been discussed early in section 2.2.1.

In this study, we conducted *in vitro* MRI for lanthanide nanomaterials, T_1- and T_2-weighted images were obtained on a Varian 7 T MRI system. All samples were

dissolved in double distilled water. The repetition (TR) and echo time (TE) values were optimized for T_1-weighted while using a spin echo sequence. Other parameters used for imaging are: number of acquisitions = 25, field of view = 35 mm, slice thickness = 3 mm, and acquisition time ~ 6 min/sample. All experiments were performed in 1% agarose medium.

3.2.7 X-ray Photoelectron Spectroscopy (XPS)

X-ray photoelectron spectroscopy (XPS) is an analysis technique used to obtain chemical information about the surfaces of solid materials. Both composition and the chemical states of surface constituents can be determined by XPS. The sample is placed in an ultrahigh vacuum environment and exposed to a low-energy, monochromatic X-ray source. The incident X-ray causes the ejection of core-level electrons from sample atoms. The energy of a photoemitted core electron is a function of its binding energy and is characteristic of the element from which it is emitted. Energy analysis of the emitted photoelectrons is the primary data used for XPS. When the core electron is ejected by the incident x-ray, an outer electron fills the core hole. The energy of this transition is balanced by the emission of an Auger electron (Figure 3.2) or a characteristic X-ray. Analysis of Auger electrons can be used in XPS, in addition to emitted photoelectrons. The photoelectrons emitted from the sample are detected by an electron energy analyzer, and their energy is determined as a function of their velocity entering the detector. By counting the number of photoelectrons as a function of their energy, a spectrum representing the surface composition is obtained. The energy corresponding to each peak is characteristic of an element presented in the

sample volume. The area under a peak in the spectrum is a measure of the relative amount of the element represented by that peak. The peak shape and precise position indicates the chemical state for the element. XPS is a surface sensitive technique because only those electrons generated near the surface escape and are detected. The photoelectrons of interest have relatively low kinetic energy. Due to inelastic collisions within the sample's atomic structure, photoelectrons originating more than 20 to 50 A below the surface cannot escape with sufficient energy to detect.

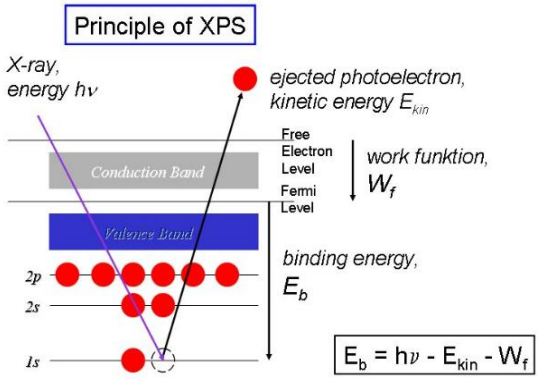

Figure 3.2 A scheme showing the principles of X-ray photoelectron spectroscopy.[194]

Mathematically, bombarding a sample in vacuum with x-rays gives rise to the emission of electrons. If monochromatic X-rays are used with a photon energy hυ, the kinetic energy (KE) of the emitted electrons is given by:

$$KE = h\upsilon - BE - \varphi \qquad \text{(Eq. 3.3)}$$

Where:

BE: the binding energy of the atomic orbital from which the electron originates

φ: the work function, it is the minimum amount of energy an individual electron needs to escape from the surface. Each element produces a unique set of electrons with

specific energies. By measuring the number of these electrons as a function of kinetic (or binding) energy, an XPS spectrum is obtained.

The XPS spectra presented in this report were collected from a VGESCALAB 250 spectrometer using a monochromatic A1 Ka X-ray source (1486.6 eV) operating at 15 kv and a pressure of 10-9 torr. Samples were finely ground before being mounted onto the adhesive tape. BEs of all elements were corrected by referring to the C 1s PEAK (BE of 284.6 eV) that was sputtered on the samples under study.

3.2.8 Fourier Transform Infrared (FTIR) Spectroscopy

Qualitative infrared spectroscopy is one of the most powerful tools for the analysis of compounds or moieties in a sample. This is achieved by recognizing characteristic shapes and patterns within the spectrum. The generated spectrum is formed as a consequence of the absorption of electromagnetic radiation at frequencies that correlate to the rotational and vibrational motions of specific chemical bonds within a molecule. Molecular bonds vibrate at various frequencies depending on the elements and types of the bonds. For a given bond, there are several specific frequencies at which it can vibrate. According to quantum mechanics, these frequencies correspond to the ground state (lowest frequency) and several excited states (higher frequencies). One way to increase the frequency of a molecular vibration is to excite the bond by absorption. By interpreting the infrared absorption spectrum, the chemical bonds in a molecule can be determined. The FTIR spectra of pure compounds are generally unique and therefore can be used as molecular fingerprints.

The potassium bromide (KBr) pellet technique is widely used for solid sample analysis. In this work, a few milligrams of finely ground sample were mixed with KBr powder with a mass molecular ratio of about 1:100. The mixture was then palletized before the measurement. The measurement was conducted in a Digilab FTS 3100 instrument by collecting 64 scans with a resolution of $4cm^{-1}$ at the mid-infrared region (400-4000 cm^{-1}). In this work, FTIR was used to analyze the chemical bonding information of metal-oxygen, the surfactants absorbed, and silica coating layer on the surface of the NPs.

3.2.9 UV-Vis-NIR Diffuse Reflectance Spectra (DRS)

A UV-Vis-NIR diffuse reflectance spectrum (DRS) is used for optical absorbance and reflectance measurements in the wavelength range (175-3300 nm). In principle, the technique is similar to IR-absorbance i.e, when a sample of an unknown compound is exposed to light, certain functional groups within the molecule absorb light of different wavelengths in the UV or visible or NIR region. The data were obtained using a CARY 5000 UV-Vis-NIR spectrophotometer (VARIAN).

Chapter 4: Dual Modal Ytterbium-Enriched Lanthanide Nanocrystals for Efficient Up-converting Fluorescence and High Field T_2 Magnetic Resonance Imaging

4.1 Introduction

Multifunctional lanthanide nanocrystals (NCs) that can be used in both magnetic resonance imaging (MRI) and fluorescence imaging is an emerging research topic due to their potential application as novel drug-delivery vehicles, imaging and diagnostic agents.[23,195-197] These NCs ally the excellent spatial resolution and great tissue penetration depth of MRI to high sensitivity of fluorescence imaging.[198] As imaging probes in fluorescence imaging, lanthanide NCs exhibit multicolor sharp fluorescent emission with high quantum yield, long life-time (μs-ms), high photostability and low toxicity when compared with other fluorophores (dyes, fluorescent proteins, lanthanide chelats, QDs).[23,24] In addition, by doping with the appropriate lanthanide ions, they can up-convert NIR photons into UV, visible or NIR region, either through a non-linear two-photon absorption process or by a sequential absorption of photons via the formation of a long-lived intermediate state.[23] Biological molecules are almost optically transparent in NIR region. Many lanthanide NCs, such as oxides, phosphate, fluorides, vanadates, have been employed as the doping matrix for lanthanide ions to achieve the desirable up-conversion (UC).[199-203] In particular, lanthanide fluorides are excellent host materials due to their high chemical stability, low phonon energies

(~350 cm^{-1}) and they are capable of suppressing non-radiative multiphonon relaxation processes which can be responsible for the improvement of the luminescence of the dopant.[204] Till now, hexagonal phase $NaYF_4$: Yb^{3+},Er^{3+} (or Tm^{3+}) NCs are known as one of the most effective up-converting NCs, in which Yb^{3+} ions absorb NIR photons and Er^{3+} or Tm^{3+} ions emit photons of higher energy.

Lanthanide ions, such as Gd^{3+}, Dy^{3+}, Pr^{3+}, Sm^{3+}, Ho^{3+}, can alter the relaxation of water protons of the nearby tissues, which can potentially be used as contrast agents in MRI.[12,21] MRI has become a common and noninvasive clinical imaging technique for obtaining topographic images of tissues with a high spatial resolution. Contrast agents are commonly used as they greatly alter proton relaxation rates and enhance visualization of the differences between normal and disease tissues. The contrast agents can be positive (examples are paramagnetic materials such as Gd-complex, Gd NCs, manganese oxide NCs), which induce brightness by shortening the longitudinal relaxation time (T_1), or negative (such as superparamagnetic iron oxide (SPIO) NCs), which produce darken MR images by shortening of the transverse relaxation time (T_2) of the surrounding water protons.[21] There is a trend in using higher magnetic field strength MRI to obtain a higher spatial resolution, better signal-to-noise ratio and reduced scanning time.[205] However, at high magnetic field, both paramagnetic T_1 contrast agents (such as the Gd^{3+}-based chelates) and superparamagnetic T_2 contrast agents (such as SPIO NCs) exhibit poor water relaxivity and low magnetization, as compared to those at low magnetic field.[205] Dy^{3+} ions are an exception owing to the relaxation induced via a Curie Relaxation which increases significantly with the

external magnetic field, and is proportional to the square of the magnetic moment of the lanthanide ions.[206] Besides, Dy^{3+} ions have the shortest electronic relaxation time (~ 0.5 ps) and highest magnetic moment (10.4 u_B) which can induce a large shortening of the transverse relaxation time T_2, resulting in very efficient T_2 relaxation. However, Dy^{3+} is a "poison" to UC due to the depopulation of multiple excited states in Yb^{3+} and Er^{3+} ions.

In search for a new type of nanosize contrast agent that is capable of incorporating the unique features of trivalent paramagnetic Dy^{3+} ions and UC properties of Yb^{3+}, Er^{3+} ions, we undertook structural and compositional design of a lanthanide based NC system and herein report Yb^{3+} enriched lanthanide NCs, $NaYF_4:Yb^{3+},Er^{3+}/NaDyF_4:Yb^{3+}$ with efficient UC fluorescence and high field T_2 MR imaging contrast enhancement. The $NaYF_4$: Yb^{3+},Er^{3+} NPs were first synthesized by a thermal decomposition method and then served as seeds for a secondary growth of the $NaDyF_4:Yb^{3+}$ layer. Yb^{3+} ions are included in both stages of growth to enhance the sensitizing effect. Yb^{3+} ion is an ideal co-dopant ion which possesses single excited state that can be easily excited using 980 nm. The absorption cross-section of the excited state of the Yb^{3+} ions is significantly greater than many of the excited states of other lanthanides with similar energy levels, rendering the UC or energy transfer process more efficient. The rational to have a secondary "magnetic layer" grown on the first layer is to separate the quencher Dy^{3+} ions from the emitter Er^{3+} ions, and to provide a passivating layer to reduce surface defects around the luminescent ions arising from the small seed particle size, thus reducing the non-radiative pathways.

Therefore, the resultant $NaYF_4:Yb^{3+},Er^{3+}/NaDyF_4:Yb^{3+}$ NCs show strong UC fluorescence and induce a simultaneous T_2 negative MR contrast, making them useful as dual modal up-converting fluorescence and T_2- weighted MR imaging probes.

4.2 Results and Discussion

$NaYF_4:Yb^{3+},Er^{3+}/NaDyF_4:Yb^{3+}$ NCs were synthesized via a two-step procedure. Figure 4.1 shows transmission electron microscopy (TEM) images of the $NaYF_4:Yb^{3+},Er^{3+}/NaDyF_4:Yb^{3+}$ NCs before and after a secondary growth. From the TEM images (Figure 4.1 A the TEM images of $NaYF_4:Yb^{3+},Er^{3+}$ seed NCs; B, the TEM images of $NaYF_4:Yb^{3+},Er^{3+}/NaDyF_4:Yb^{3+}$ NCs), all the observed as-obtained $NaYF_4:Yb^{3+},Er^{3+}$ and $NaYF_4:Yb^{3+},Er^{3+}/NaDyF_4:Yb^{3+}$ NCs are of single-crystalline and display relatively size uniformity, of average diameters of 37 nm and 55 nm, respectively. The $NaYF_4:Yb^{3+},Er^{3+}$ seed NCs display hexagonal shape while the $NaYF_4:Yb^{3+},Er^{3+}/NaDyF_4:Yb^{3+}$ NCs display spherical shape. The increases in size and shape evolution indicate the formation of the $NaDyF_4:Yb^{3+}$ secondary layer. The compositional analyses by Energy-dispersive X-ray spectroscopy (EDS) reveal the presence of the elements of Na, Y, F, Yb, Er in the seed particle and additional peaks of Dy in the final, further proving that $NaDyF_4:Yb^{3+}$ layer has been successfully formed onto the $NaYF_4:Yb^{3+},Er^{3+}$ seed NCs (Figure 4.2). The structure of $NaYF_4:Yb^{3+},Er^{3+}$ and $NaYF_4:Yb^{3+},Er^{3+}/NaDyF_4:Yb^{3+}$ NCs was further confirmed by X-ray powder diffraction (XRD) analysis, as shown in Figure 4.3. All the XRD peaks and intensities for both NCs are consistent with the standard pattern of hexagonal phase $NaYF_4$ crystals (JCPDS. No 16-0334). The Y: Dy molar ratio was determined to

be 40.2: 40 by inductively coupled plasma (ICP) spectroscopy, which is the stoichiometric ratio for the chloride precursors used in the experiment.

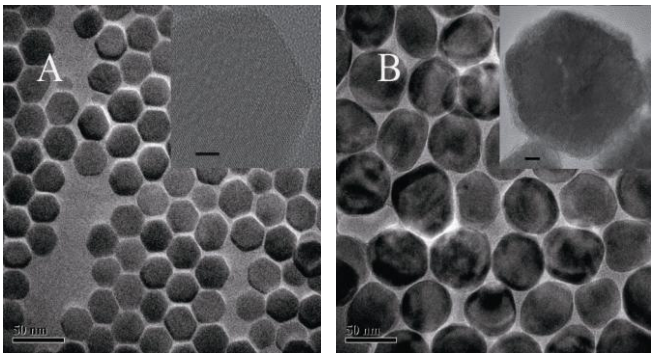

Figure 4.1 TEM images of $NaYF_4:Yb^{3+},Er^{3+}$ (A) and $NaYF_4:Yb^{3+},Er^{3+}/NaDyF_4:Yb^{3+}$ (B) NCs. Inset: HRTEM images (scale bar for insert images: 5 nm).

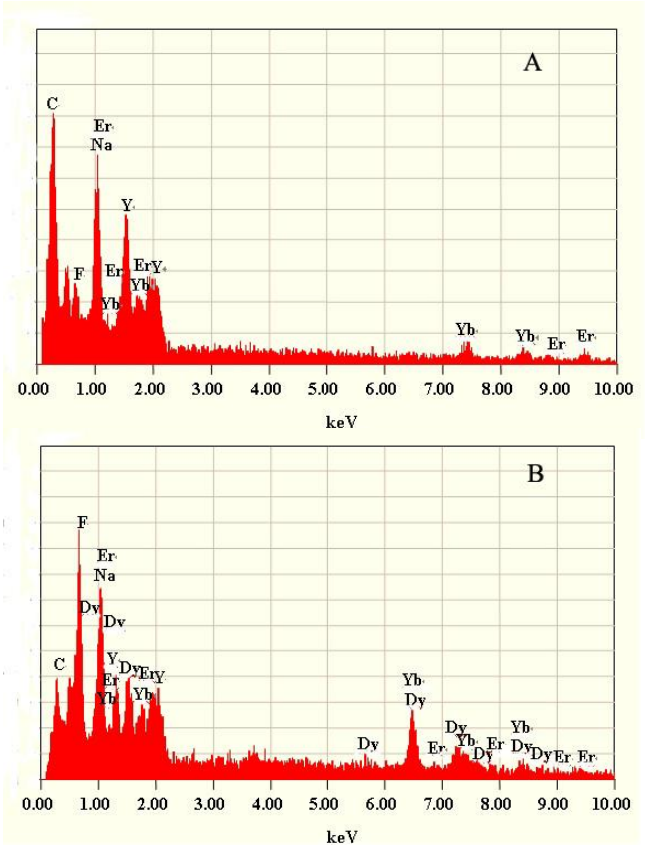

Figure 4.2 EDS analysis of elemental composition of (A) $NaYF_4:Yb^{3+},Er^{3+}$ and (B) $NaYF_4:Yb^{3+},Er^{3+}/NaDyF_4:Yb^{3+}$ NCs.

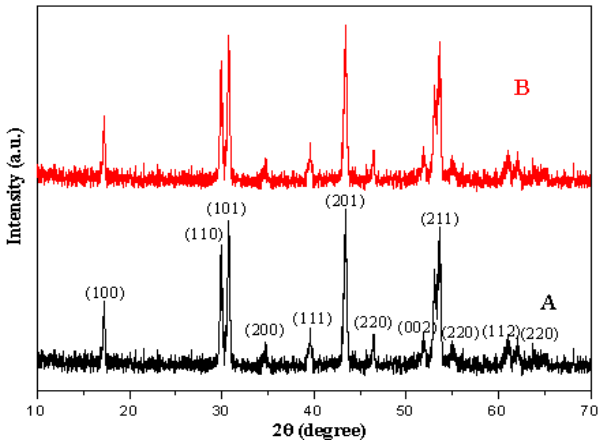

Figure 4.3 XRD patterns of as-synthesized (A) β-$NaYF_4$:Yb^{3+},Er^{3+} and (B) $NaYF_4$:Yb^{3+},Er^{3+}/$NaDyF_4$:Yb^{3+} NCs.

The UC emission spectra are shown in Figure 4.4. Four types of NCs: (A) seed only $NaYF_4$:Yb^{3+},Er^{3+}; (B) $NaYF_4$:Yb^{3+},Er^{3+}/$NaDyF_4$:Yb^{3+}; (C) $NaYF_4$:Yb^{3+},Er^{3+}/$NaDyF_4$ (Yb^{3+} absent in second layer) and (D) triple doped $NaYF_4$: Yb^{3+},Er^{3+},Dy^{3+} NCs were synthesized to show the feasibility of the strategy. There are no characteristic emission lines of Dy^{3+} ions in the wavelength regions of 470-500 nm and 570-600 nm, indicating that Yb^{3+} and Dy^{3+} ions act as sensitizers and Er^{3+} ions act as emitters. Dominant green fluorescence was observed at 523 and 546 nm, corresponding to the transition from $^2H_{11/2}$ and $^4S_{3/2}$ excited states to the $^4I_{15/2}$ ground state, respectively. Red UC luminescence was observed at 659 nm due to the transition from $^4F_{9/2}$ excited state to $^4I_{15/2}$ of Er^{3+} ions. The intense green color fluorescence, as shown in Figure 4.5, is mainly due to the much stronger green emissions than that of the red ones.

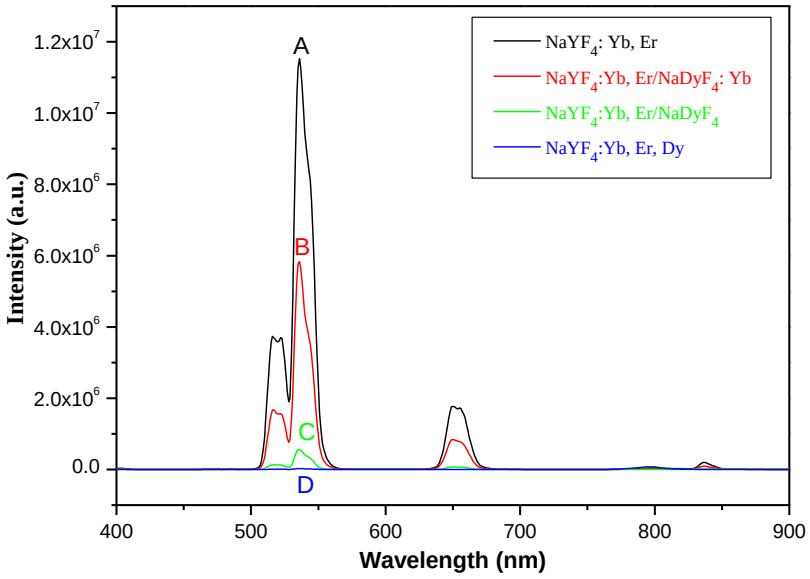

Figure 4.4 UC luminescence spectra of $NaYF_4:Yb^{3+},Er^{3+}$ (A); $NaYF_4:Yb^{3+},Er^{3+}/NaDyF_4:Yb^{3+}$ (B); (Yb absent) $NaYF_4:Yb^{3+},Er^{3+}/NaDyF_4$ (C) and triple dopant $NaYF_4:Yb^{3+},Er^{3+},Dy^{3+}$ NCs following 980 nm excitation.

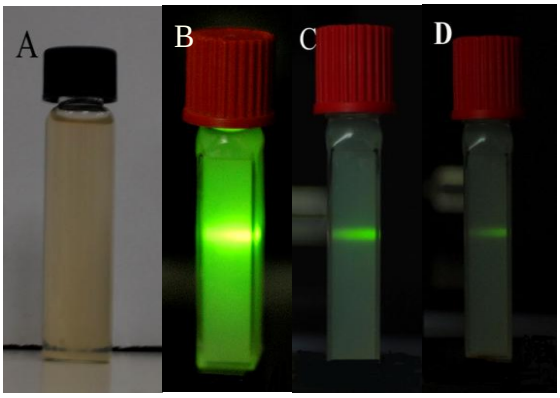

Figure 4.5 Photograph of $NaYF_4:Yb^{3+},Er^{3+}/NaDyF_4:Yb^{3+}$ NCs in hexane solution (A). The UC luminescence photograph of a cuvetter showing green emission of $NaYF_4:Yb^{3+},Er^{3+}/NaDyF_4:Yb^{3+}$ NCs (B); (Yb absent) $NaYF_4:Yb^{3+},Er^{3+}/NaDyF_4$ (C); and triple dopant $NaYF_4:Yb^{3+},Er^{3+},Dy^{3+}$ NCs (D) at 980 nm excitation.

The intensity of the green emission of (a) $NaYF_4:Yb^{3+},Er^{3+}$ NCs is much stronger than that of (B), (C) and (D) NCs, due to the absence of Dy^{3+} ions. Dy^{3+} ions have the reputation of being a poisonous center in Yb-Er and Yb-Tm or Yb-Ho UC emitters. The possible explanation for the detrimental effects of Dy^{3+} to Er^{3+} ions is the depopulation of $^4I_{11/2}$ (Er^{3+}) and $^2F_{5/2}$ (Yb^{3+}) by Dy^{3+} ions. The $^2F_{5/2}$-$^2F_{7/2}$ transition of Yb^{3+} ions and $^4I_{11/2}$-$^4I_{15/2}$ transition of Er^{3+} ions are resonant with the $^6H_{5/2}$-$^6H_{15/2}$ transition of Dy^{3+} ions, hence, energy transfer between Yb^{3+}, Er^{3+} and Dy^{3+} can take place. Dy^{3+} ions populate the $^6H_{5/2}$ excited state from $^6H_{15/2}$ ground state directly excited by a 980 nm photon or receiving energy from the excited Yb^{3+} and Er^{3+} ions. Back-energy transfer to Yb^{3+} ions is negligible due to the short life time of $^6H_{5/2}$.[207-209] The excited Dy^{3+} ions can either relax radiatively to $^6H_{15/2}$, or relax nonradiatively to the $^6H_{9/2}$ level and the transition energy is transferred and excite the Er^{3+} ions from the $^4I_{15/2}$ to $^4I_{13/2}$. The second energy transfer from the Dy^{3+} to Er^{3+} ions takes place via $^4I_{13/2}$-$^4F_{9/2}$, subsequently the third energy transfer caused Er^{3+} ions to the upper excitation level ($^2H_{9/2}$). The radiative transition from $^2H_{9/2}$ to $^4I_{11/2}$ level of Er^{3+} ions gives rise of the red emission around 660 nm (Figure 4.6). This three-photon excitation process has been demonstrated by a study of UC Er^{3+} emissions in the presence of Dy^{3+} ions.[207,208] However, the efficiency of this three-photon excitation efficiency is low compared to the two-photon Yb^{3+}-Er^{3+} energy transition process. Yb^{3+} ions have single excitation level at 980 nm and exhibit a much larger absorption cross-section at this level, acting more efficiently as sensitizing centers in comparison with Dy^{3+} ions.

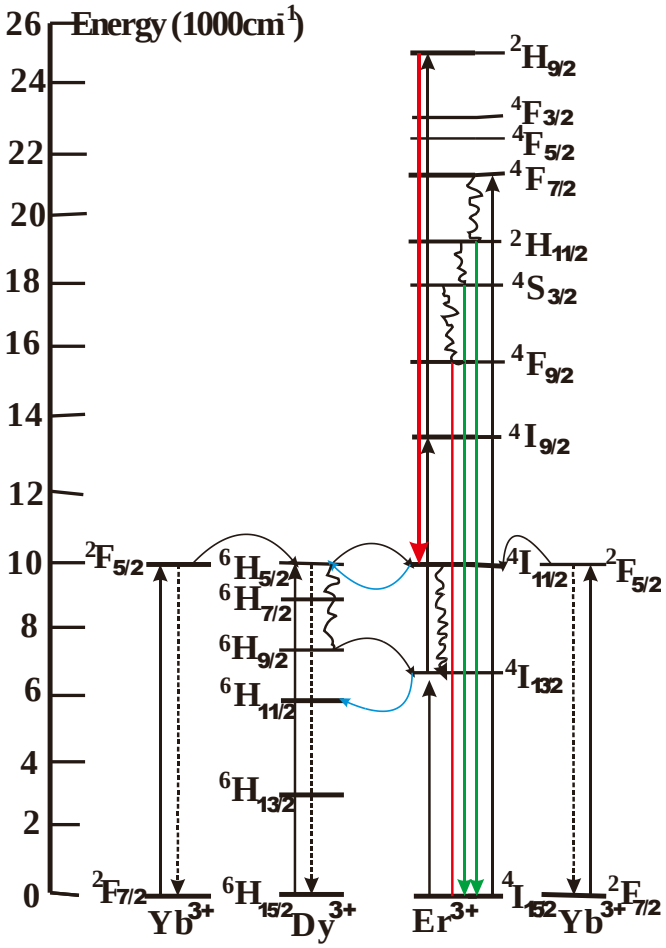

Figure 4.6 Proposed up-conversion mechanism in $NaYF_4:Yb^{3+},Er^{3+}$; $NaYF_4:Yb^{3+},Er^{3+}/NaDyF_4:Yb^{3+}$; $NaYF_4:Yb^{3+},Er^{3+}/NaDyF_4$ and triple dopant $NaYF_4:Yb^{3+},Er^{3+},Dy^{3+}$ NCs following 980 nm excitation. Solid lines indicate energy level, solid arrow indicated excitation, curved arrows indicate energy transfer, and dashed arrows indicate nonradiative decay while colored arrows indicate emission.

The presence of an outer layer or shell structure, be it an active or inert layer, has proven to be an effective way to improve the fluorescence of the NCs.[210,211] This is consistent with our observation that $NaYF_4:Yb^{3+},Er^{3+}/NaDyF_4:Yb^{3+}$ (B) and $NaYF_4:Yb^{3+},Er^{3+}/NaDyF_4$ (C) NCs show stronger emission than triple doped

$NaYF_4:Yb^{3+},Er^{3+},Dy^{3+}$ (D).[210,211] The surface defects around the emitters Er^{3+} ions are one of the reasons that account for the low efficiency of the fluorescence. A large portion of Er^{3+} ions are located on or near surface of the core NCs because of their high surface-to-volume ratio arising from the small particle size. The passivating outer layer reduces the non-radiative decay from the emitter Er^{3+} ions in the core and also protects the ions from the large vibrational energies of the solvent and surface-associated ligands. Furthermore, the emitters Er^{3+} ions are physically separated from the Dy^{3+} ions, reducing the detrimental effect of Dy^{3+} ions.[212,213]

Upon further comparison of $NaYF_4:Yb^{3+},Er^{3+}/NaDyF_4:Yb^{3+}$ (B) and $NaYF_4:Yb^{3+},Er^{3+}/NaDyF_4$ (C) NCs, it was observed that the UC emission intensity was further enhanced upon doping the shell with Yb^{3+} ions (Figure 4.4). Dopant concentration which determines distance between two neighboring ions has a great impact on the energy transfer efficiency and hence the UC efficiency of lanthanide ions doped NCs.[23] Yb ions exhibit a much larger absorption cross-section in NIR region and work more efficiently as a sensitizer compared to other ions. Increasing the sensitizers in the shell reduces the poisonous effect of the Dy^{3+} ions on the Er^{3+} ions by tricking the Dy^{3+} ions to undergo energy transfer with the "sacrificial" Yb^{3+} ions. The increase in Yb^{3+} ions centers also facilitates Er^{3+} ions to the $^4F_{7/2}$ state via two successive energy transfers ($^4I_{15/2}$-$^4I_{11/2}$, $^4I_{11/2}$-$^4I_{7/2}$), of which Er^{3+} ions decay to give rise to green ($^2H_{11/2}$-$^4I_{15/2}$, $^4S_{3/2}$-$^4I_{15/2}$) and red ($^4F_{9/2}$-$^4I_{15/2}$) emissions. Thus, the presence of Yb^{3+} in the outer layer may also facilitate energy transfers to the core Er^{3+}.

To determine the potential application of the $NaYF_4:Yb^{3+},Er^{3+}/NaDyF_4:Yb^{3+}$ NCs in MRI, the transverse relaxation time (T_2)–weighted images were tested using a 7 T MRI scanner. A silanization procedure was used to render the NRs water-soluble.[214] Different concentrations of the NCs were tested. Representative T_2-weighted (TR/ TE= 2000 ms, 25 ms) image is shown in Figure 4.7. It shows signal reduction with increasing Dy^{3+} concentration, a result very similar to that obtained for the superparamagnetic iron oxide NCs in MRI. The relaxivity r_2 of NCs was determined to be 328. 19 $mM^{-1}s^{-1}$ (Figure 4.8), which is higher than that of other reported SPIO T_2 negative contrast agents, such as Feridex (r_2=120 $mM^{-1}S^{-1}$), Resovist (r_2=186 $mM^{-1}S^{-1}$) and Combidex (r_2=65 $mM^{-1}S^{-1}$), and other T_2 contrast agents, such as FeNP (129 $mM^{-1}S^{-1}$) $CoFe_2O_4$ (172 $mM^{-1}S^{-1}$), $MnFe_2O_4$ (208 $mM^{-1}S^{-1}$) and $NiFe_2O_4$ (152 $mM^{-1}S^{-1}$), indicating that the current NRs were more efficient in enhancing T_2 contrast.[215]

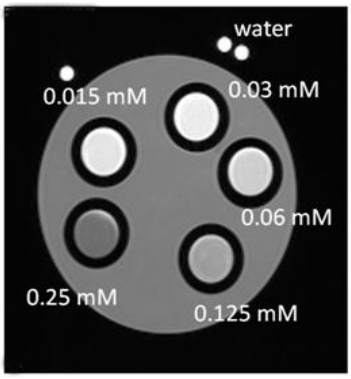

Figure 4.7 T_2-weighted MR images of silanized $NaYF_4:Yb^{3+}$, $Er^{3+}/NaDyF_4:Yb^{3+}$ NCs in 1% agarose gel with increasing concentrations (0.015, 0.03, 0.06, 0.125, 0. 5).

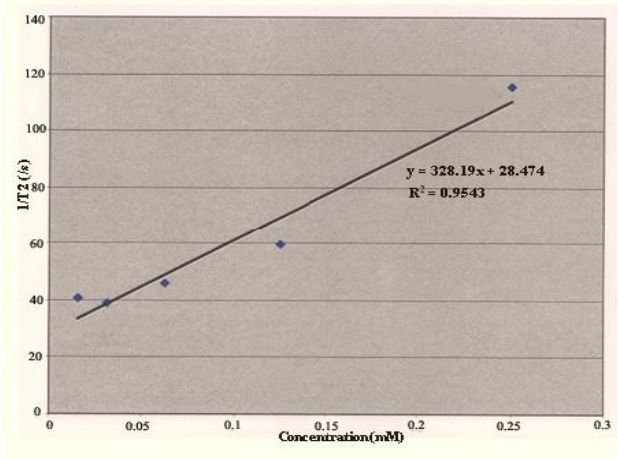

Figure 4.8 The transverse relaxivity (r_2) plot of $NaYF_4:Yb^{3+}$, $Er^{3+}/NaDyF_4:Yb^{3+}$ NCs obtained at various concentrations in 1% agarose gel.

4.3 Conclusions

The current work demonstrates a two-stage synthesis strategy and the enrichment of Yb^{3+} doping in lanthanide nanocrystals $NaYF_4:Yb^{3+}$,$Er^{3+}/NaDyF_4:Yb^{3+}$ result in excellent up-conversion fluorescence, despite the presence of Dy^{3+} ions, and can efficiently induce dark T_2 images in high magnetic field. These nanocrystals have the potential to serve as a versatile contrast agent in a new generation fluorescence and MR integrated imaging modality. This report also reveals that rational design of the composition and structure of nanocrystals is of particular importance for developing new functional nanomaterials with unique properties. By Yb^{3+} enrichment and physically separating the UC poisoning Dy^{3+} from the Er^{3+} emitters, a new type of nanocrystals with T_2 MR enhancement and up-conversion, of which properties are solely derived lanthanide ions, has been realized.

Chapter 5: A Strategy to Achieve Simultaneous Up-conversion Fluorescence and Tunable T_1-T_2 Magnetic Resonance Imaging Contrast in Lanthanide Nanocrystals

5.1 Introduction

Multimodal imaging probes are highly desirable for in vivo diagnosis due to their ability to be detectable in multiple mode techniques, leading to more accurate and reliable data.[216,217] Multimodal probes that possess magnetic resonance (MR) as well as optical imaging capabilities have attracted considerable attention in recent years.[216,218] Magnetic resonance imaging (MRI) offers imaging of opaque tissues in a noninvasive manner with a high spatial resolution.[219,220] However, its limited sensitivity for imaging at the cellular level hampers its applications for molecular imaging. [219,220] Optical imaging, on the other hand, provides high sensitivity for *in vivo* imaging, but suffers from low tissue penetration.[221] The integration of MRI and optical imaging could act synergistically by improving the resolution and sensitivity.[11] In this regard, numerous efforts have been dedicated to the fabrication of bimodal imaging contrast agents, such as Gd-Cy5.5/magnetic nanoparticles (NPs),[222] $NaYF_4$/Si-DTTA-Gd^{3+} NPs,[223] Fe_2O_3/CdSe (ZnS) NPs,[224] and Gd_2O_3/C nanoshells.[225]

In particular, lanthanide nanocrystals (NCs) have been actively pursued as multimodal probes due to their unique luminescent and magnetic properties. Compared to

conventional imaging probes such as organic fluorescent dyes and quantum dots (QDs), lanthanides exhibit multicolor and sharp emission with high quantum yield, long luminescence lifetimes, and low toxicity.[226] These excellent features, coupled with their high resistance to photobleaching, make them highly suitable as alternatives to organic dyes and QDs for various biological applications.[226] In addition, lanthanide NCs have been found to be useful as MRI contrast agents, which enhance the visualization of MRI signals. The use of MR contrast agents, which usually constitutes paramagnetic species, can enhance the contrast between normal and malignant tissues by greatly enhancing the water proton's longitudinal (T_1) or transverse (T_2) relaxation rate, the effect which is widely known as proton relaxation enhancement (PRE).[227] T_1 contrast agents comprised typically of paramagnetic complex containing Gd^{3+} and Mn^{2+} ions, induce bright MR images in T_1 weighted experiments by increasing the spin-lattice relaxation rate of nearby water protons. On the other hand, T_2 contrast agents that commonly consist of superparamgnetic NPs (e.g., iron oxide NPs) cause protons in their vicinity to undergo fast spin-spin relaxation which gives rise to dark MR images in T_2 weighted experiments.[228] A dual-mode imaging strategy, where T_1 and T_2 MR imaging modes can be utilized simultaneously, has the potential to obtain more comprehensive diagnostic information. For such purpose, Gd-labeled magnetite NPs were reported as dual-contrast agents for T_1- and T_2-weighted MR imaging.[229] A "magnetically decoupled" $MnFe_2O_3$-$Gd_2O(CO_3)_2$ core/shell NCs were designed as the dual-contrast agents.[230] Ultrasmall superparamgentic iron oxide (USPIO) NPs, capable of depicting enhanced T_1 at low concentration range and weak T_2 contrast effects, have been developed.[231] FeCo-graphitic system has also exhibited high T_1 and

T_2 contrast effect, however, an understanding of the mechanism by which this system operates is still unclear.[232]

In addition, lanthanides possess the ability of converting near-infrared (NIR) light (usually 980 nm) to higher energies ranging from UV to the NIR, a process known as up-conversion (UC), which is strongly desirable for biological applications as it gives rise to deeper light penetration, reduced autofluorescence and light scattering, and increasing image contrast.[77] An ongoing bottleneck in achieving simultaneous UC fluorescence and T_2 MRI contrast in single lanthanide NCs is due to the presence of Dy^{3+} ions, which are up-converter quenchers. Dysprosium (Dy^{3+}) ions, despite being a "poison" for UC emission, can enhance the transverse relaxation rate of water protons in tissues.[77] They are regarded as promising T_2 contrast agents in MRI, as they can provide better spatial resolution and higher contrast to noise ratio at higher magnetic field (>1.5 T).[228]

Herein, we demonstrate a new strategy of combining both UC fluorescence imaging and tunable T_1-T_2 dual-mode MRI contrast properties within a single NC, of which all functionalities arise solely from lanthanide ions (illustrated in Figure 1A). The $NaDyF_4$:Yb^{3+} seed particles were first prepared, which underwent further growth in a second reaction in the presence of Gd^{3+}, Yb^{3+} and Er^{3+} to form nanorods. To circumvent the "poisoning" or quenching by Dy^{3+} ions, we chose ytterbium (Yb^{3+}) ions as the co-dopant sensitizers. Yb^{3+} ions possess single excited state at 980 nm. More importantly, the absorption cross-section of excited Yb^{3+} ions is significantly

greater than many of the excited states of other lanthanides with similar energy levels, rendering the UC or energy transfer process more efficient.[233,234] Fluoride hosts have been demonstrated to possess strong and efficient up-conversion due to their high chemical stability and low photon energies (~350 cm^{-1}).[235,236] Gadolinium (Gd^{3+}) ions on the outer layer of NCs efficiently induce electron-nuclear dipolar interactions with the surrounding water protons, hence shortening the longitudinal relaxation time (T_1) and generating T_1 MRI contrast. Dy^{3+} ions induce good T_2 negative contrast. The resultant NCs demonstrate simultaneous up-conversion luminescence and tunable T_1/T_2 contrast enhancement in MRI, making them good candidates as dual-functional optical and MR imaging contrast agents.

5.2 Results and Discussion

Figure 5.1 shows the TEM images of the seed $NaDyF_4:Yb^{3+}$ NCs (Figure 5.1 (B)) and $NaDyF_4:Yb^{3+}$/ $NaGdF_4:Yb^{3+},Er^{3+}$ NCs (Figure 5.1 ©) at different magnifications. The image of the seed NCs (Figure 5.1 (B)) displayed signs of anisotropic growth. The nanorods (NRs) in the presence of Gd^{3+} and Er^{3+} showed relatively uniform rod-shape morphology, due to the well defined orientation and growth. The average diameter and length of the $NaDyF_4:Yb^{3+}$ NCs are 17 and 22 nm, respectively. The average diameter and length of the $NaDyF_4:Yb^{3+}$/ $NaGdF_4:Yb^{3+},Er^{3+}$ NRs are 21 and 45 nm, respectively.

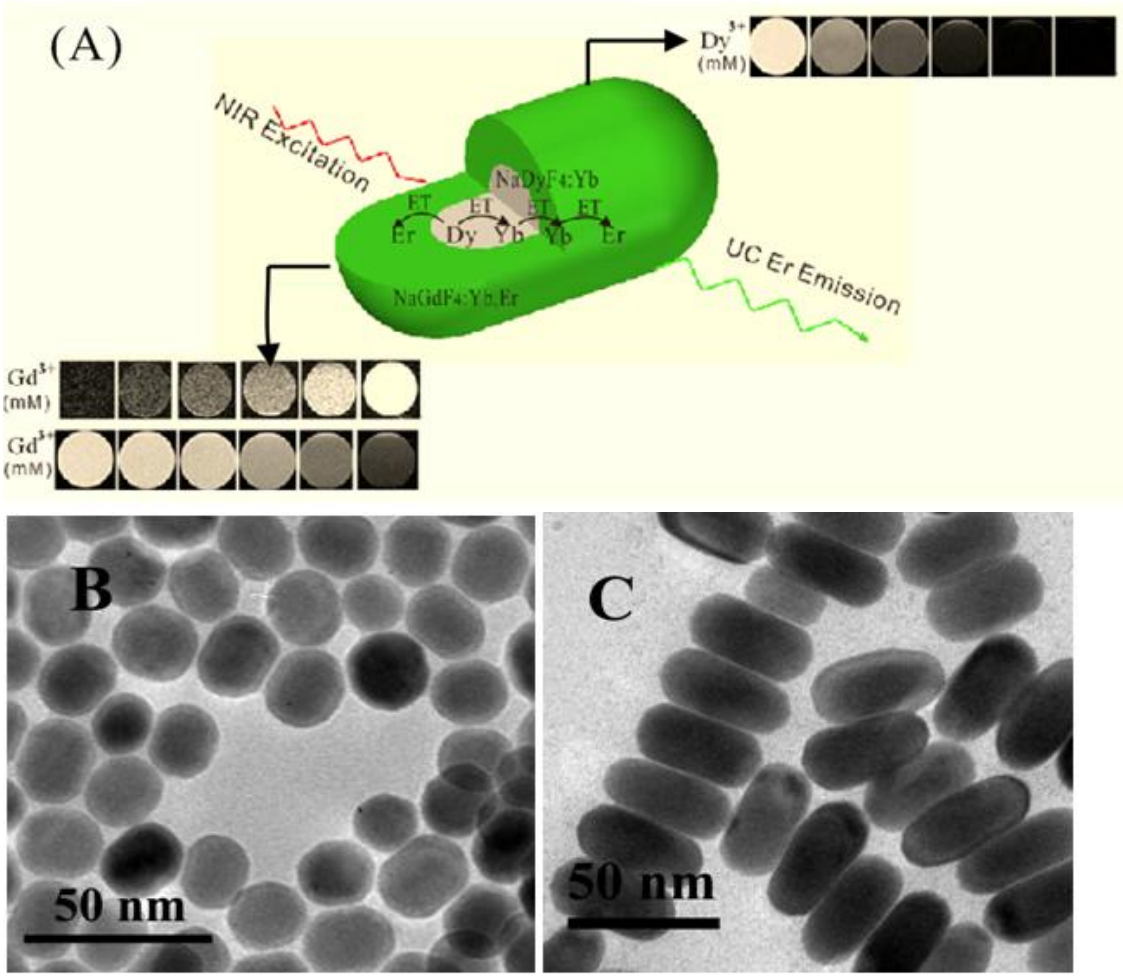

Figure 5.1 (A) Schematic illustration of the general strategy to achieve tunable MRI T_1-T_2 contrast and Up-conversion Lanthanide Nanocrystals; (B) TEM images of $NaDyF_4:Yb^{3+}$ NCs and (C) $NaDyF_4:Yb^{3+}$/ $NaGdF_4:Yb^{3+},Er^{3+}$ NRs.

The hexagonal phase structure of the $NaDyF_4:Yb^{3+}$ NCs and $NaDyF_4:Yb^{3+}$ /$NaGdF_4:Yb^{3+}$, Er^{3+} NRs were confirmed by the XRD analysis (Figure 5.2). The peak positions and intensities of the seed NCs are consistent with hexagonal-phase $NaDyF_4$.[237] The XRD pattern of the $NaDyF_4:Yb^{3+}$/$NaGdF_4:Yb^{3+},Er^{3+}$ NRs is similar to that of the seed NCs, but with an increase in peak signal intensity. The increased

intensity is attributed to the increase in size of the NCs and similar crystal structure of $NaDyF_4$ and $NaGdF_4$.

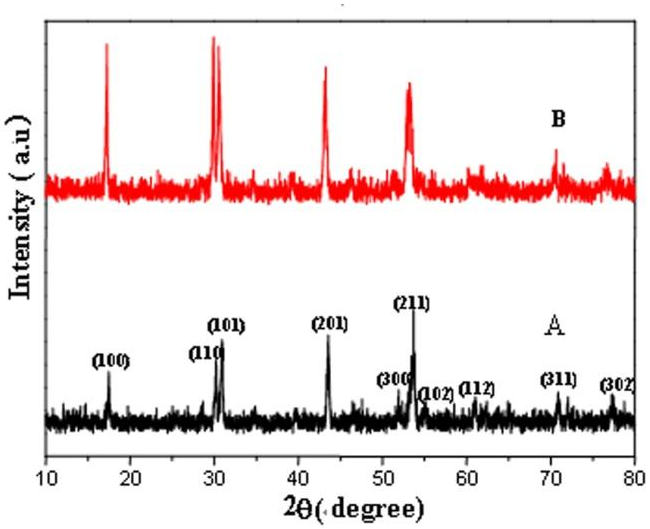

Figure 5.2 XRD patterns of as-synthesized $NaDyF_4:Yb^{3+}$ NCs (A) and $NaDyF_4:Yb^{3+}$/ $NaGdF_4:Yb^{3+},Er^{3+}$ NRs (B).

Energy-dispersive X-ray analysis (EDX) confirmed the presence of all elements in the seed NCs (Na, Dy, F, Yb) and NRs (Gd, Er in addition to all seed elements) (Figure 5.3). Using inductively coupled plasma mass spectroscopy (ICP-MS), the Gd:Dy molar ratio was quantified to be 40.2:40, based on the stoichiometric ratio of the chloride precursors used in the experiment.

To demonstrate the feasibility of our strategy, four types of NCs were synthesized. Figure 5.4 (1) shows the UC emission spectra of (A) $NaGdF_4:Yb^{3+},Er^{3+}$; (B) $NaDyF_4:Yb^{3+}/NaGdF_4:Yb^{3+}$, Er^{3+}; (C) Yb^{3+}-absent $NaDyF_4/NaGdF_4:Yb^{3+},Er^{3+}$ NCs and (D) triple-doped $NaGdF_4:Yb^{3+},Er^{3+},Dy^{3+}$ NCs, excited at 980 nm. All the NCs

exhibited green and red emissions. There are no characteristic emission lines of Dy^{3+} ions in the wavelength regions of 470-500 nm and 570-600 nm, indicating that Yb^{3+} ions act as the main sensitizer and Er^{3+} ions the emitters. Therefore, green emissions at 523 and 546 nm are ascribed to Er^{3+} ions transition from $^2H_{11/2}$ and $^4S_{3/2}$ excited states

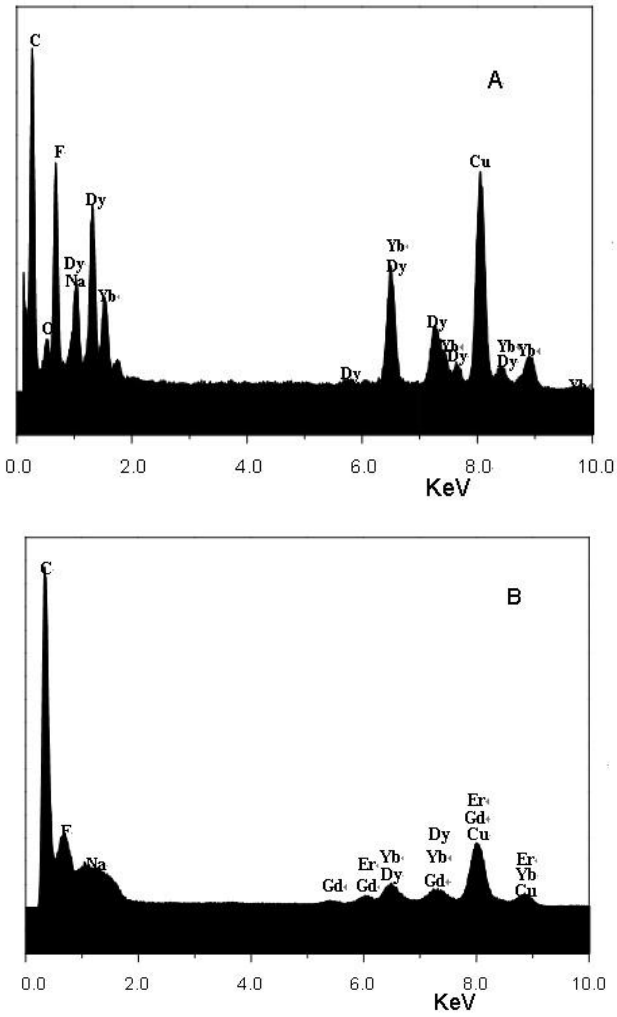

Figure 5.3 Energy-dispersive X-ray spectroscopy (EDX) analysis of (A) $NaDyF_4:Yb^{3+}$ and (B) $NaDyF_4:Yb^{3+}/NaGdF_4:Yb^{3+},Er^{3+}$ NCs, revealing the presence of the Gd, Er after secondary growth on the $NaDyF_4:Yb^{3+}$ seeds NCs.

to the $^4I_{15/2}$ ground state respectively, while red emission at 659 nm is due to the transition from $^4F_{9/2}$ excited state to the ground state of Er^{3+} ions.[238,239] The intensities of green emission of all NCs are much stronger in comparison with those of red emissions, as shown in Figure 5.4 (2).

The intensities of the green emissions of NCs (B), (C) and (D) are weaker than that of (A) $NaGdF_4:Yb^{3+},Er^{3+}$ NCs, due to the detrimental effect of Dy^{3+} ions (Figure 5.4 (1)). Dy^{3+} ions are well-known UC quenchers. The detailed mechanism of Dy^{3+} ions quenching of Er^{3+} luminescence has already been discussed in chapter 4, p95-96.

To examine the feasibility of using the $NaDyF_4:Yb^{3+}/NaGdF_4:Yb^{3+},Er^{3+}$ NCs as tunable T_1-T_2 dual MRI contrast agents, T_1- and T_2-weighted MR images (Figure 5.6) as a function of NC concentration and relaxivities, r_1 and r_2, were measured using a 7 T MRI system. The NCs were rendered water-dispersible using an amphiphilic layer of cetyl trimethylammonium bromide (CTAB).[242] The NCs show excellent negative T_2 enhancement due to the presence of Dy^{3+} ions (Figure 5.5). Interestingly, tunable positive and negative T_1 enhancement can be achieved by suitably employing a magnetization preparation module in a gradient echo (GE) or a spin echo (SE) sequence. In Figure 5.5 (A), the images were acquired with a GE T_1-weighted sequence with a magnetization preparation (inversion pulse) module which exhibits a genuine T_1 contrast (positive enhancement). However, Figure 5.5 (B) shows T_1 weighted images acquired with a SE sequence without any preparation module, which clearly shows negative enhancement albeit the parameters were optimized to generate

T_1 contrast. r_2 is determined to be 437.96 $mM^{-1}S^{-1}$, while r_1 is 0.321 $mM^{-1}S^{-1}$ as shown in Figure 5.6.

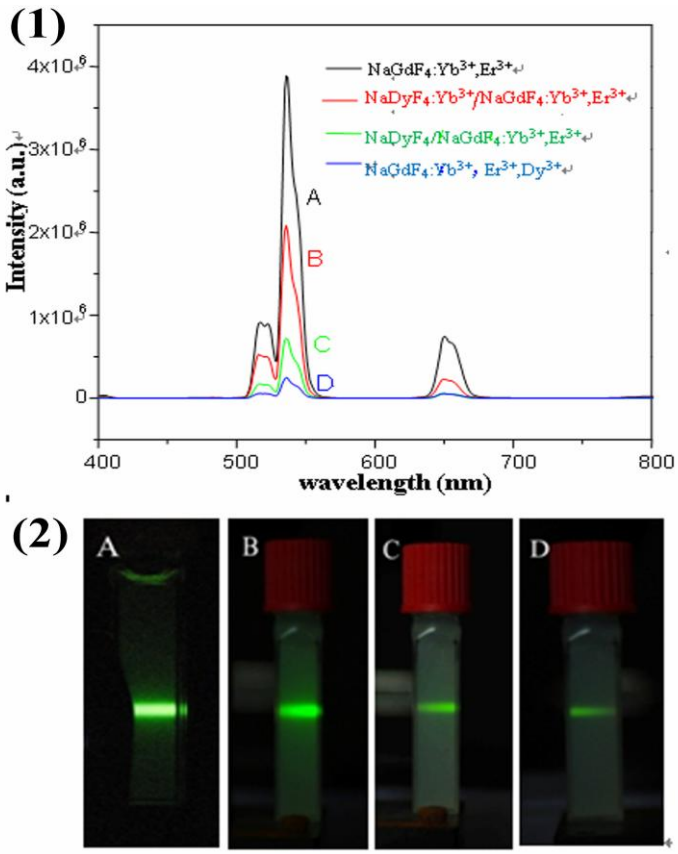

Figure 5.4 (1) UC fluorescence spectra of the (A) $NaGdF_4:Yb^{3+},Er^{3+}$, (B) $NaDyF_4:Yb^{3+}$/ $NaGdF_4:Yb^{3+},Er^{3+}$; (C) Yb^{3+}-absent $NaDyF_4/NaGdF_4:Yb^{3+},Er^{3+}$ and (D) triple dopant $NaGdF_4:Yb^{3+},Er^{3+},Dy^{3+}$ NCs at the excitation of 980 nm. (1wt %); (2) Photographs of green emissions of the water-soluble (A) $NaGdF_4:Yb^{3+},Er^{3+}$; (B) $NaDyF_4:Yb^{3+}$/ $NaGdF_4:Yb^{3+},Er^{3+}$; (C) Yb^{3+}-absent $NaDyF_4/NaGdF_4:Yb^{3+},Er^{3+}$ and (D) triple doped $NaGdF_4:Yb^{3+},Er^{3+},Dy^{3+}$ NCs. (1 wt%)

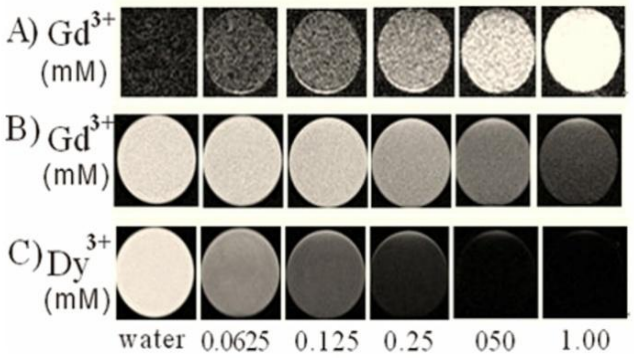

Figure 5.5 (A) Bright T_1–weighted MR images using gradient echo sequence, (B) dark T_1–weighted images using spin echo sequence and (C) T_2–weighted images of $NaDyF_4:Yb^{3+}$/ $NaGdF_4:Yb^{3+},Er^{3+}$ NCs at different concentrations (0, 0.0625, 0.125, 0.50, 1.00 mM).

The SE based T_2 weighted experiments generate negative T_2 contrast due to the presence of Dy^{3+} ions. Dy^{3+} ions, having shorter electronic relaxation time (~ 0.5 ps) and higher magnetic moment (10.6 μ_B), have proved to efficiently induce T_2 contrast.[243] For example, Elst et al. examined Dy-DTPA derivatives as contrast agents in fields between 0.47 and 18.8 T.[244] NPs, such as Dy_2O_3, have also been investigated as T_2 contrast agents in high-field MRI (from 7 to 17.6 T).[245,246] Recently, we have reported ultrasmall Dy_2O_3 NCs as a positive T_2 contrast agent (r_2 of 2.12 $mM^{-1}s^{-1}$).[246] The relaxivity of Dy^{3+} ions primarily originates from its magnetization and Curie Spin (CS) relaxation mechanism which becomes very dominant at high magnetic field.[243,247] According to the CS relaxation mechanism, the induced Curie magnetic moment per Dy^{3+} ion is given by: $\mu_C = \mu_S^2 B_0/3kT$; where μ_S is the magnetic moment, k is Boltzmann's constant and T is the absolute temperature. This implies that induced

magnetization of the Dy^{3+} ions increases with external magnetic field and is proportional to square of the magnetic moment of Dy^{3+} ions. The relaxivity, r_2 measured at 7 T MRI (437.96 $mM^{-1}s^{-1)}$ is resultant of a combined effect of the NPs magnetic moments and Curie Spin relaxation arises from Dy^{3+} ions.

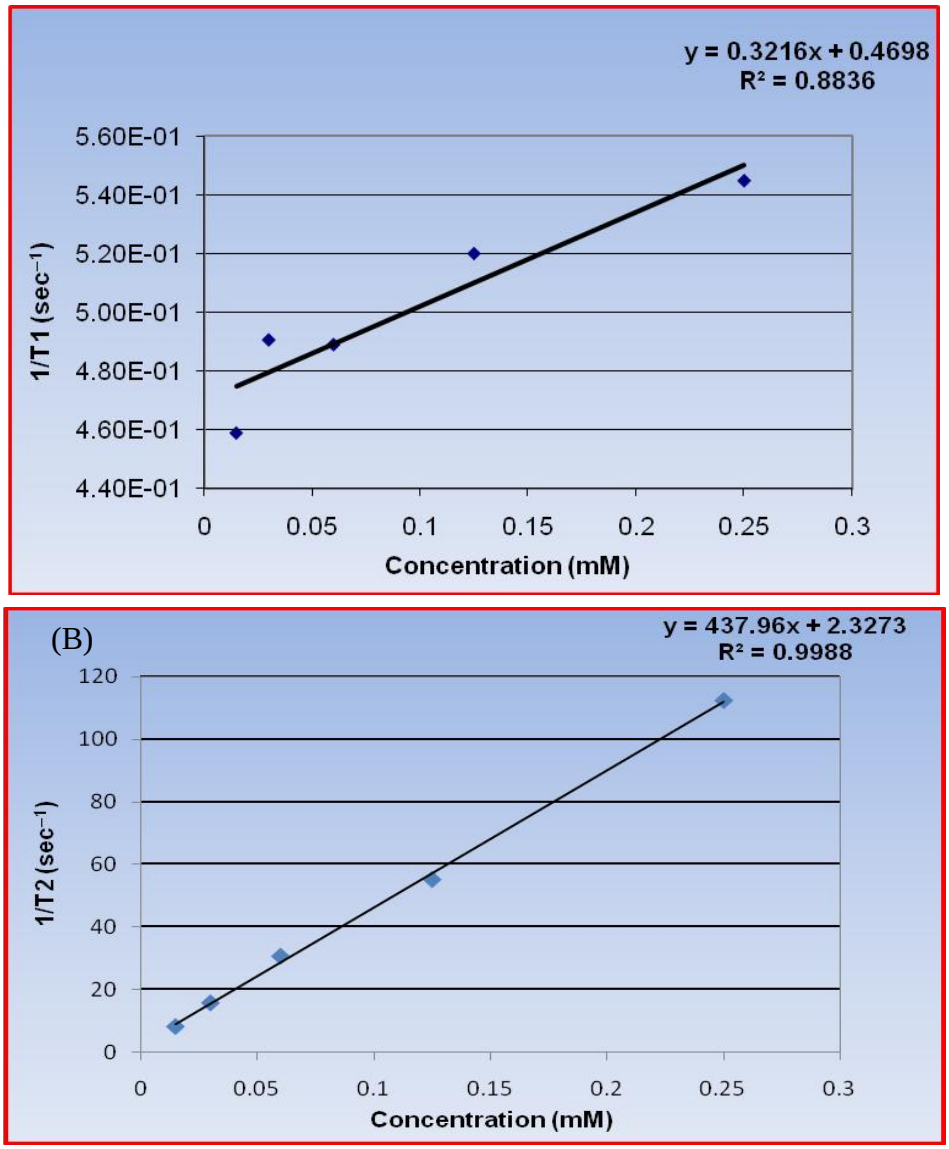

Figure 5.6 (A) T_1 and (B) T_2 relaxivity plot of $NaDyF_4:Yb^{3+}/NaGdF_4:Yb^{3+},Er^{3+}$ NCs. Spin echo sequence were used to measure the T_1 and T_2 relaxation time constant. The experimental parameters for T_1 and T_2 weighted images are TR/TE/NEX = 400/8.9/16 and TR/TE/NEX =1500/41/16, respectively.

Gd^{3+} ions, which have seven unpaired electrons, are known to have excellent T_1 enhancing properties due to their long electronic relaxation time.[228,248,249] In order to execute efficient exchange of magnetic fields with surrounding water protons to induce T_1 contrast, contrast agents are required to be in close contact with water molecules.[221,248-250] In the present study, Gd^{3+} ions are doped in the outer layer of the NCs, which remain in close contact with the surrounding water protons, and therefore capable of inducing T_1 relaxation. Interestingly, the current NCs generate T_1 negative contrast, which has never been reported to the best of our knowledge, in the normal SE based T_1-weighted experiments (in the absence of an inversion module). Contrast agents, including Ln^{3+} ions, show both T_1 and T_2 relaxation properties at different extent. The T_1 contrast agents viz., Gd (III), demonstrate both T_1 and T_2 relaxation properties, but shortening of T_1 is dominated over that of T_2. This results in a hyperintense image within areas where the agents are taken up.[228] Thus, species with high T_1 values lend themselves to hypointense images.[228] The r_1 of NCs obtained from SE, is much smaller than that of other T_1 contrast agent, for example Gadovist (commercially Gd-based contrast agents, r_1 = 4.34 $mM^{-1}S^{-1}$),[228] Gd_2O_3 NPs (8.8 $mM^{-1}S^{-1}$ for size 2.2 nm and 4.4 $mM^{-1}S^{-1}$ for size 4.6 nm),[251] ultrasmall Gd_2O_3 NRs (1.5 $mM^{-1}S^{-1}$),[252] and GdF_3 (3.17 $mM^{-1}S^{-1}$),[253] indicating the T_1 relaxation of water is large in these NCs and hence capable of inducing negative contrast. The presence of Dy^{3+} is inferred to affect the T_1 relaxivity induced by the Gd^{3+} ions (due to the very short electronic relaxation time of Dy^{3+} compared to Gd^{3+} ions), hence leading to the current observation of negative T_1 contrast. Cheon and coworkers reported similar findings, that the coupling process between the electron spins of the T_1 contrast agent

and nuclear spins of water is perturbed in the presence of additional magnetic field generated by T_2 contrast agent in close proximity.[230] One of the strategies to increase the relaxivity is to enhance the exchange rate of water between the NPs and the water in the bulk phase.[230] The water exchange rate of Dy^{3+} ions is generally faster than that of the Gd^{3+} ions. Therefore, the measured low r_1 could be attributed to the slow water exchange rate of Gd^{3+} which is present in the outer layer of our NCs. In addition, the relaxivity measurements at high field (7 T) and the relatively larger size of NCs are another two reasons that may account for the lower r_1 of the current NCs. Gd^{3+} is known to exhibit decreased relaxivity as magnetic field strength increases, which is consistent with our observation.[250,254] Previous studies showed that smaller-size NCs, which have a higher surface area, showed a higher MR relaxivity due to easier magnetic exchange with surrounding water protons.[255] The rod-shaped NCs have relatively smaller surface area, thereby, a fairly large portion of the Gd^{3+} ions are embedded inside the NCs which are less likely to contribute to the relaxation of water protons. Thus, the ionic relaxivity goes down due to a relatively thick shell around the $NaDyF_4$ NCs.

Despite a weak T_1 negative contrast, a stronger T_1 positive contrast was also obtained in a GE sequence when an inversion module was used at the start of the pulse sequence. The GE is generated by fast gradient reversal which allows minimum echo time and repetition time, and is characterized by rapid sampling time. Since the signal is detected rapidly during the recovery of the longitudinal magnetization, this sequence generates a good T_1 positive contrast.

The current NCs have the advantage of showing tunable properties of positive T_1 and negative T_1 by applying appropriate pulse sequences, as well as negative T_2 MRI contrast. In addition to possessing the advantages of normal positive T_1 contrast agents for clear visualization of anatomic details and bright contrast for distinguishing from other pathogenic or biological condition, the current NCs also possess the advantages of negative T_1 contrast agents. One of the disadvantages of using positive T_1 contrast agent is the bright signal they generate which causes artifacts in the bowel lumen.[256] This may be avoided if the signal can be tuned to a dark contrast. Generally the T_2 weighted experiment consumes more experimental time, because of large TR and TE, than the T_1 weighted experiments. Since our NCs generate negative T_1 enhancement (small TR and TE), they could find application in cases where negative contrast is desired within a limited experimental time. Therefore, depending on the tissue site of interest, the current NCs can be selectively tuned to visualize by bright or dark T_1 and T_2-weighted MRI contrast in order to achieve complementary information that cannot be obtained by using single mode contrast agents. In addition, the image quality can also be improved, leading to more accurate diagnosis. The relaxivities of the current NCs may be optimized by varying the concentration of the dopants and/or introducing a physical barrier between the Dy^{3+} and Gd^{3+} ions, so as to reduce the effect of Dy^{3+} on Gd^{3+}.

5.3 Conclusions

In conclusion, we have realized a simple strategy to fabricate lanthanide NCs possessing tunable T_1 and T_2 MR contrasts and efficient up-conversion fluorescence,

which is solely based on active lanthanide elements. The key strategy involves physically separating the T_2 and "poisoning" Dy^{3+} ions from the Er^{3+} emitters, and by co-doping Dy^{3+} with Yb^{3+}. In addition to the ability to show strong T_2 contrast, by utilizing a different pulse sequence, positive or negative T_1 contrast can be tuned. These NCs should attract strong interest as a new generation multifunctional "smart" contrast agent in the area of up-conversion fluorescence/MR multimodal imaging.

Chapter 6: Color-Tunable Up-conversion Emission from Yb,Tm Codoped $NaYF_4$/CdSe Core/shell Nanocrystals

6.1. Introduction

Multicolor emissions of nanocrystals (NCs) have found applications in light emitting displays, lasers, optoelectronic devices and biological imaging.[125,241,257] Different approaches have been explored to achieve multicolor emission by either controlling emission wavelength or varying material compositions and/or dopant concentration in the NCs.[14,258,259] However, most of these approaches have limitations, such as strong background autofluorescence, low detection sensitivity, low light-penetration depth in tissue and high photodamage to the living organisms. These drawbacks arise mainly from the excitation in the ultraviolet (UV) region. As a consequence, there are a great interests in the design of near-infrared (NIR)-to-visible fluorescent NCs.

NIR-to-visible fluorescence imaging provides distinctive properties: low absorption, weak background autofluoresence, high spatial resolution, high sensitivity and minimum photodamage to living cells and tissues. Various NIR nanoprobes have been developed, such as gold,[260-262] carbon nanotubes (CNT),[263,264] NIR dye-containing NCs,[265-267] QDs,[268-278] and lanthanide-based NCs. NIR dye-containing NCs offer advantages of high payload of dyes, high sensitivity and photostability resulting from the protection of the dyes from the outside environment.[265] However, the quantum yield of the NPs is low and their broad emission peaks, rapid photodegradation and

narrow excitation profile limit their further applications. NIR fluorescent QDs that exhibit narrow, size-tunable emission with broad excitation spectra, high fluorescence quantum yield, large effective Stokes shifts and high resistance to photobleaching have been under investigation. However, most of these QDs are down-conversion (DC) probes. The DC QDs emit low energy photons when excited by a high energy radiation, typically within the UV or visible wavelengths. Conversely, up-conversion (UC) fluorescence is a process that converts low energy light in the NIR region into higher energy visible light through multiple photon absorption or energy transfer.[279] It is promising in biomedical imaging and detection, compared to the DC process. Distinct advantages of UC fluorescence include minimum photodamage to living cells and tissues, weak background autofluorescence, high spatial resolution and detection sensitivity and high tissue penetration.[279,280] These benefits motivate researchers to investigate NIR excitable QDs for UC fluorescence. Examples include CdSe,[269,281,282] CdSe/ZnS,[274] CdS,[276] CdTe,[277,282] ZnCdS,[276] CdSe/AsS,[283] CdSe/ZnSe,[284] InP,[285] ZnS/Mn^{2+},[286] GaAs-$GaInP_2$.[287,288] Unfortunately, their quantum efficiency is quite low, and an expensive shortpulsed laser [e.g. femtosecond laser, Ti: sapphire pulsed laser] with a high power density is required to compensate for their low quantum efficiency.[276,277,282] Moreover, the mechanisms for UC emission in QDs are still under debate. Two-photon absorption,[281,282,286,288] Auger recombination[287] and thermally assisted surface state processes [283,285] have been proposed to explain the UC emission.

Lanthanide based NPs have attracted numerous research interests due to the following unique optical features: i) efficient absorption NIR light and conversion to visible light based on photon UC.[289] The photon UC is a process based on sequential absorption of

photons and as such its efficiency is much higher compared to two-photon absorption; ii) the NCs exhibit sharp emission lines, long lifetimes, non-blinking and non-photobleaching, and they can also be surface-functionalized with biocompatible polymers and antibodies to decrease toxicity, prolong circulation times and increase tissue selectivity; iii) the quantum efficiency is seven orders of magnitude higher than the most efficient two-photon CdSe/ZnS QDs.[289,290] Among various lanthanide hosts, lanthanide fluorides are excellent hosts due to their high chemical stability as well as low photon energies (~ 350cm^{-1})[290] and they suppress nonradiative multiphonon relaxation process. Up to now, hexagonal phase $NaYF_4$: Yb^{3+},Er^{3+} or $NaYF_4$: Yb^{3+},Tm^{3+} NPs are known as one the most effective NIR-to-vis UCNPs. Multicolor UC emissions of lanthanide based NCs are primarily based on the types of dopants, their relative concentration and/or the host materials.[291-293] Although multicolor imaging can be achieved by using CdSe/ZnS QDs, dye-coated UCNPs[290] or lanthanide NPs with different dopant and concentration,[291-293] the use of QDs-coated UCNPs for achieving multicolor imaging has rarely been reported. Recently, single emission $NaYF_4$: Yb^{3+}, Er^{3+}/CdSe nanoheterostructures were prepared to study the photoconductivity and luminescence resonant energy transfer properties.[278,294] Tunable emission of such nanostructures has not been reported, probably due to the difficulty in achieving strong near-UV or blue wavelengths from the up-converting lanthanide NPs, which provide the excitation source for the QDs. In this work, we report a strategy to achieve color tunable emission lanthanide NPs coated with QDs. The $NaYF_4$: Yb^{3+},Tm^{3+} NPs were coated with green, yellow or red-emitting CdSe QDs. The emission of $NaYF_4$: Yb^{3+},Tm^{3+} NPs were tuned to obtain the optimal UV and blue

emissions which were used to excite the QDs to re-emit at various visible wavelengths. As a result, multicolor emissions with different sized QDs are achieved by using a single 980 nm excitation source. The current system of lanthanide/QDs (LnQD) core/shell NPs which utilizes $NaYF_4$: Yb^{3+},Tm^{3+} NPs as energy donors and CdSe as energy acceptors, offers numerous benefits similar to that of a fluorescent resonant energy transfer (FRET) mechanism, such as high photochemical stability, high signal-to-noise detection and multiplexing capabilities that meet for simple homogeneous in situ bio-detection schemes.[294]

6.2 Results and Discussion

ß-$NaYF_4$: Yb^{3+},Tm^{3+} core NPs were synthesized first which served as the seeds for the CdSe shell growth, resulting in the formation of ß-$NaYF_4$: Yb^{3+},Tm^{3+}/CdSe core/shell LnQD NPs. Different growth time of QDs on the core resulted in different sizes and hence different color QDs. Figure 6.1(e-f) shows transmission electron microscopy (TEM) images of the resulting NCs before and after QD shell growth. From the TEM images, it can be seen that the ß-$NaYF_4$: Yb^{3+},Tm^{3+} NPs are relatively monodisperse and uniform in size with an average diameter of 41 nm (Figure 6.1e). The core/shell LnQD NPs are also relatively monodisperse with a larger diameter of 65 nm (Figure 6.1f), suggesting that the CdSe multilayer shell has successfully grown onto the surface of ß-$NaYF_4$: Yb^{3+},Tm^{3+} core NPs. High-resolution TEM reveals an lattice spacing of 0.52 nm for the core NPs, in good agreement with the *d* spacing of the (100) lattice planes of hexagonal-phase $NaYF_4$ (Figure 6.1e, HRTEM image). For the shell, the lattice spacing of 0.35 nm agrees with *d* spacing of the (001) lattice place of CdSe.

Compositional analyses by energy-dispersive X-ray spectroscopy (EDS) reveal the presence of the doped elements of Yb, Tm in the core NCs and additional elements Cd, Se for the core/ shell NPs, as shown in Figure 6.2. The highly crystalline core and core/shell LnQD NPs can be further confirmed by X-ray power diffraction (XRD) analysis, as shown in Figure 6.3. All the diffraction peaks of the core NCs agree well with the standard pattern of hexagonal phase $NaYF_4$ crystals (JCPDS standard card 28-1192) (Figure 6.3, bottom). Additional five peaks can be assigned to CdSe QDs (Figure 6.3, upper), indicating the formation of the CdSe QD shell.

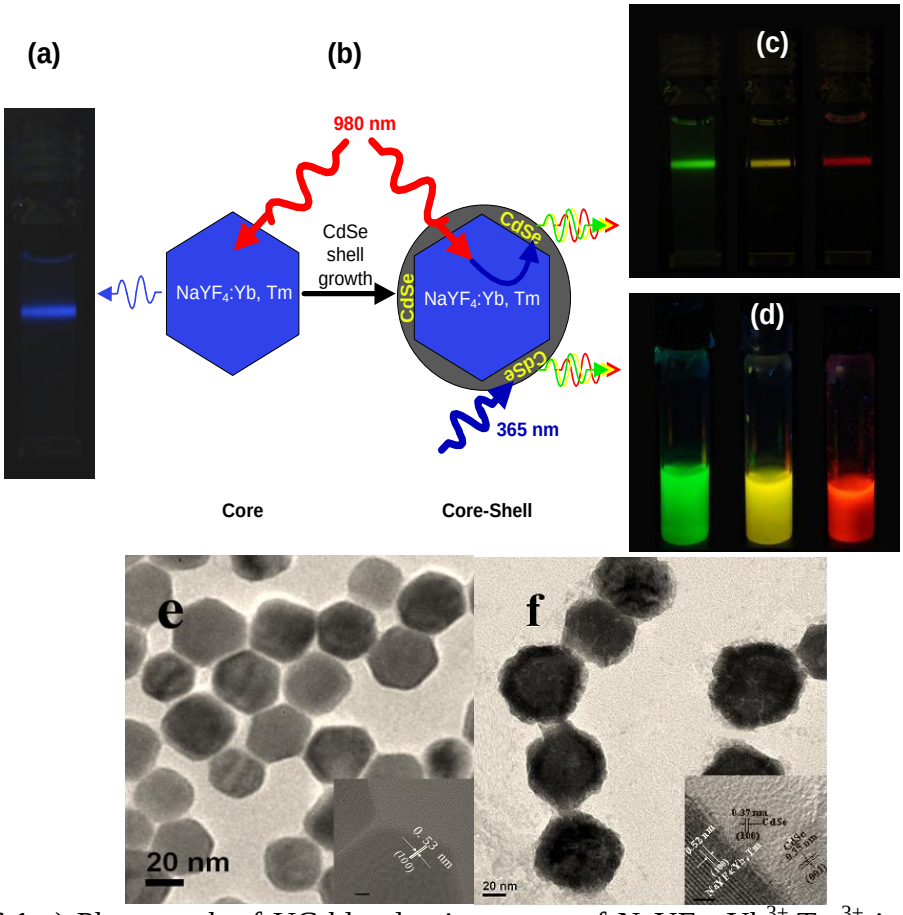

Figure 6.1 a) Photograph of UC blue luminescence of $NaYF_4$: Yb^{3+},Tm^{3+} in hexane solution; b) Schematic illustration of the strategy to achieve multicolor tunable UC emission; c) Photographs of the multicolor emissions of core/shell $NaYF_4$:

Yb^{3+},Tm^{3+}/CdSe NPs excited at 980 nm; d) Photographs of the multicolor emissions of core/shell $NaYF_4$: Yb^{3+},Tm^{3+}/CdSe excited at 365 nm; e) TEM image and HRTEM (insert) of monodisperse $NaYF_4$: Yb^{3+},Tm^{3+} core NPs and (f) TEM image and HRTEM (insert) of monodisperse $NaYF_4$: Yb^{3+},Tm^{3+}/CdSe core/shell NPs. Scale bar represents 5 nm and 2 nm in (e) and (f), respectively.

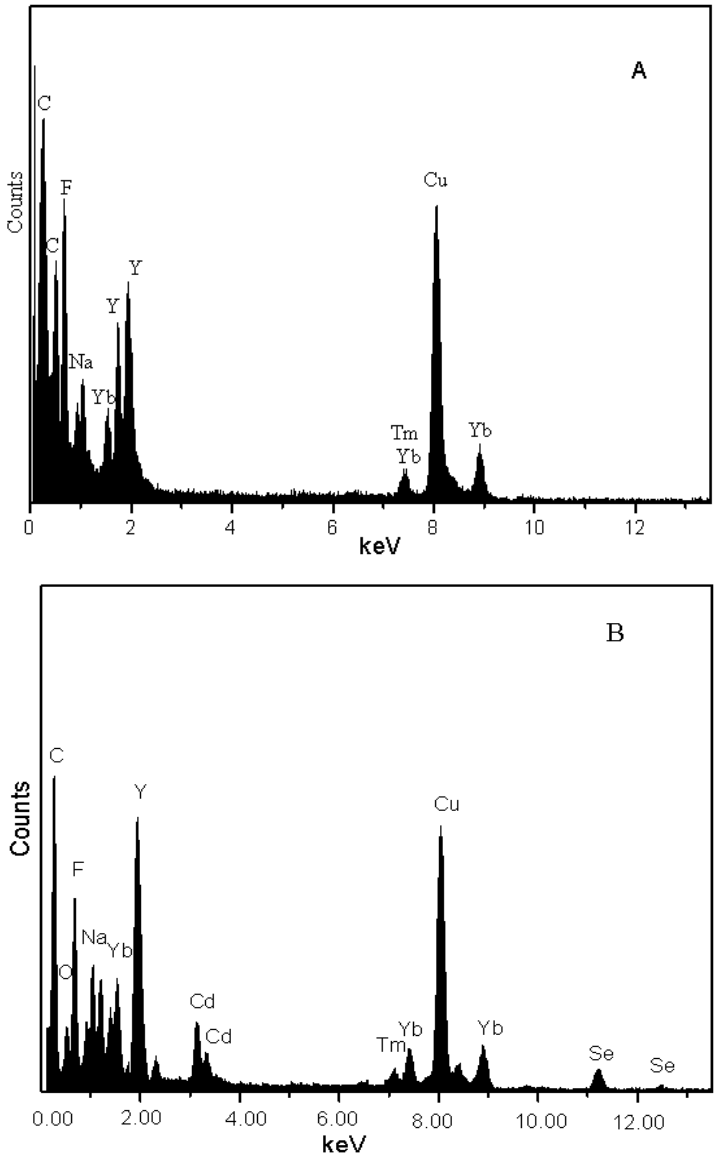

Figure 6.2 The energy-dispersive X-ray spectroscopy analyze of (A) $NaYF_4$: Yb^{3+},Tm^{3+} core and (B) $NaYF_4$:Yb^{3+},Tm^{3+}-CdSe core/shell NPs, revealing the presence of the Cd, Se after coated a shell on the core NPs.

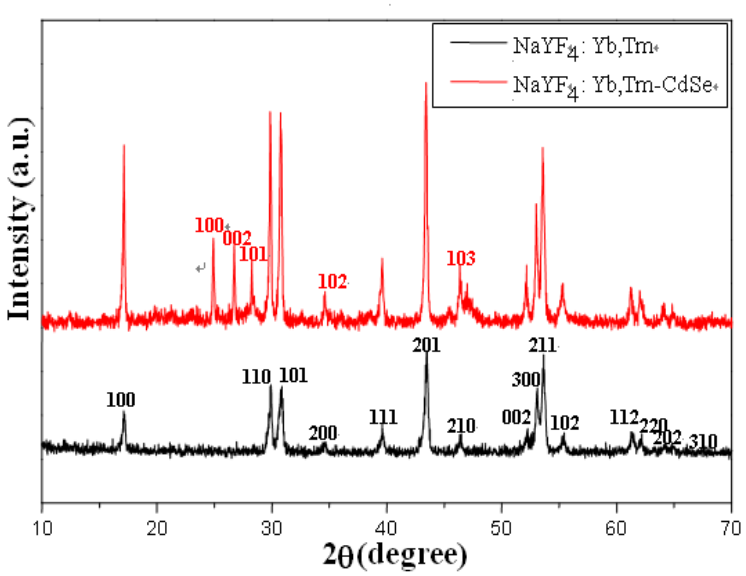

Figure 6.3 XRD patterns of $NaYF_4$: Yb^{3+},Tm^{3+} core and $NaYF_4$: Yb^{3+},Tm^{3+}/CdSe core/shell NPs.

The $NaYF_4$:Yb^{3+}, Tm^{3+} core NPs exhibit five emissions at 355, 450, 485, 690 and 800 nm, corresponding to $^1D_2 \rightarrow {}^3H_6$, $^1D_2 \rightarrow {}^3H_4$, $^1G_4 \rightarrow {}^3H_6$, $^3F_3 \rightarrow {}^3H_6$ and $^3H_4 \rightarrow {}^3H_6$ transitions respectively, which are the characteristic peaks of Tm^{3+} ions (Figure 6.3). The dominant visible blue emission from the core NPs (Figure 6.1a) was observed at 450 nm emission. In order to optimize the near-UV and blue UC emission peaks, which will provide the excitation source for CdSe QDs, we have investigated the effect of Tm and Yb dopant concentrations on the PL intensity (Figure 6.4, 6.5). The core $NaYF_4$: Yb^{3+}, Tm^{3+} (20/0.2%) NPs were found to exhibit strong emission maximum at around 375 nm ($^1D_2 \rightarrow {}^3H_6$) and 450 nm ($^1D_2 \rightarrow {}^3H_4$) upon excitation at 980 nm. By increasing the Tm^{3+} concentration from 0.2% - 5%, the intensities of 375 and 450 nm emissions decrease significantly while 800 nm NIR emission was considerably increased (Figure 6.4). The phenomenon is primarily attributed to the enhanced population of $^3H_4$ level generated by the energy resonance between

$^1G_4 \rightarrow {}^3H_4$ and $^3F_4 \rightarrow {}^3F_2$. Cross relaxation becomes significant as the Tm-Tm distance decreases because of the increasing Tm content in the host lattices.[295] With the molar ratio of Tm^{3+} ions fixed at 0.2%, the UV and blue emissions decrease with increasing concentration of Yb^{3+} (20%-40%). This is attributed to the decrease in interatomic distances between Yb-Tm, which facilitates back-energy transfer from Tm^{3+} to Yb^{3+} and subsequently suppresses the population in excited levels of $^2H_{9/2}$, $^2H_{11/2}$ and $^4S_{3/2}$.[293] Thus, the optimal dopant concentration of 20% Yb^{3+}, 0.2% Tm^{3+} was chosen for subsequent studies.

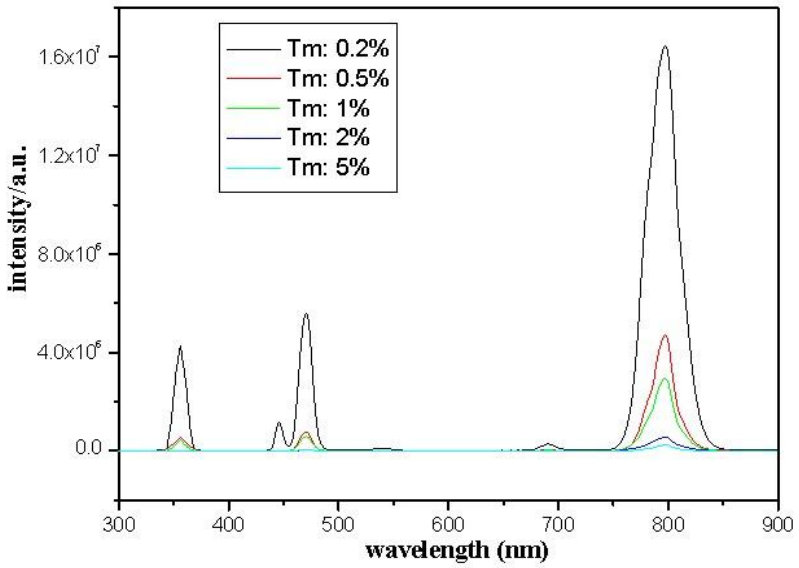

Figure 6.4 Room temperature UC spectra of $NaYF_4$: 20% Yb^{3+}, 0.2–5 mol% Tm^{3+} NPs in cyclohexane solution (1 wt %) under 980 nm excitation.

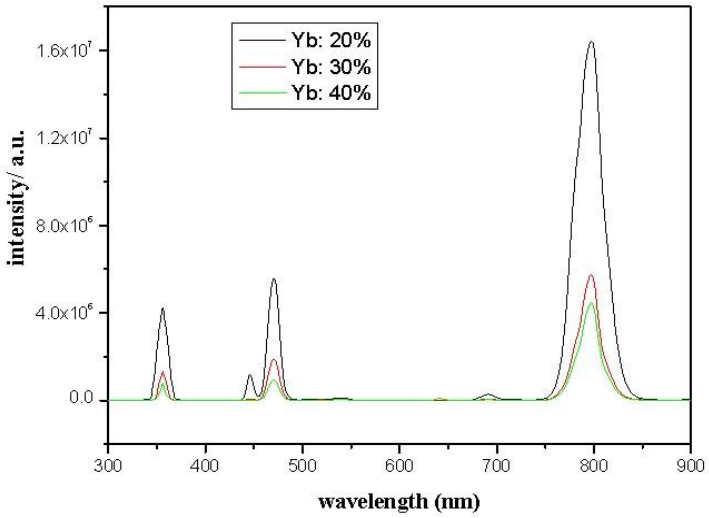

Figure 6.5 Room temperature UC spectra of $NaYF_4$: 20-40%Yb^{3+}, 0.2% Tm^{3+} NPs dispersion in cyclohexane solution (1 wt %) under 980 nm excitation.

Figure 6.6 shows the UC emission spectra of the LnQD NPs. Upon 980 nm excitation, near UV (375 nm) and blue (455 nm) emissions were attenuated compared to core NCs, while emissions at three different wavelengths (533, 560 and 604 nm) were observed, indicating that energy has been absorbed to the CdSe shell. The color of LnQD NPs depends on the CdSe crystal size in the shell. The emission of core/shell LnQD NPs excited under 980 nm resembles the emission peak positions of LnQD NCs excited at 365 nm (Figure 6.6, inserted) and the color of LnQD NCs is the same as the NCs excited under 365 nm excitation (Figure 6.1 c,d). It is difficult to discern individual CdSe naoncrystals, even under HRTEM (Figure 6.1f) due to the sheer small size of the QDs. However, the tunable emission provides strong evidence of size-dependent optical properties of the CdSe QDs' green, orange and red emissions, which is attributed to the small CdSe nanocrystals in their quantum confinement states.

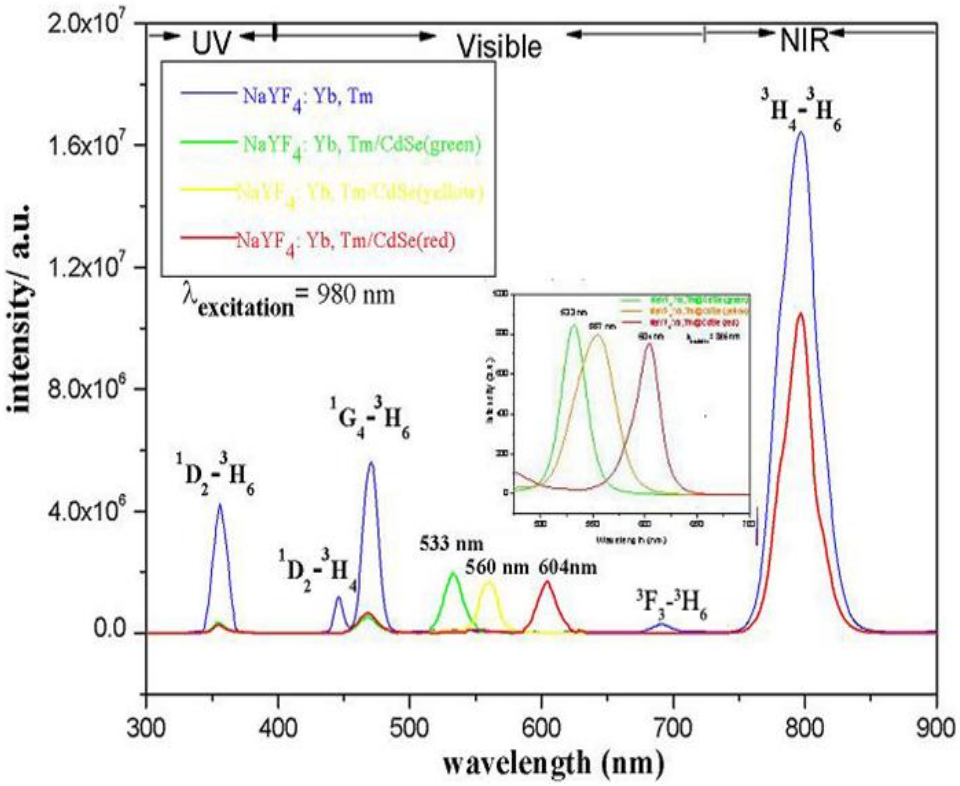

Figure 6.6 The UC emission of $NaYF_4$: Yb^{3+},Tm^{3+} (20%, 0.2%, blue line) core and $NaYF_4$: Yb^{3+},Tm^{3+}/CdSe core/shell NCs (green, yellow and red traces), excited at 980 nm. Insert: PL spectra of LnQD NCs excited at 365 nm.

The mechanism of energy transfer responsible for the UC emission of $NaYF_4$: Yb^{3+},Tm^{3+} core and $NaYF_4$: Yb^{3+},Tm^{3+}/CdSe core/shell LnQD NCs is shown in Figure 6.7. The sensitizers (Yb^{3+}) located in the core first absorbed 980 photons and successively transfer their energies to nearby Tm^{3+} ions to populate the Tm^{3+} ions to the $^1D_2$, $^1G_4$, $^3H_4$ states which relax radiatively to $^3H_6$ or $^3H_4$ which gives rise to the 355, 450, 485, 700 and 800 nm emissions. It was demonstrated that the UV emission at about 360 nm and blue emission at about 450 nm are four-photon processes, that is transition from $^1D_2$ to $^3H_6$ and $^3H_4$, respectively.[296] The blue emision at about 457 nm

is three-photon process which is $^1G_4$ to $^3H_6$. The red emission at about 700 nm is a two photon process ($^3F_3$ to $^3H_6$) and the NIR emission is due to $^3H_4$-$^3H_6$ transition. The energy of the excited Tm^{3+} ions in the $^1D_2$ and $^1G_4$ states fits the energy gap between the conduction and valence bands of the CdSe QDs, and thereby, energy was transferred to the QDs and excited them into higherlying electron or hole states and subsequent relaxation (t_e, t_h) to the lowest emitting state, giving rise to the green, yellow and red emission.

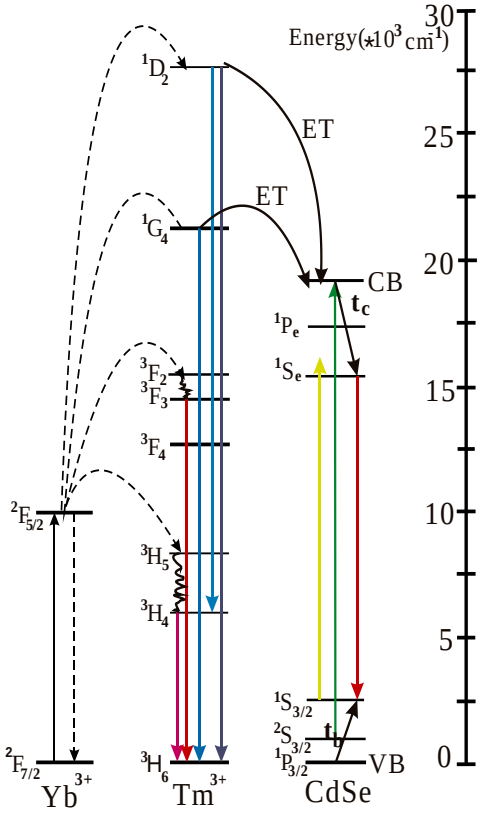

Figure 6.7 Proposed energy transfer UC processes for the emission of $NaYF_4$: Yb^{3+}, Tm^{3+} core and subsequent energy transfer to CdSe. The excitation state (black solid arrow), energy transfer (dotted wavy arrow), radiative decay (solid wavy arrow) are shown. The energy of UC NCs is transferred to QDs either through FRET or photon

reabsorption. The corresponding conduction band (CB) and valence band (VB) of CdSe QDs are presented.[297]

6.3 Conclusions

In summary, we have demonstrated a simple strategy to achieve tunable up-converting multicolor emission QDs. This has been achieved by optimizing the near-UV and blue up-converting emission of $NaYF_4$: Yb^{3+},Tm^{3+} NCs. The benefits of using lanthanide-based NCs as energy donors are: 1) The ability to optimize UC emission by proper control of sensitizer and emission ions in the lanthanide fluoride host; 2) their ability to resist photobleaching and photochemical degradation and 3) the reduction in background autofluorescence. Furthermore, these UCs are potential candidates for tissue/ protein distribution studies and small animal imaging, drug delivery. Over and above, this system of lanthanide/QDs (LnQD) core/shell NCs offers numerous benefits such as high photochemical stability and high signal-to-noise detection. Multicolor emissions of NCs have found applications in light emitting displays, lasers, optoelectronic devices and biological imaging.

Chapter 7: Anti-cAngptl4 Ab-conjugated N-TiO_2/$NaYF_4$:Yb,Tm Nanocomposite Near Infrared-Triggered Drug Release and Enhanced Targeted Cancer Cell Ablation

7.1 Introduction

Near infrared-induced drug release and cancer therapy using inorganic nanoparticles have generated much interest because near infrared (NIR) radiation is safe to the body and can penetrate deeper into tissues.[298,299,300] Of the various kinds of nanoparticles available, Au nanoparticles have been utilized in a gold-nanoparticle-mediated hyperthermia system to kill cancer cell and deliver drug by using NIR laser as an excitation.[299,300] Under NIR irradiation, the gold nanoparticles absorb the photon energy and convert it into heat, which raises the temperature of the tissue and eradicate cancer cells by disrupting the cell membrane.[301] Targeted drug delivery based on the NIR-induced photothermal effect of Au nanoparticles also has been reported.[300] Various modifications of Au nanoparticles to enhance the cancer cell killing and drug delivery have been undertaken.[302-304] However, gold nanoparticle is very expensive, which increase the already hefty healthcare costs.

TiO_2 nanoparticles are also good candidates for drug delivery and cancer therapy owing to their advantages of high activity, high stability, non-toxicity and low costs.[305-307] For these reported research works on cancer therapy and drug release, the

main principle is the formation of electron-hole pairs in the TiO_2 under UV light irradiation and thereby create highly reactive radical oxygen species (ROS). In cancer therapy, ROS can damage the cancer cell membrane and induce programmed cancer cell death,[307] while in drug release, ROS can sever the hydrocarbon chains attached on the surface of TiO_2 and thus leads to the release of drug.[307] However, besides low tissue penetration, the usage of high-energy UV light can cause photo-damage to biological specimen.[308]

It is desirable to develop a modified TiO_2 nanoparticle which can be activated by NIR laser to deliver drug and kill cancer cell. Rare earth-doped $NaYF_4$ upconversion nanoparticles (UCNPs) can emit bright fluorescence (green, blue, etc) under NIR light excitation. In addition, rare earth-doped $NaYF_4$ UCNPs is stable and has low cytotoxicity, which hence can potentially be applied to *in vivo* imaging.[298] It is reasonable that the emission of bright fluorescence from rare earth-doped $NaYF_4$ UCNPs can be absorbed by photocatalyst to produce ROS. Qin et al had reported the preparation of $YF_3:Yb^{3+},Tm^{3+}/TiO_2$ core/shell nanoparticles, which showed photocatalytic activity under NIR irradiation due to the photoactivation of TiO_2 by the upconverted UV emission.[307] However, UV light can cause photo-damage to biological specimen and the efficiency of NIR to UV conversion is relatively low.[112,308,309] NIR to visible light upconversion is more efficient.[310] Li et al. had reported a NIR photocatalyst, $NaYF_4:Yb^{3+},Tm^{3+}$/CdS composite, which could degrade Rhodamine B and Methylene blue (MB) under NIR irradiation.[310] Unfortunately, CdS is toxic and unstable, which limits its applications *in vivo* application.[311]

In this chapter, we report the synthesis of NIR-active N-TiO_2/$NaYF_4$:Yb^{3+},Tm^{3+} nanocomposites (NCs) for the first time, and investigate its drug release and targeted cancer cell killing using a safe NIR 980 nm laser. Under NIR laser irradiation, the NIR-to-Vis UCNPs ($NaYF_4$:Yb^{3+},Tm^{3+}) emit visible light (λ = 470 nm), which can excite N-doped TiO_2 to generate electron-hole pairs for redox reaction, as shown in Scheme 7.1. We attached a fluorescence dye, 7-methoxycoumarin-3-carboxylic acid (a model drug) on the surface of N-TiO_2/$NaYF_4$:Yb^{3+},Tm^{3+} to investigate NIR-induced drug release. Anti-cAngptl4 Ab-conjugated nanocomposites were demonstrated to have targeted cancer cell ablation activities.

7.2 Results and Discussion

FTIR spectra (Figure 7.1) of the thioglycolic acid-modified N-TiO_2 (TGA-N-TiO_2) and $NaYF_4$:Yb^{3+},Tm^{3+} show the presence of carboxyl and -O-H respectively, which enables the strong bonding between N-TiO_2 and $NaYF_4$:Yb^{3+},Tm^{3+}. The peaks at 1630 and 3100-3700 cm^{-1} are attributed to the stretching vibrations of the O-H bending of adsorbed water molecules and O-H absorbed on $NaYF_4$. The peaks at 1160 and 1560 cm^{-1} are assigned to the C-O stretching vibration and carboxyl stretching vibration, respectively.

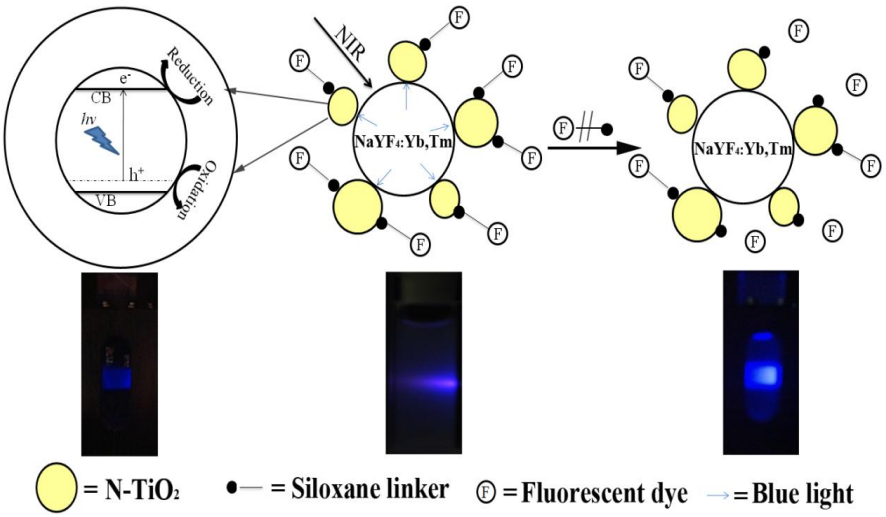

Scheme 7.1 Diagram showing the release principle of a fluorescent dye (model drug) from the N-TiO_2/$NaYF_4$:Yb^{3+},Tm^{3+} upon NIR irradiation.

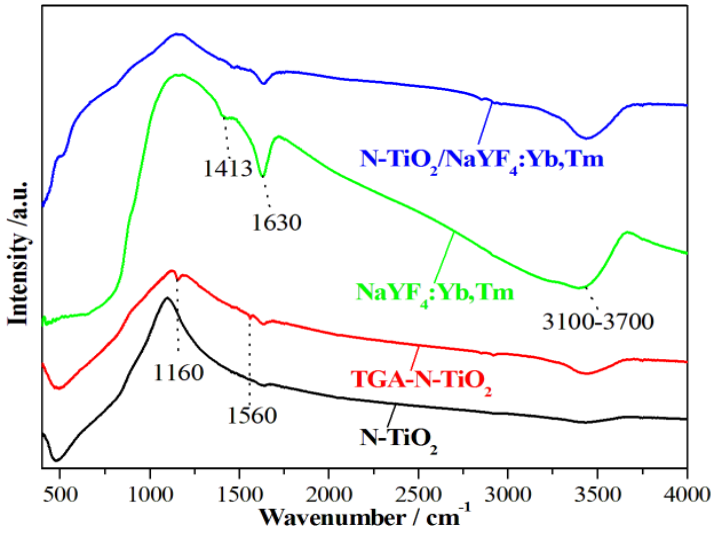

Figure 7.1 FTIR spectra of N-TiO_2, TGA-N-TiO_2, $NaYF_4$:Yb^{3+},Tm^{3+} and N-TiO_2/$NaYF_4$:Yb^{3+},Tm^{3+}.

Figure 7.2 shows the TEM images of $NaYF_4$:Yb^{3+},Tm^{3+} NPs and N-TiO_2/$NaYF_4$:Yb^{3+},Tm^{3+} nanocomposite, respectively, while insert displays the

magnified HRTEM images. Compared to the image of $NaYF_4:Yb^{3+},Tm^{3+}$ NPs (Figure 7.2 a), the image of N-TiO_2/$NaYF_4:Yb^{3+},Tm^{3+}$ NPs (Figure 7.2 b) shows that the $NaYF_4:Yb^{3+},Tm^{3+}$ NPs are surrounded by N-TiO_2. The atomic spacing of 0.32 nm and 0.352 nm observed in Figure 7.2 (inset) are attributed to (111) face of $NaYF_4$ and (101) face of anatase, respectively. EDX elemental scanning (Figure 7.3) of $NaYF_4:Yb^{3+},Tm^{3+}$ and N-TiO_2/$NaYF_4:Yb^{3+},Tm^{3+}$ NPs were performed to further determine the composition of the particles, which further prove the formation of N-TiO_2/$NaYF_4:Yb^{3+},Tm^{3+}$ NPs. Figure 7.4 shows the crystalline and phase information of the samples. For the N-TiO_2/$NaYF_4:Yb^{3+},Tm^{3+}$, in addition to the reflections of hexagonal phase $NaYF_4$, several weak peaks of anatase TiO_2 were observed. Figure 7.5 shows the N1s XPS spectra of the N-TiO_2, the smaller peak at 396.3 eV suggesting the doping of N into the lattice of N-TiO_2, which could enhance visible light absorption.

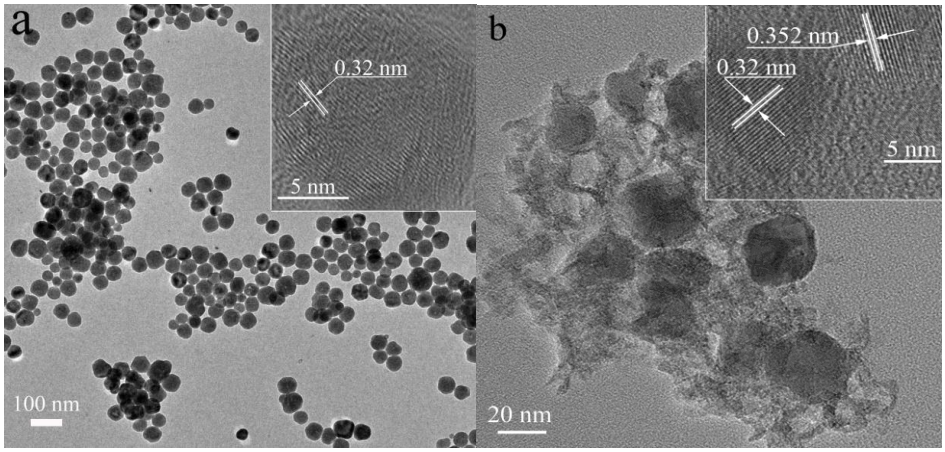

Figure 7.2 TEM images of the (a) $NaYF_4:Yb^{3+},Tm^{3+}$ and (b) N-TiO_2/$NaYF_4:Yb^{3+},Tm^{3+}$ NPs (inset: magnified HRTEM).

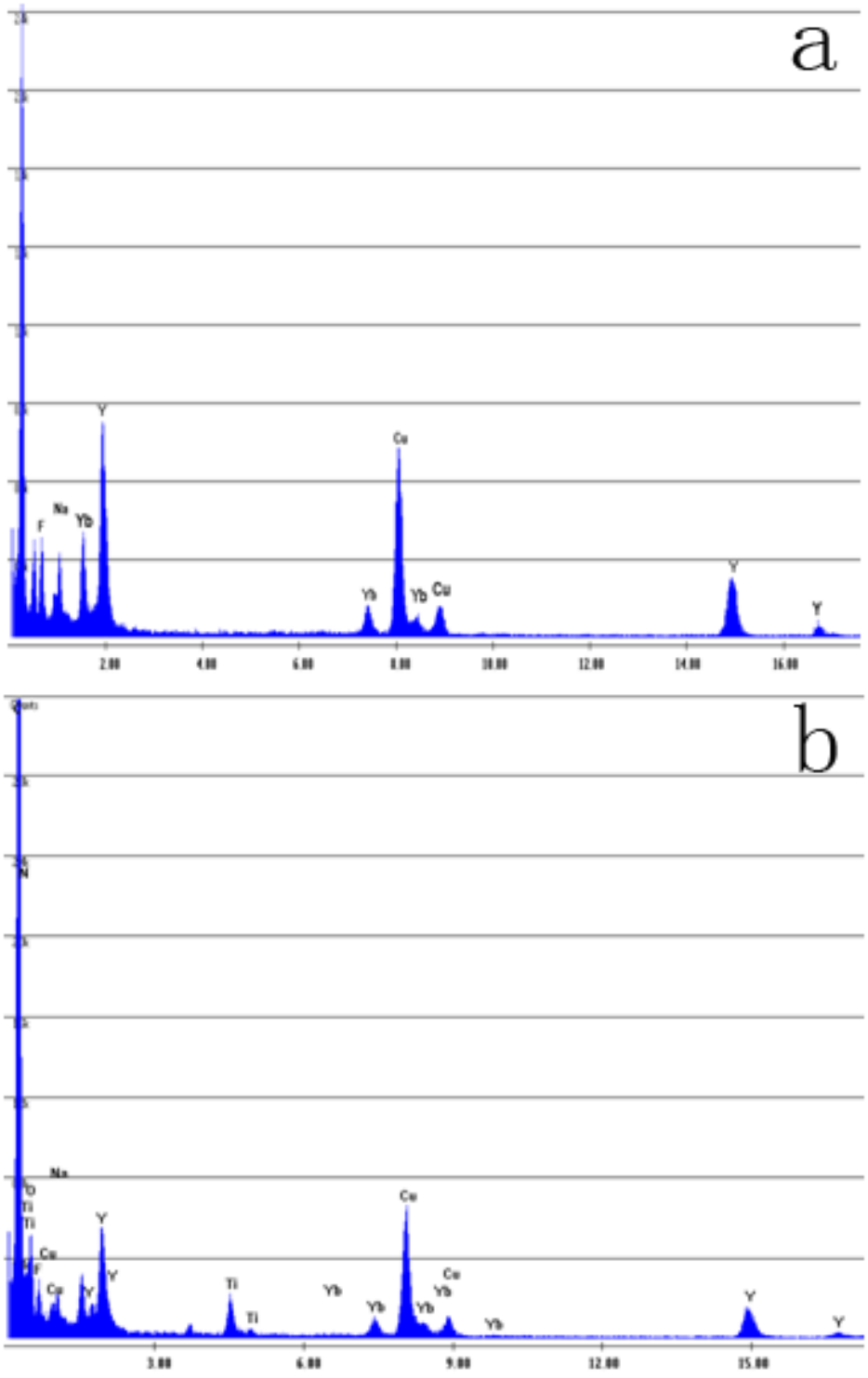

Figure 7.3 EDX pattern of the (a) $NaYF_4:Yb^{3+},Tm^{3+}$ and (b) $N\text{-}TiO_2/NaYF_4:Yb^{3+},Tm^{3+}$ NPs.

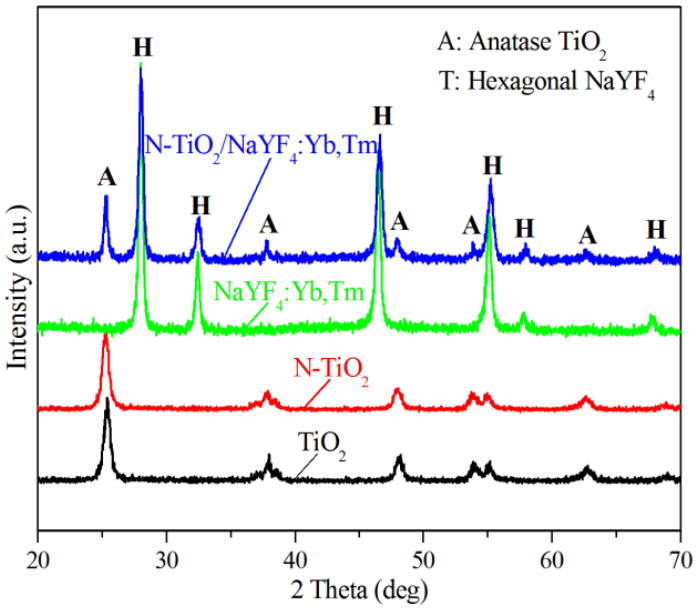

Figure 7.4 XRD spectra of TiO_2, N-TiO_2, $NaYF_4$:Yb^{3+},Tm^{3+} and N-TiO_2/$NaYF_4$:Yb^{3+},Tm^{3+} NPs.

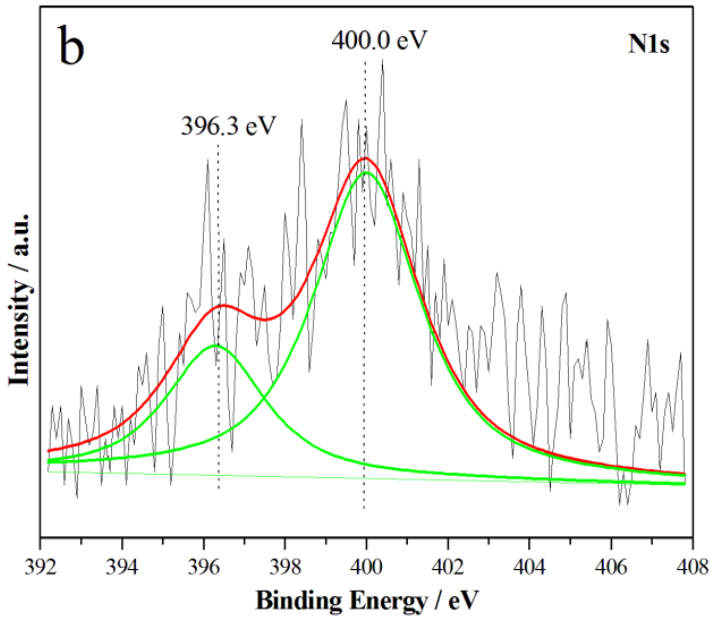

Figure 7.5 N1s XPS spectra of N-TiO_2.

NIR-triggered photocatalysis, drug release and cancer cell killing depend on the UC emission of visible light from $NaYF_4$:Yb^{3+},Tm^{3+} NPs and the light absorption on the

N-TiO_2 semiconductor. To transfer energy efficiently, the photon energy of the emitted light should activate electrons from N-TiO_2 valence band to conduction band and create highly reactive redox species.[312] The photoluminescence (PL) spectra of N-TiO_2, $NaYF_4$:Yb^{3+},Tm^{3+} and N-TiO_2/$NaYF_4$:Yb^{3+},Tm^{3+} NPs, and the light absorption spectrum of N-TiO_2 are presented in Figure 7.6. In Figure 7.7, the $NaYF_4$:Yb^{3+},Tm^{3+} NPs can absorb NIR photons (λ = 980 nm) and emit blue light(470 nm) (Figure 7.6, inset). As shown in Figure 7.6 (a), the N-TiO_2 exhibits obvious light absorption at 470 nm, indicating its ability to absorb blue emission from $NaYF_4$:Yb^{3+},Tm^{3+} NPs. The $NaYF_4$:Yb^{3+},Tm^{3+} NPs were optimized to emit predominantly at blue, instead of both UV and blue, to avoid the harmful effect of UV emission to the cells. The PL intensity of the N-TiO_2/$NaYF_4$:Yb^{3+},Tm^{3+} NPs at blue emission peak of 470 nm (I_{470}) is much lower than that of $NaYF_4$:Yb^{3+},Tm^{3+}. The PL intensities of the N-TiO_2/$NaYF_4$:Yb^{3+},Tm^{3+} at emission peaks of 640 nm and 795 nm (I_{795}) are also lower than that of $NaYF_4$:Yb^{3+},Tm^{3+}, which probably because the surrounding N-TiO_2 blocks the absorption of NIR by $NaYF_4$:Yb^{3+},Tm^{3+} to some extent. However, the reductions of the emission peaks at 640 nm and 795 nm are much lower than that of the emission peak at 470 nm. The PL intensity ratio of I_{470}/I_{795} for N-TiO_2/$NaYF_4$:Yb^{3+},Tm^{3+} composite is 0.23, which is much smaller than the value of 0.43 for the pure $NaYF_4$:Yb^{3+},Tm^{3+}, suggesting that some blue light is absorbed by N-TiO_2.

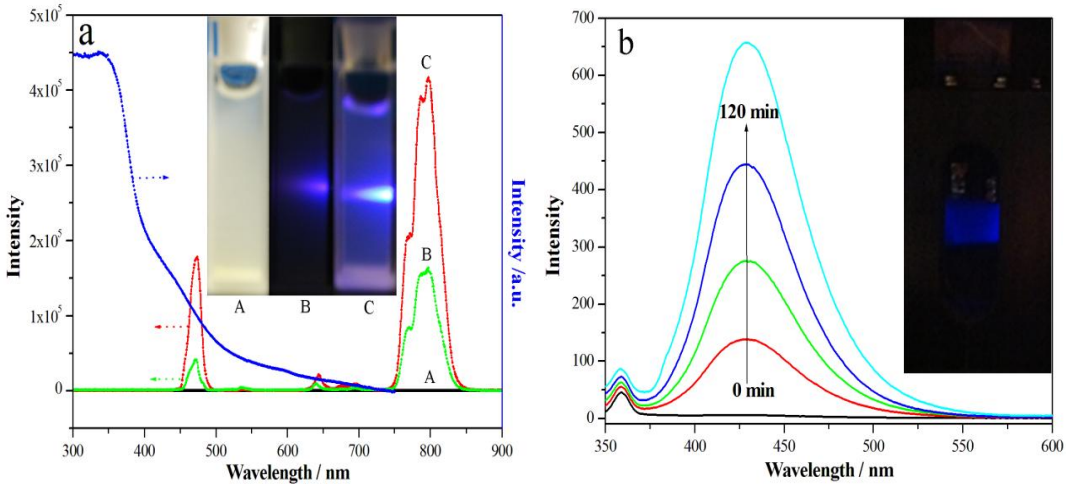

Figure 7.6 (a) Room temperature UC emission spectra of: (A) $NaYF_4$:Yb^{3+},Tm^{3+}; (B) N-TiO_2/$NaYF_4$:Yb^{3+},Tm^{3+}; (C) N-TiO_2. Inset: photographs showing the light emission of the particle solutions. (b) Time-dependent fluorescence spectra of the terephthalic acid solution (8×10^{-4} M) containing 10 mg of N-TiO_2/$NaYF_4$:Yb^{3+},Tm^{3+} upon NIR irradiation. Inset: Photograph shows the light emission of the 2-hydroxyterephthalic acid solution after NIR irradiation.

To further prove the energy transfer from $NaYF_4$:Yb^{3+},Tm^{3+} to N-TiO_2 and the generation of hydroxyl radicals, we employed a fluorescence approach based on a terephalic acid (TA) reaction.[196,278] Figure 7.6 (b) shows the fluorescence response for a TA solution after the N-TiO_2/$NaYF_4$:Yb^{3+},Tm^{3+} is irradiated with a 980 nm NIR laser for different time periods. The fluorescence intensity gradually increases with the increase of irradiation time. In addition, the strong blue fluorescence (Figure 7.6 (b) inset) upon excitation wavelength of 320 nm proves the formation of $OH^{\bullet}$ radicals. Control experiments involving $NaYF_4$:Yb^{3+},Tm^{3+} and N-TiO_2 were carried out for

comparison and the results were shown in Figure 7.8. It is obvious that no fluorescence can be seen for $NaYF_4:Yb^{3+},Tm^{3+}$ and N-TiO_2 under NIR irradiation.

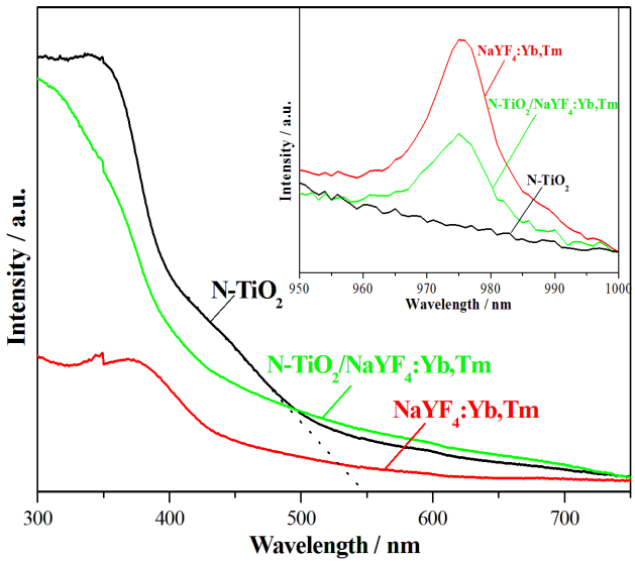

Figure 7.7 UV-Vis and NIR (inset) diffuse reflectance spectra of the N-TiO_2, $NaYF_4:Yb^{3+},Tm^{3+}$ and N-TiO_2/$NaYF_4:Yb^{3+},Tm^{3+}$.

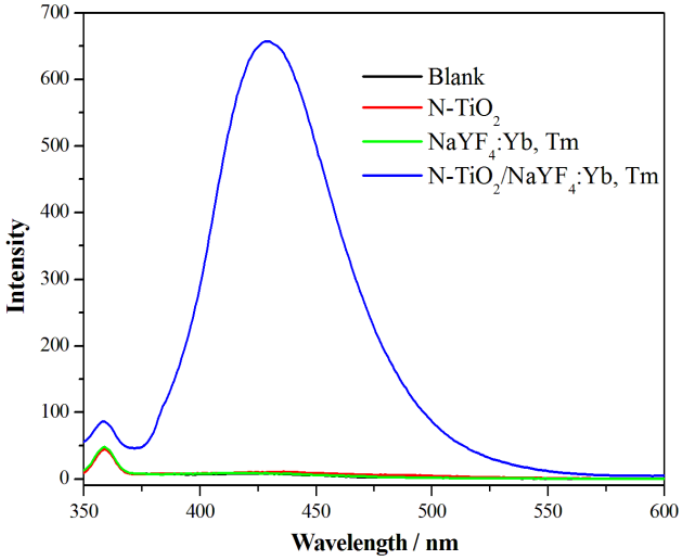

Figure 7.8 Spectra of the terephthalic acid solution containing N-TiO_2, $NaYF_4:Yb^{3+},Tm^{3+}$ and N-TiO_2/$NaYF_4:Yb^{3+},Tm^{3+}$ after NIR irradiation (120 min).

The photocatalytic activity of N-TiO_2/$NaYF_4$:Yb^{3+},Tm^{3+} NPs under NIR irradiation was measured using MB as a model and the results are shown in Figure 7.9. In Figure 7.9 (a), the absorption band at 664 nm decrease with the increase of NIR irradiation time, indicating the N-TiO_2/$NaYF_4$:Yb^{3+},Tm^{3+} is capable of degrading MB. Figure 7.9 (b) shows the comparison of the normalized concentration of MB decomposed by the N-TiO_2, $NaYF_4$:Yb^{3+},Tm^{3+} and N-TiO_2/$NaYF_4$:Yb^{3+},Tm^{3+} under NIR laser irradiation. It is obvious that 56% of MB was degraded for N-TiO_2/$NaYF_4$:Yb^{3+},Tm^{3+} after 30 h irradiation. However, no obvious MB degradation is observed on the pure N-TiO_2 and $NaYF_4$:Yb^{3+},Tm^{3+}.

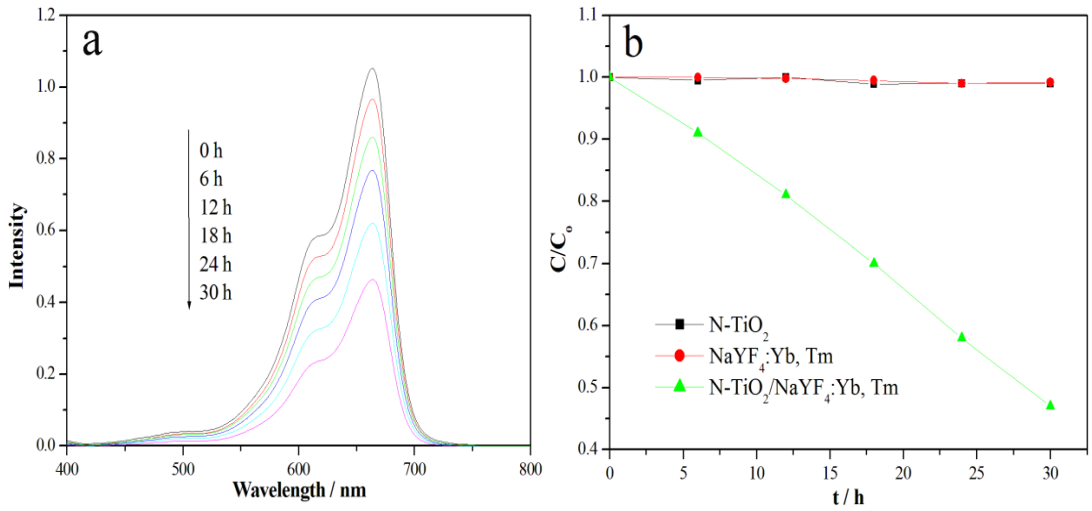

Figure 7.9 (a) Variation in absorbance spectra of MB catalyzed by N-TiO_2/$NaYF_4$:Yb^{3+},Tm^{3+} as a function of NIR irradiation time. (b) Comparison of the normalized concentration of MB decomposed by N-TiO_2, $NaYF_4$:Yb^{3+},Tm^{3+}, and N-TiO_2/$NaYF_4$:Yb^{3+},Tm^{3+} under 980 nm NIR laser irradiation.

To demonstrate NIR-triggered drug release, a model drug, which is a fluorescent dye (7-methoxycoumarin-3-carboxylic acid), was attached to the

N-TiO_2/$NaYF_4$:Yb^{3+},Tm^{3+} by using 3-aminopropyltriethoxysilane as a cross-linker. The N-TiO_2/$NaYF_4$:Yb^{3+},Tm^{3+} NPs were then dispersed into a quartz cuvette containing DI water. Before and after NIR irradiation, N-TiO_2/$NaYF_4$:Yb^{3+},Tm^{3+} NPs were removed and the remaining solution was measured by PL technique. Under NIR irradiation, the cleavage takes place at the anchoring siloxane groups, which triggered the release of the model drug into DI water. The results of NIR-induced drug release are shown in Figure 7.10.[313] Before NIR irradiation, there was no fluorescence observed, which confirm that no dye was released without NIR irradiation. After NIR irradiation, a strong blue fluorescence (Figure 7.10 inset) and high intensity peak at 405 nm was observed, which indicates the release of model drug into DI water under NIR irradiation.

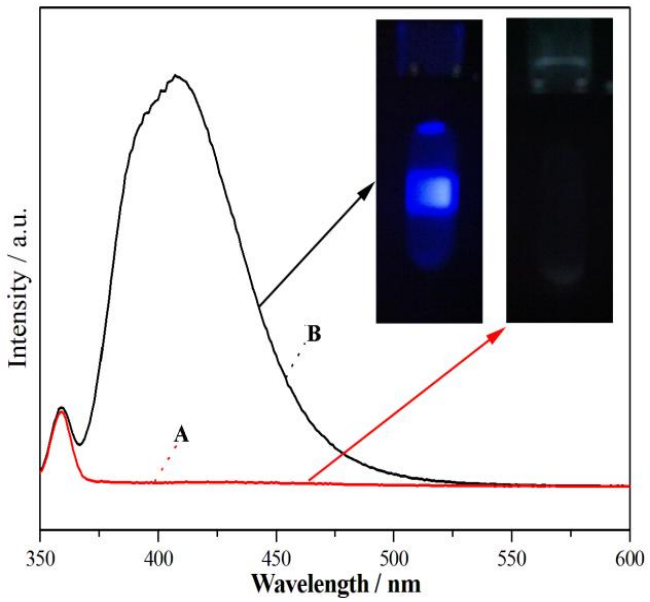

Figure 7.10 Fluorescence spectra of the 7-methoxycoumarin-3-carboxylic acid released from N-TiO_2/$NaYF_4$:Yb^{3+},Tm^{3+} NPs (a) before and (b) after 980 nm NIR irradiation. Inset: photographs show the light emission of the

7-methoxycoumarin-3-carboxylic acid solution before and after NIR irradiation, respectively.

The potential application of the N-TiO_2/$NaYF_4$:Yb^{3+},Tm^{3+} in targeted cancer cell killing using NIR laser was also explored in this work. The monoclonal antibody against fibrinogen-like domain of human angiopoitein-like 4 (anti-cAngptl4; clone mAb 11F6C4) was generated in-house and was previously described by Zhu et al..[314] Fluorescence Activated Cell Sorting (FACS) analysis (Figure 7.11) showed an increase in apoptotic A-5RT3 cells (Annexin V^+/PI^+ and Annexin V^+/PI^-) when treated with anti-cAngptl4 Ab nanoparticles when compared with unconjugated nanoparticles, even in the absence of NIR exposure (unconjugated vs anti-cAngptl4-conjugated: 7.53 % vs 13.67 %). Upon NIR exposure, anti-cAngptl4 Ab-NCs treated A-5RT3 showed a further ~2.5-fold increase (31.49 %) in apoptotic cells. Although there was a slight increase in the percentage of apoptotic cells in NIR exposed unconjugated NCs treated A-5RT3 (9.8 %), this difference was not statistically significant. FACS analysis also showed no significant difference in the percentage of apoptotic HaCaT cells treated with unconjugated nanoparticles regardless of NIR exposure, suggesting that the NCs exerted their cytotoxic effects only in close proximity to the cells. The functionalization of the NCs with anti-cAngptl4 antibody conferred selective anti-tumor property. The experiments were repeated except that HaCaT were prelabelled and similar results were obtained.

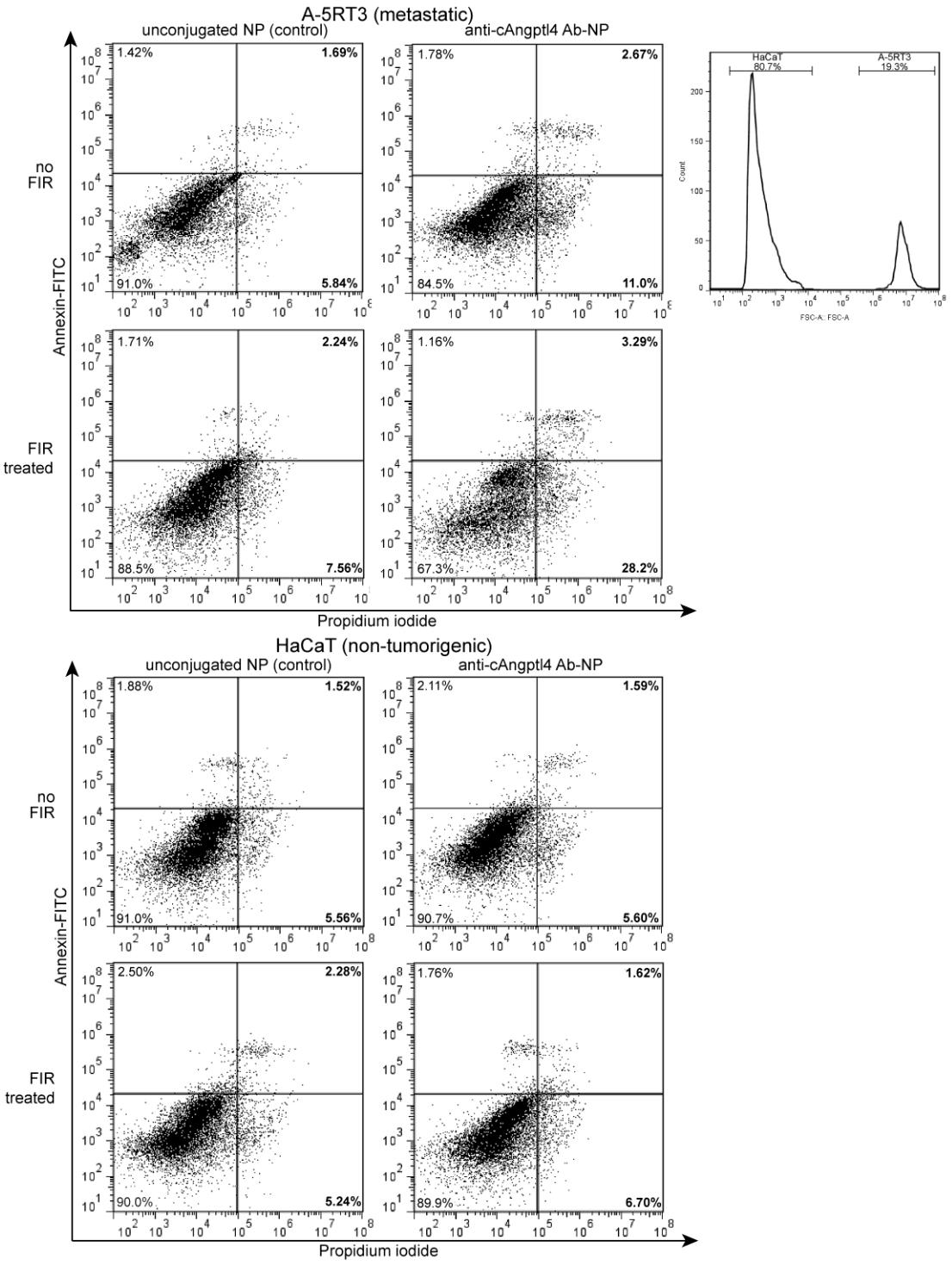

Figure 7.11 FACS analysis of apoptotic A-5RT3 cells (Annexin V^+/PI^+ and Annexin V^+/PI^-) when treated with anti-cAngptl4 Ab nanoparticles and unconjugated nanoparticles, in and in the absence of NIR exposure.

The mechanisms for the NIR-induced photocatalysis, drug release and cancer cell killing are shown in Scheme 7.2. Under NIR irradiation, the sensitizers (Yb^{3+}) in the $NaYF_4$:Yb^{3+},Tm^{3+} absorb 980 nm photons, successively transfer their energies to neighboring Tm^{3+} ions and populate the Tm^{3+} ions to the $^1G_4$ and $^3H_4$ states.[23,196] Then the excited Tm^{3+} ions relax radiatively to $^3H_6$ or $^3H_4$ and gives rise to three characteristics emissions at 470, 650 and 800 nm, corresponding to $^1G_4 \rightarrow {}^3H_6$, $^1G_4 \rightarrow {}^3H_4$ and $^3H_4 \rightarrow {}^3H_6$ transitions, respectively. The predominant blue emission from $NaYF_4$:Yb^{3+},Tm^{3+} UCNPs is at 470 nm (Figure 7.2 (a)). The N-TiO_2 exhibits strong absorption at 470 nm in Figure 7.2 (a). Herein, the blue emission can be absorbed by the surrounding N-TiO_2, which leads to the generation of holes in the valence band and electrons in the conduct band of the N-TiO_2, and thereby creating highly reactive radical species (OH•). The highly active OH• radical species can degrade MB, kill cancer cell [315] and scissor the hydrocarbon chains attached on the surface of the N-TiO_2/$NaYF_4$:Yb^{3+},Tm^{3+} leading to the release of drug and selectively killed cancer cells when brought to their close proximity, through a cancer-targeting antibody in the current case (Scheme 7.1b).

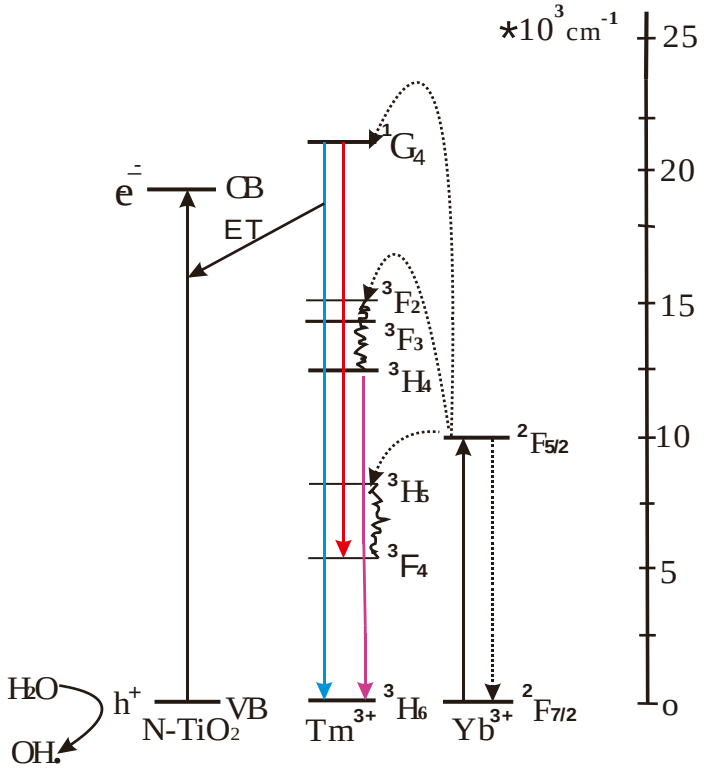

Scheme 7.2 Proposed UC processes for the emission of $NaYF_4$: Yb^{3+}, Tm^{3+} core and subsequent energy transfer to N-TiO_2 under 980 nm NIR excitation. The excitation state (black solid arrow), energy transfer (dotted wavy arrow), radiative decay (solid wavy arrow). The UCNPs energy is transferred to TiO_2 either through FRET or photon reabsorption. The corresponding conduction band (CB) and valence band (VB) of TiO_2 are shown.

7.3 Conclusions

In summary, we have developed NIR-activated N-TiO_2/$NaYF_4$:Yb,Tm nanocomposites. The NIR laser is safe to the body and can penetrate deeper into

tissues. Herein, we have explored its potential application in *in vitro* NIR-triggered drug release and targeted cancer cells killing. The current study demonstrates that conjugating the NCs with anti-cAngptl4 antibody conferred targeted anti-tumor property.

Chapter 8: Conclusions and Recommendations

8.1 Conclusions

The works presented in the preceding chapters of this dissertation show the efforts towards synthesis and tailoring of new multifunctional lanthanide nanomaterials for nanomedicine. Different types of lanthanide nanomaterials were synthesized and their potential applications in fluorescence microscopy and MRI were tested. Detail characterizations and analysis were performed to study the properties and the mechanism involved in the fluorescence emission of the nanomaterials was investigated. In another aspect, near-UV and blue up-converting emission of $NaYF_4$: Yb^{3+}, Tm^{3+} UCNPs were optimized to excite QDs and TiO_2. Tunable multicolor emissions can be achieved and their potential applications in triggered drug release and cancer cell killing have been investigated. The important results and finding of this study are summarized as follows:

(1) A new type of multifunctional lanthanide NPs that can function as dual-mode contrast agent in high magnetic field MR imaging and optical imaging is synthesized. MRI sensitivity is increased in higher magnetic field and higher spatial resolution, a better signal-to-noise ratio and reduced scan time can be achieved. The sensitivity of the as-synthesized contrast agents, namely r_2, is higher than that of current used ones, proving their efficiency as contrast agents in MRI. In addition, efficiently UC fluorescence is achieved without compromising the MRI contrast enhancement by growing a ytterbium-enriched secondary magnetic layer on the first layer.

(2) A simple strategy is conceived to synthesize and tailor the lanthanide nanorods for UC fluorescence and tunable T_1-T_2 dual mode contrast enhancement in MRI. This is the first demonstration of embedding UC emitters and tunable both positive and negative T_1 and negative T_2 properties into a single nanomaterials, all such properties arise solely from lanthanide ions.

(3) By optimizing the UV and blue emission from $NaYF_4$: Yb^{3+}, Tm^{3+} NCs, color-tunable UC emission of QDs is achieved. The as-obtained optimal UV and blue emission of $NaYF_4$: Yb^{3+}, Tm^{3+} NCs are used to excite the QDs to re-emit at green, yellow and red. This system of lanthanide/QDs (LnQD) core/shell NCs offers numerous benefits such as high photochemical stability, high signal-to-noise detection and multiplexing capabilities. Multicolor emissions of NCs have found applications in light emitting displays, lasers, optoelectronic devices and biological imaging.

(4) The NIR-triggered N-TiO_2/$NaYF_4$:Yb^{3+},Tm^{3+} NPs were synthesized and their applications in triggered drug release and cancer cell killing were investigated. Under NIR laser irradiation, the blue UC emissions from $NaYF_4$: Yb^{3+},Tm^{3+} UCNPs are absorbed by N-doped TiO_2 to generate electron-hole pairs for redox reaction and its potential applications in triggered *in vivo* control drug release and cancer cells ablation is explored.

8.2 Recommendations

Lanthanide doped nanomaterials with novel optical and magnetic properties are one of the most promising candidates in biomedical applications. In order to fully realize their potential in biomedical applications, the author proposes the following recommendations for improvement of the lanthanide doped nanomaterials investigated in this dissertation, and future development of lanthanide-doped nanomaterials in general.

(1) Fundamental studies of the effects of Yb^{3+} dopants and the shell thickness on the $NaYF_4$:Yb^{3+},Er^{3+}/$NaDyF_4$: Yb^{3+} nanomaterials: In this dissertation, the problem of up-conversion quenching by Dy^{3+} ions have been circumvented by adopting a core-shell configuration and incorporating Yb^{3+} ions into the shell. The possible explanations are: (1) the depopulation of $^4I_{11/2}$ (Er^{3+}) and $^2F_{5/2}$ (Yb^{3+}) by Dy^{3+} ions and (2) the presence of an outer layer or shell structure to improve the fluorescence of the NCs.

A fundamental study is recommended for future work to clearly elucidate how the energy transfers are affected by the concentration of Yb^{3+} ions and how the shell thickness influences the emission properties of the nanomaterials. This could be done using a laser flash photolysis system. Combined with MRI relaxivities studies, optimized UC emissions and T_2 contrasts will enable the realization of an efficient lanthanide-doped nanomaterial as a dual modal contrast agent.

(2) To investigation effect of Dy^{3+} ions on the longitudinal relaxivity induced by Gd^{3+} ions. Gd^{3+} ions, which have seven unpaired electron, are known to have an excellent longitudinal nuclear relaxation enhancing properties due to its long electronic relaxation time. Most of the Gd^{3+}-based contrast agents have shown positive T_1 contrast images. However, in our observation, the nanomatetrials exhibits negative T_1 contrast enhancement due to the large T_1 relaxation time. The presence of Dy^{3+} ions have affected the T_1 relaxivity induced by the Gd^{3+} ions in the commonly used spin-echo sequence. Choi and coworkers reported similar findings, that the coupling process between the electron spins of the T_1 contrast agent and nuclear spins of water is perturbed in the presence of additional magnetic field generated by T_2 contrast agent in close proximity. [316] The water exchange rate of the Dy^{3+} ions is faster than that of the Gd^{3+} ions, hence the presence of Dy^{3+} ions quickens T_1 relaxation in Gd ions, leading to a lower r_1 value.

A fundamental study is recommended for future work to clearly address how the paramagnetic property of Dy^{3+} ions affects the Gd^{3+} ions or vice-verse, which in turns affects the T_1 relaxivity. A silica insulating layer with different shell thickness can be incorporated to physically separate the Dy^{3+} and Gd^{3+} ions. Magnetic measurement such as SQUID could be used to study the magnetic response of the nanomaterials under varying magnetic fields. By undertaking such studies, it is hoped that the magnetic properties of such nanomaterials could be better understood, which will enable us to design and optimize nanomaterial with efficient T_1 and T_2 contrast enhancement for more effective deep-tissue imaging.

(3) To devise a one-pot synthesis method of water-dispersible, uniform and monodisperse lanthanide NPs. Water-dispersibility of NPs is one of the important requirements for bio-applications. The limitation of many synthesis methods, including the thermal decomposition methods used in the current work, is that post-synthesis surface modification is necessary to render the nanomaterials biocompatible. Hence, it is highly desirable to devise a one-pot synthetic strategy to produce water-dispersible, uniform and monodisperse multifunctional NCs. Several groups reported fabrication strategies of one-pot water-dispersible NCs with the aid of polymers or surfactants, such as PEG-derivatives (e.g. monocarboxyl-termined poly(ethylene glycol)) or surfactants (e.g. polyvinylpyrrolidone).[23] However, uniformity, monodispersity, and stability of these NPs remain as issues to be addressed. Thus, concerted efforts are needed to devise synthetic strategies for fabrication of water-dispersible NPs with desired surface properties for bioconjugations. The development of new water-dispersible and biocompatible amphiphilic micelles or polymeric ligands or bifunctional ligands as strong stabilizing agents in aqueous environment may resolve such issues.

(4) Further development of lanthanide-doped nanomaterials for treatment and diagnosis. Multifunctional nanomaterials systems hold great promise for future therapeutic applications. Accurate and early diagnosis coupled with on-site delivery and treatment using suitable therapeutic agents at the early stage of the disease will facilitate timely clinical intervention and can mitigate patient risk and disease progression. As such, lanthanide-based nanomaterials can potentially achieve

simultaneously, efficient detection and imaging, targeting and on-demand drug delivery as well as a non-invasive means of tracking and monitoring the subsequent therapeutic effects. It is envisioned that modeling light-NPs-tissue interactions during therapy and integration of these algorithms together with real-time imaging technologies will allow therapy optimization,[317] whilst improving the delivery methods of these NPs will allow accumulation of a larger number of particles to the site of interest (e.g. tumor), therefore enhancing both imaging contrast and therapy efficacy. Both of these developments will lead to better understanding of the fundamentals of cells/tissues/organs-NPs interaction. Such understanding of biological responses to nanomaterials is needed to develop and safely utilize nanomaterials for therapeutic applications in the future, as it allows us to predict risk and benefit parameters and hence create a critical path to nano-product development.

A key concern in the development of rare-earth nanotechnology is a stable and relatively cheap supply of raw materials. Besides biomedical applications, rare earth compounds are needed for many of the sophisticated civilian and military technologies including computer memory, DVD's, rechargeable batteries, cell phones, car catalytic converters, magnets, fluorescent lighting and much more. For instance, neodyminm is needed for headphones and hybrid electric cars. Samarium is crucial in the manufacture of missiles. However, significant amounts of rare earth elements are produced in only a few counties, and China is the dominant producer of rare earth elements, and is believed to be responsible for over 95% of the world mine production on a rare earth oxide equivalent basis. The concentration of rare earth element

production in China raises the important issue of supply vulnerability. As in early 2010, when China announced that they would restrict their rare earth exports to ensure a supply for domestic manufacturing, the price soared. Attempt to find alternatives to rare earth elements is undergoing; however, due to the unique properties of the rare earth materials, these substitutes are not as good as rare earth elements. It is possible that suitable alternatives to rare earth elements could one day be discovered, but in the mean time, a stable supply of rare earth compounds is crucial to major industries globally. This has turned into a tricky as well as politically sensitive issue.

It is in my opinion that at the current stage of research and development, as the amount of lanthanide materials used is very minute, the price of the raw materials should not be a major issue. Should the technology be translated into clinical application in the future, as the amount of lanthanide materials administered for diagnosis or/and treatment, be it for biomedical imaging or targeted cancer cell killing, will be in milli- or even micro-molar quantity. Therefore, the cost of the raw materials would probably not be a major stumbling block. The challenge for engineers and scientists is to design and tailor the nanomaterials to be highly sensitive, so that only a small quantity is needed for high efficiency applications, as well as reducing potential toxicology effect (see point 5).

(5) Toxicity evaluation of lanthanide NPs. The scientific hurdles in bringing nanoengineered products to patients, specifically in pre-clinical, clinical and manufacturing phases of product development still needs to be addressed before lanthanide-based nanomaterial can move forward. Determination of the long-term

toxicity of the NPs is still one of the main hurdles that require the establishment of standards and testing protocols that can provide benchmarks for the development of novel classes of materials including lanthanide-based materials. At present, the lack of *in vivo* studies involving lanthanide-based nanomaterials means that there is limited information about the long-term efficacy and health implications of using these products. Limited *in vitro* studies focused on toxicology of lanthanide-based nanomaterials showed that the concentration of lanthanide-metals will affect the upregulation of inflammatory genes, whilst the type of assay methods used to assess cytotoxicity needs to be optimized. [318] In addition, further studies need to be carried out to evaluate the post-exposure effects of lanthanide-based nanomaterials on cell biology and physiology.

REFERENCES

1 Brigger, I., Dubernet, C., Couvreur, P. Nanoparticles in cancer therapy and diagnosis. *Advanced Drug Delivery Reviews* **54**, 631-651 (2002).

2 Hamley, I. W. Nanotechnology with soft materials. *Angewandte Chemie - International Edition* **42**, 1692-1712 (2003).

3 Katz, H. E. Recent advances in semiconductor performance and printing processes for organic transistor-based electronics. *Chemistry of Materials* **16**, 4748-4756 (2004).

4 Panyam, J., Labhasetwar, V. Biodegradable nanoparticles for drug and gene delivery to cells and tissue. *Advanced Drug Delivery Reviews* **55**, 329-347 (2003).

5 Kim, D. K. & Dobson, J. Nanomedicine for targeted drug delivery. *Journal of Materials Chemistry* **19**, 6294-6307 (2009).

6 Moghimi, S. M., Hunter, A. C. & Murray, J. C. Nanomedicine: Current status and future prospects. *FASEB Journal* **19**, 311-330 (2005).

7 Riehemann, K., Schneider, S. W., Luger, T. A., Godin, B., Ferrari, M., Fuchs, H. Nanomedicine - Challenge and perspectives. *Angewandte Chemie - International Edition* **48**, 872-897 (2009).

8 Debbage, P., Jaschke, W. Molecular imaging with nanoparticles: Giant roles for dwarf actors. *Histochemistry and Cell Biology* **130**, 845-875 (2008).

9 Duncan, R. Polymer conjugates as anticancer nanomedicines. *Nature Reviews Cancer* **6**, 688-701 (2006).

10 Weissleder, R., Mahmood, U. Molecular imaging. *Radiology* **219**, 316-333 (2001).

11 Jennings, L. E., Long, N. J. 'Two is better than one'-probes for dual-modality molecular imaging. *Chemical Communications*, 3511-3524 (2009).

12 Waters, E. A., Wickline, S. A. Contrast agents for MRI. *Basic Research in Cardiology* **103**, 114-121 (2008).

13 Yoo, B., Pagel, M. D. An overview of responsive MRI contrast agents for molecular imaging. *Frontiers in Bioscience* **13**, 1733-1752 (2008).

14 Sharma, P., Brown, S., Walter, G., Santra, S., Moudgil, B. Nanoparticles for bioimaging. *Advances in Colloid and Interface Science* **123-126**, 471-485 (2006).

15 Wang, F., Banerjee, D., Liu, Y., Chen, X., Liu, X. Upconversion nanoparticles in biological labeling, imaging, and therapy. *Analyst* **135**, 1839-1854 (2010).

16 Louie, A. Multimodality imaging probes: Design and challenges. *Chemical Reviews* **110**, 3146-3195 (2010).

17 Corr, S. A., Rakovich, Y. P., Gun'Ko, Y. K. Multifunctional magnetic-fluorescent nanocomposites for biomedical applications. *Nanoscale Research Letters* **3**, 87-104 (2008).

18 Fang, C., Zhang, M. Multifunctional magnetic nanoparticles for medical imaging applications. *Journal of Materials Chemistry* **19**, 6258-6266 (2009).

19 Liong, M., Lu, J., Kovochich, M., Xia, T., Ruehm, S. G., Nel, A. E., Tamanoi, F., Zink, J. I. Multifunctional inorganic nanoparticles for imaging, targeting, and drug delivery. *ACS Nano* **2**, 889-896 (2008).

20 Lewin, M. C., N.; Tung, C. H.; Tang, X. W.; Cory, D.; Scadden, D. T.; Weissleder, R. Tat peptide-derivatized magnetic nanoparticles allow in vivo tracking and recovery of progenitor cells. *Nature Biotechnology* **18**, 410-414 (2000).

21 Bottrill, M., Kwok, L., Long, N. J. Lanthanides in magnetic resonance imaging. *Chemical Society Reviews* **35**, 557-571 (2006).

22 Wang, F., Tan, W. B., Zhang, Y., Fan, X., Wang, M. Luminescent nanomaterials for biological labelling. *Nanotechnology* **17**, R1-R13 (2006).

23 Wang, F., Liu, X. Recent advances in the chemistry of lanthanide-doped upconversion nanocrystals. *Chemical Society Reviews* **38**, 976-989 (2009).

24 Zhang, C., Sun, L., Zhang, Y., Yan, C. Rare earth upconversion nanophosphors: Synthesis, functionalization and application as biolabels and energy transfer donors. *Journal of Rare Earths* **28**, 807-819 (2010)..

25 Haase, M., Schäfer, H. Upconverting Nanoparticles. *Angewandte Chemie International Edition* **50**, 5808-5829 (2011).

26 Bae, K. H., Kim, Y. B., Lee, Y., Hwang, J. Y., Park, H., Park, T. G. Bioinspired synthesis and characterization of gadolinium-labeled magnetite nanoparticles for dual contrast T_1- and T_2-weighted magnetic resoance imaging. *Bioconjugated Chemistry* **21**, 505-512 (2010).

27 Na, H. B., Hyeon, T. Nanostructured T_1 MRI contrast agents. *Journal of Materials Chemistry* **19**, 6267-6273 (2009).

28 Yang, H., Zhuang, Y., Sun, Y., Dai, A., Shi X. X., Wu, D., Li, F., Hu, H., Yang, S. Targeted dual-contrast T_1- and T_2-weighted magnetic resonance imaging of tumors using multifunctional gadolinium-labeled superparamagnetic iron oxide nanoparticles. *Biomaterials* **32**, 4584-4593 (2011).

29 Rudin, M., Weissleder, R. Molecular imaging in drug discovery and development. *Nature Reviews Drug Discovery* **2**, 123-131 (2003).

30 Cho, E. C., Glaus, C., Chen, J., Welch, M. J., Xia, Y. Inorganic nanoparticle-based contrast agents for molecular imaging. *Trends in Molecular Medicine* **16**, 561-573 (2010).

31 Basilion, J. P., Yeon, S., Botnar, R. Magnetic Resonance Imaging: Utility as a Molecular Imaging Modality. *Current Topics in Developmental Biology* **70**, 1-33 (2005).

32 Huh, Y. M., Jun, Y. W., Song, H. T., Kim, S., Choi, J. S., Lee, J. H., Yoon, S., Kim, K. S., Shin, J. S., Suh, J. S., Cheon, J. *In vivo* magnetic resonance detection of cancer by using multifunctional magnetic nanocrystals. *Journal of the American Chemical Society* **127**, 12387-12391 (2005).

33 Lee, H., Mi, K. Y., Park, S., Moon, S., Jung, J. M., Yong, Y. J., Kang, H. W., Jon, S. Thermally cross-linked superparamagnetic iron oxide nanoparticles: Synthesis and application as a dual imaging probe for cancer in vivo. *Journal of the American Chemical Society* **129**, 12739-12745 (2007).

34 Insin, N., Tracy, J. B., Lee, H., Zimmer, R. M., Westervelt, R. M., Bawendi, M. G. Incorporation of iron oxide nanoparticles and quantum dots into silica microspheres. *ACS Nano* **2**, 197-202 (2008).

35 Li, L., Chen, D., Zhang, Y., Deng, Z., Ren, X., Meng, X., Tang, F., Ren, J., Zhang, L. Magnetic and fluorescent multifunctional chitosan nanoparticles as a smart drug delivery system. *Nanotechnology* **18**, doi: 10.1088/0957-4484/1018/1040/405102 (2007).

36 Zhang, H., Yee, D., Wang, C. Quantum dots for cancer diagnosis and therapy: Biological and clinical perspectives. *Nanomedicine* **3**, 83-91 (2008).

37 Zhang, Y., Wang, S. N., Ma, S., Guan, J. J., Li, D., Zhang, X. D., Zhang, Z. D. Self-assembly multifunctional nanocomposites with Fe_3O_4 magnetic core and CdSe/ZnS quantum dots shell. *Journal of Biomedical Materials Research - Part A* **85**, 840-846 (2008).

38 He, Y., Wang, H. F., Yan, X. P. Exploring Mn-doped ZnS quantum dots for the room-temperature phosphorescence detection of enoxacin in biological fluids. *Analytical Chemistry* **80**, 3832-3837 (2008).

39 Yong, K. Mn-doped near-infrared quantum dots as multimodal targeted probes for pancreatic cancer imaging. *Nanotechnology* **20**, doi: 10.1088/0957-4484/1020/1081/015102 (2009).

40 Bünzli, J. C. G., Piguet, C. Taking advantage of luminescent lanthanide ions. *Chemical Society Reviews* **34**, 1048-1077 (2005).

41 Gossuin, Y., Hocq, A., Gillis, P., Quoc Lam, V. Physics of magnetic resonance imaging: From spin to pixel. *Journal of Physics D: Applied Physics* **43** (2010).

42 Sorensen, A. G., Tievsky, A. L., Ostergaard, L., Weisskoff, R. M., Rosen, B. R. Contrast agents in functional MR imaging. *Journal of Magnetic Resonance Imaging* **7**, 47-55 (1997).

43 Sharma, P., Brown, S. C., Walter, G., Santra, S., Scott, E., Ichikawa, H., Fukumori, Y., Moudgil, B. M. Gd nanoparticulates: From magnetic resonance imaging to neutron capture therapy. *Advanced Powder Technology* **18**, 663-698 (2007).

44 Caravan, P., Ellison, J. J., McMurry, T. J., Lauffer, R. B. Gadolinium (III) chelates as MRI contrast agents: structures, dynamics and application. *chemical Reviews* **99**, 2293-2352 (1999).

45 Aime, S., Botta, M., Terreno, E. *Advances in Inorganic Chemistry* **57**,173-237 (2006).

46 Na, H. B., Song, I. C., Hyeon, T. Inorganic nanoparticles for MRI contrast agents. *Advanced Materials* **21**, 2133-2148 (2009).

47 Liu, Y., Chen, Z., Liu, C., Yu, D., Lu, Z., Zhang, N. Gadolinium-loaded polymeric nanoparticles modified with Anti-VEGF as multifunctional MRI contrast agents for the diagnosis of liver cancer. *Biomaterials* **32**, 5167-5176 (2011).

48 Malgorzata N., Joop A. P. MRI contrast agetns based on dysprosium or holmium. *Progress in Nuclear Magnetic Resonance Spectroscopy* **59**, 64-82 (2011).

49 Ivano Bertini, C. L., Giacomo P.. Magnetic susceptibility in paramagnetic NMR. *Progress in Nuclear Magnetic Resonance Spectroscopy* **40**, 249-273 (2002).

50 Briley-Saebo, K. C., Geninatti-Crich, S., Cormode, D. P., Barazza, A., Mulder, W. J. M., Chen, W., Giovenzana, G. B., Fisher, E. A., Aime, S., Fayad, Z. A. High-relaxivity gadolinium-modified high-density lipoproteins as magnetic resonance imaging contrast agents. *Journal of Physical Chemistry B* **113**, 6283-6289 (2009).

51 Corbin, I. R., Li, H., Chen, J., Lund-Katzy, S., Zhou, R., Glickson, J. D., Zheng, G. Low-density lipoprotein nanoparticles as magnetic resonance imaging contrast agents. *Neoplasia* **8**, 488-498 (2006).

52 Crich, S. G., Lanzardoy, S., Alberti, D., Belfiore, S., Ciampa, A., Giovenzana, G. B., Lovazzano, C., Pagliarin, R., Aime, S. Magnetic resonance imaging detection of tumor cells by targeting low-density lipoprotein receptors with Gd-loaded low-density lipoprotein particles. *Neoplasia* **9**, 1046-1056 (2007).

53 Perez-Baena, I., Loinaz, I., Padro, D., Garcá, I., Grande, H. J., Odriozola, I. Single-chain polyacrylic nanoparticles with multiple Gd(iii) centres as potential MRI contrast agents. *Journal of Materials Chemistry* **20**, 6916-6922 (2010).

54 Csajbók, É., Bányai, I., Elst, L. V., Muller, R. N., Zhou, W., Peters, J. A. Gadolinium(III)-loaded nanoparticulate zeolites as potential high-field MRI contrast agents: Relationship between structure and relaxivity. *Chemistry - A European Journal* **11**, 4799-4807 (2005).

55 Pereira, G. A., Ananias, D., Rocha, J., Amaral, V. S., Muller, R. N., Vander Elst, L., Tóth, É, Peters, J. A., Geraldes, C. F. G. C. NMR relaxivity of Ln^{3+}-based zeolite-type materials. *Journal of Materials Chemistry* **15**, 3832-3837 (2005).

56 Pereira, G. A., Norek, M., Peters, J. A., Ananias, D., Rocha, J., Geraldes, C. F. G. C. NMR Transversal relaxivity of aqueous suspensions of particles of Ln^{3+}-based zeolite type materials. *Dalton Transactions*, **17**, 2241-2247 (2008).

57 Sitharaman, B., Wilson, L. J. Gadofullerenes and gadonanotubes: A new paradigm for high-performance magnetic resonance imaging contrast agent probes. *Journal of Biomedical Nanotechnology* **3**, 342-352 (2007).

58 Sitharaman, B., Zakharian, T. Y., Saraf, A., Ashcroft, P. M. J., Pan, S., Pham, Q. P., Mikos, A. G., Wilson, L. J., Engler, D. A. Water-soluble fullerene (C_{60}) derivatives as nonviral gene-delivery vectors. *Molecular Pharmaceutics* **5**, 567-578 (2008).

59 Richard, C., Doan, B. T., Beloeil, J. C., Bessodes, M., Tóth, É, Scherman, D. Noncovalent functionalization of carbon nanotubes with amphiphilic Gd^{3+}

chelates: Toward powerful T_1 and T_2 MRI contrast agents. *Nano Letters* **8**, 232-236 (2008).

60 Hsiao, J. K., Tsai, C. P., Chung, T. H., Hung, Y., Yao, M., Liu, H. M., Mou, C. Y., Yang, C. S., Chen, Y. C., Huang, D. M. Mesoporous silica nanoparticles as a delivery system of gadolinium for effective human stem cell tracking. *Small* **4**, 1445-1452 (2008).

61 Lin, Y. S., Hung, Y., Su, J. K., Lee, R., Chang, C., Lin, M. L., Mou, C. Y. Gadolinium(III)-incorporated nanosized mesoporous silica as potential magnetic resonance imaging contrast agents. *Journal of Physical Chemistry B* **108**, 15608-15611 (2004).

62 Taylor, K. M. L., Kim, J. S., Rieter, W. J., An, H., Lin, W. Mesoporous silica nanospheres as highly efficient MRI contrast agents. *Journal of the American Chemical Society* **130**, 2154-2155 (2008).

63 Jin, T., Yoshioka, Y., Fujii, F., Komai, Y., Seki, J., Seiyama, A. Gd^{3+}-functionalized near-infrared quantum dots for *in vivo* dual modal (fluorescence/magnetic resonance) imaging. *Chemical communications*, 5764-5766 (2008).

64 Koole, R., Mulder, W. J., van Schooneveld, M. M., Strijkers, G. J., Meijerink, A., Nicolay, K. Magnetic quantum dots for multimodal imaging. *Wiley interdisciplinary reviews. Nanomedicine and nanobiotechnology* **1**, 475-491 (2009).

65 Tani, W. B., Zhang, Y. Multi-functional chitosan nanoparticles encapsulating quantum dots and Gd-DTPA as imaging probes for bio-applications. *Journal of Nanoscience and Nanotechnology* **7**, 2389-2393 (2007).

66 Debouttière, P. J., Roux, S., Vocanson, F., Billotey, C., Beuf, O., Favre-Réguillon, A., Lin, Y., Pellet-Rostaing, S., Lamartine, R., Perriat, P., Tillement, O. Design of gold nanoparticles for magnetic resonance imaging. *Advanced Functional Materials* **16**, 2330-2339 (2006).

67 Marradi, M., Alcántara, D., De La Fuente, J. M., García-Martín, M. L., Cerdán, S., Penadés, S. Paramagnetic Gd-based gold glyconanoparticles as probes for MRI: Tuning relaxivities with sugars. *Chemical Communications*, 3922-3924 (2009).

68 Roberts, D., Zhu, W.L., Frommen, C. M., Rosenzweig, Z.. Synthesis of gadolinium oxide magnetoliposomes for magnetic resonance imaging. *Journal of Applied Physics* **87**, 6208 (2000).

69 Louis, C., Bazzi, R., Marquette, C. A., Bridot, J. L., Roux, S., Ledoux, G., Mercier, B., Blum, L., Perriat, P., Tillement, O.. Nanosized Hybrid Particles with Double Luminescence for Biological Labeling. *Chemistry of Materials* **17**, 1673-1682 (2005).

70 Miyawaki, J., Matsumura, S., Yuge, R., Murakami, T., Sato, S., Tomida, A., Tsuruo, T., Ichihashi, T., Fujinami, T., Irie, H., Tsuchida, K., Iijima, S., Shiba, K., Yudasaka, M. Biodistribution and ultrastructural localization of single-walled carbon nanohorns determined *in vivo* with embedded Gd_2O_3 labels. *ACS Nano* **3**, 1399-1406 (2009).

71 Huang, C. C., Liu, T. Y., Su, C. H., Lo, Y. W., Chen, J. H., Yeh, C. S. Superparamagnetic hollow and paramagnetic porous Gd_2O_3 particles. *Chemistry of Materials* **20**, 3840-3848 (2008).

72 Hu, K. W., Jhang, F. Y., Su, C. H. & Yeh, C. S. Fabrication of $Gd_2O(CO_3)_2 \cdot H_2O$/silica/gold hybrid particles as a bifunctional agent for MR imaging and photothermal destruction of cancer cells *Journal of Materials Chemistry* **19**, 2147-2153 (2009).

73 Vymazal, J., Bulte, J. W. M., Frank, J. A., Chiro, Gi. D., Brooks, R. A. Frequency dependence of MR relaxation times I. Paramagnetic ions. *Journal of Magnetic Resonance Imaging* **3**, 637-640 (1993).

74 Bulte, J. W. M., Wu, C., Brechbiel, M. W., Brooks, R. A., Vymazal, J., Holla, M., Frank, J. A. Dysprosium-DOTA-PAMAM dendrimers as macromolecular T_2 contrast agents: preparation and relaxometry. *Investigative Radiology* **33**, 841-845 (1998).

75 Kato, H., Kanazawa, Y., Okumura, M., Taninaka, A., Yokawa, T., Shinohara, H. Lanthanoid endohedral metallofullerenols for MRI contrast agents. *Journal of the American Chemical Society* **125**, 4391-4397 (2003).

76 Wang, F., Tan, W. B., Zhang, Y., Fan, X., Wang, M. Luminescent nanomaterials for biological labelling. *Nanotechnology* **17**, R1-R13 (2006).

77 Auzel, F. Upconversion and Anti-Stokes Processes with f and d Ions in Solids. *Chemical Reviews* **104**, 139-173 (2004).

78 Chen, X., Song, Z. Strong cooperative upconversion luminescence of ytterbium doped oxyfluoride nanophase vitroceramics. *Solid State Communications* **136**, 313-317 (2005).

79 Deng, D., Xu, S., Bao, R., Zhao, S., Wang, B., Wang, H., Ju, H. Blue cooperative upconversion in Yb^{3+}-doped glass ceramic containing $LiYF_4$ nanocrystals. *Journal of Physics D: Applied Physics* **42** (2009).

80 Xiao, K., Yang, Z. Blue cooperative luminescence in Yb^{3+}-doped barium gallogermanate glass excited at 976 nm. *Journal of Fluorescence* **16**, 755-759 (2006).

81 Nakazawa, E., Shionoya, S. Cooperative luminescence in $YbPO_4$. *Physical Review Letters* **25**, 1710-1712 (1970).

82 Chivian, J. S., Case, W. E., Eden, D. D. The photon avalanche: A new phenomenon in Pr^{3+}-based infrared quantum counters *Applied Physics Letters* **35**, 124-125 (1979).

83 Louis, C., Bazzi, R., Marquette, C. A., Bridot, J. L., Roux, S., Ledoux, G., Mercier, B., Blum, L., Perriat, P., Tillement, O. Nanosized Hybrid Particles with Double Luminescence for Biological Labeling. *Chemistry of Materials* **17**, 1673–1682 (2005).

84 Riwotzki, K., Haase, M. Wet-Chemical Synthesis of Doped Colloidal Nanoparticles: YVO_4:Ln (Ln = Eu, Sm, Dy). *The Journal of Physical Chemistry B* **102**, 10129–10135 (1998).

85 Zhang, Y. W., Sun, X., Si, R., You, L. P., Yan, C. H. Single-crystalline and monodisperse LaF_3 triangular nanoplates from a single-source precursor. *Journal of the American Chemistry Society* **127**, 3260–3261 (2005).

86 Peter R. Diamente, R. D. B., F. C. J. M. van Veggel. Bioconjugation of Ln^{3+}-Doped LaF_3 Nanoparticles to Avidin. *Langmiur* **22**, 1782–1788 (2005).

87 Heer, S., Kömpe, K., Güdel, H. U., Haase, M. Highly Efficient Multicolour Upconversion Emission in Transparent Colloids of Lanthanide-Doped $NaYF_4$ Nanocrystals. *Advanced Materials* **16**, 2102-2105 (2004).

88 Yi, G., Lu, H., Zhao, S., Ge, Y., Yang, W., Chen, D., Guo, L. H. Synthesis, Characterization, and Biological Application of Size-Controlled Nanocrystalline $NaYF_4$:Yb,Er Infrared-to-Visible Up-Conversion Phosphors. *Nano Letters* **4**, 2191–2196 (2004).

89 Zeng, J. H., Su, J., Li, Z. H., Yan, R. X., Li, Y. D. Synthesis and Upconversion Luminescence of Hexagonal-Phase $NaYF_4:Yb^{3+}$, Er^{3+} Phosphors of Controlled Size and Morphology. *Advanced Materials* **17**, 2119-2123 (2005).

90 Wei, Y., Lu, F., Zhang, X., Chen, D. Synthesis of Oil-Dispersible Hexagonal-Phase and Hexagonal-Shaped $NaYF_4$:Yb,Er Nanoplates. *Chemistry of Materials* **18**, 5733–5737 (2006).

91 Mai, H. X., Zhang, Y. W., Si, R., Yan, Z. G., Sun, L. D., You, L. P., Yan, C. H. High-Quality Sodium Rare-Earth Fluoride Nanocrystals: Controlled Synthesis and Optical Properties. *Journal of the American Chemistry Society* **128**, 6426–6436 (2006).

92 Jin, T., Yoshioka, Y., Fujii, F., Komai, Y., Seki, J., Seiyama, A. Gd^{3+}-functionalized near-infrared quantum dots for *in vivo* dual modal (fluorescence/magnetic resonance) imaging. *Chemical Comminucation*, 5764–5766 (2008).

93 Yang, H., Santra, S., Walter, G. A., Holloway, P. H. GdIII-Functionalized Fluorescent Quantum Dots as Multimodal Imaging Probes. *Advanced Materials* **18**, 2890-2894 (2006).

94 Mulder, W. J. M., Ricardo, R. K., Gert S., J. B., Patrick, T. K. C., Gustav, J. S., Celso, D. M. D., Klaas, N., Arjan, W. G. Quantum dots with a paramagnetic coating as a bimodal molecular imaging probe. *Nano Letters* **6**, 1-6 (2006).

95 Gerion, D., Herberg, Julie, Bok, Robert, Gjersing, Erica, Ramon, Erick, Maxwell, Robert, Kurhanewicz, John, Budinger, Thomas F., Gray, Joe W., Shuman, Marc A., Chen, Fanqing Frank. Paramagnetic silica-coated

nanocrystals as an advanced MRI contrast agent. *The Journal of Physical Chemistry C* **111**, 12542-12551, (2007).

96 Prinzen, L., Miserus, R. J. J. H. M., Dirksen, A., Hackeng, T. M., Deckers, N., Bitsch, N. J., Megens, R. T. A., Douma, K., Heemskerk, J. W., Kooi, M. E., Frederik, P. M., Slaaf, D. W., Van Zandvoort, M. A. M. J., Reutelingsperger, C. P. M. Optical and Magnetic Resonance Imaging of Cell Death and Platelet Activation Using Annexin A5-Functionalized Quantum Dots. *Nano Letters* **7**, 93-100 (2007).

97 Tsai, C. P., Hung, Y., Chou, Y. H., Huang, D. M., Hsiao, J. K., Chang, C., Chen, Y. C., Mou, C. Y. High-contrast paramagnetic fluorescent mesoporous silica nanorods as a multifunctional cell-imaging probe. *Small* **4**, 186-191 (2008).

98 Hsiao, J. K., Tsai, C. P., Chung, T. H., Hung, Y., Yao, M., Liu, H. M., Mou, C. Y., Yang, C. S., Chen, Y. C., Huang, D. M. Mesoporous Silica Nanoparticles as a Delivery System of Gadolinium for Effective Human Stem Cell Tracking. *Small* **4**, 1445–1452 (2008).

99 Taylor, K. M. L., Kim, J. S., Rieter, W. J., An, H., Lin, W. Mesoporous Silica Nanospheres as Highly Efficient MRI Contrast Agents. *Journal of the American Chemical Society* **130**, 2154-2155 (2008).

100 Rieter, W. J., Kim, J. S., Taylor, K. M. L., An, H., Lin, W., Tarrant, T. Hybrid Silica Nanoparticles for Multimodal Imaging. *Angewandte Chemie International Edition* **46**, 3680-3682 (2007).

101 Kim, J. S., Rieter, W. J., Taylor, K. M. L., An, H., Lin, W. Self-assembled hybrid nanoparticles for cancer-specific multimodal imaging. *Journal of the American Chemical Society* **129**, 8962-8963 (2007).

102 Li, I. F., Yeh, C. S. Synthesis of Gd doped CdSe nanoparticles for potential optical and MR imaging applications. *Journal of Materials Chemistry* **20**, 2079-2081 (2010).

103 Bridot, J. L., Faure, A. C., Laurent, S., Rivière, C., Billotey, C., Hiba, B., Janier, M., Josserand, V., Coll, J. L., Elst, L. V., Muller, R., Roux, S., Perriat, P., Tillement, O. Hybrid Gadolinium Oxide Nanoparticles: Multimodal

Contrast Agents for *in vivo* Imaging. *Journal of the American Chemical Society* **129**, 5076-5084 (2007).

104 Huang, C. C., Su, C. H., Li, W. M., Liu, T. Y., Chen, J. H., Yeh, C. S. Bifunctional Gd_2O_3/C nanoshells for MR imaging and NIR therapeutic applications. *Advanced Functional Materials* **19**, 249-258 (2009).

105 Miyawaki, J., Matsumura, S., Yuge, R., Murakami, T., Sato, S., Tomida, A., Tsuruo, T., Ichihashi, T., Fujinami, T., Irie, H., Tsuchida, K., Iijima, S., Shiba, K., Yudasaka, M. Biodistribution and Ultrastructural Localization of Single-Walled Carbon Nanohorns Determined In Vivo with Embedded Gd2O3 Labels. *ACS Nano* **3**, 1399–1406 (2009).

106 Petoral Jr, R. M., Söderlind, F., Klasson, A., Suska, A., Fortin, M. A., Abrikossova, N., Selegård, L., Käll, P. O., Engström, M., Uvdal, K. Synthesis and Characterization of Tb^{3+}-Doped Gd_2O_3 Nanocrystals: A Bifunctional Material with Combined Fluorescent Labeling and MRI Contrast Agent Properties. *The Journal of Physical Chemistry C* **113**, 6913-6920, doi:10.1021/jp808708m (2009).

107 Das, G. K., Heng, B. C., Ng, S. C., White, T., Loo, J. S. C., D'Silva, L., Padmanabhan, P., Bhakoo, K. K., Selvan, S. T., Tan, T. T. Y. Gadolinium oxide ultranarrow nanorods as multimodal contrast agents for optical and magnetic resonance imaging. *Langmuir* **26**, 8959-8965 (2010)

108 Setua, S., Menon, D., Asok, A., Nair, S., Koyakutty, M. Folate receptor targeted, rare-earth oxide nanocrystals for bi-modal fluorescence and magnetic imaging of cancer cells. *Biomaterials* **31**, 714-729 (2010).

109 Das, G. K., Heng, B. C., Ng, S. C., White, T., Loo, J. S. C., D'Silva, L., Padmanabhan, P., Bhakoo, K. K., Selvan, S. T., Tan, T. T. Y. Gadolinium oxide ultranarrow nanorods as multimodal contrast agents for optical and magnetic resonance imaging. *Langmuir* **26**, 8959-8965 (2010)

110 Stouwdam, J. W., Van Veggel, F. C. J. M. Near-infrared Emission of Redispersible Er^{3+}, Nd^{3+}, and Ho^{3+} Doped LaF_3 Nanoparticles. *Nano Letters* 2, 733-737 (2002).

111 Kumar, R., Nyk, M., Ohulchanskyy, T. Y., Flask, C. A., Prasad, P. N. Combined Optical and MR Bioimaging Using Rare Earth Ion Doped $NaYF_4$ Nanocrystals. *Advanced Functional Materials* **19**, 853–859 (2009).

112 Park, Y. I., Kim, J. H., Lee, K. T., Jeon, K. S., Na, H. B., Yu, J. H., Kim, H. M., Lee, N., Choi, S. H., Baik, S. I., Kim, H., Park, S. P., Park, B. J., Kim, Y. W., Lee, S. H., Yoon, S. Y., Song, I. C., Moon, W. K., Suh, Y. D., Hyeon, T. Nonblinking and nonbleaching upconverting nanoparticles as an optical imaging nanoprobe and T_1 magnetic resonance imaging contrast agent. *Advanced Materials* **21**, 4467-4471 (2009).

113 Li, Z., Zhang, Y., Shuter, B. & Muhammad Idris, N. Hybrid Lanthanide Nanoparticles with Paramagnetic Shell Coated on Upconversion Fluorescent Nanocrystals. *Langmuir* **25**, 12015–12018 (2009).

114 He, H., Xie, M. Y., Ding, Y., Yu, X. F. Synthesis of Fe_3O_4@LaF_3:Ce,Tb nanocomposites with bright fluorescence and strong magnetism. *Applied Surface Science* **255**, 4623-4626 (2009).

115 Zhang, Y., Das, G. K., Xu, R., Tan, T. T. Y. Tb-doped iron oxide: Bifunctional fluorescent and magnetic nanocrystals. *Journal of Materials Chemistry* **19**, 3696-3703 (2009).

116 Ernest, V. G., J. C. B., Christopher, P. R., Vaccaro, D. E.. Ultrasmall Mixed Ferrite Colloids as Multidimensional Magnetic Resonance Imaging, Cell Labeling, and Cell Sorting Agents. *Bioconjugate Chemistry* **18**, 1763–1771 (2007).

117 Lu, H., Yi, G., Zhao, S., Chen, D., Guo, L. H., Cheng, J. Synthesis and characterization of multi-functional nanoparticles possessing magnetic, up-conversion fluorescence and bio-affinity properties. *Journal of Materials Chemistry* **14**, 1336-1341 (2004).

118 Das, G. K., Zhang, Y., D'Silva, L., Padmanabhan, P., Heng, B. C., Chye Loo, J. S., Selvan, S. T., Bhakoo, K. K., Yang Tan, T. T. Single-Phase Dy_2O_3:Tb^{3+} Nanocrystals as Dual-Modal Contrast Agent for High Field Magnetic Resonance and Optical Imaging. *Chemistry of Materials* **23**, 2439-2446 (2011).

119 Rosenberg, J. T., Kogot, J. M., Lovingood, D. D., Strouse, G. F., Grant, S. C. Intracellular bimodal nanoparticles based on quantum dots for high-field MRI at 21.1 T. *Magnetic Resonance in Medicine* **64**, 871-882 (2010).

120 Gustafsson, B., Youens, S., Louie, A. Y. Development of contrast agents targeted to macrophage scavenger receptors for MRI of vascular inflammation. *Bioconjugate Chemistry* **17**, 538-547 (2006).

121 Alric, C., Taleb, J., Le Duc, G., Mandon, C., Billotey, C., Le Meur-Herland, A., Brochard, T., Vocanson, F., Janier, M., Perriat, P., Roux, S., Tillement, O. Gadolinium Chelate Coated Gold Nanoparticles As Contrast Agents for Both X-ray Computed Tomography and Magnetic Resonance Imaging. *Journal of the American Chemical Society* **130**, 5908-5915 (2008).

122 Sajja, H. K., East, M. P., Mao, H., Wang, Y. A., Nie, S., Yang, L. Development of multifunctional nanoparticles for targeted drug delivery and noninvasive imaging of therapeutic effect. *Current Drug Discovery Technologies* **6**, 43-51 (2009).

123 Chan, K. W. Y., Wong, W. T. Small molecular gadolinium(III) complexes as MRI contrast agents for diagnostic imaging. *Coordination Chemistry Reviews* **251**, 2428-2451 (2007).

124 Wong, H. T., Chan, H. L. W. & Hao, J. Towards pure near-infrared to near-infrared upconversion of multifunctional GdF_3:Yb^{3+},Tm^{3+} nanoparticles. *Optics Express* **18**, 6123-6130 (2010).

125 Zhang, C., Sun, L., Zhang, Y., Yan, C. Rare earth upconversion nanophosphors: Synthesis, functionalization and application as biolabels and energy transfer donors. *Journal of Rare Earths* **28**, 807-819 (2010).

126 Zielhuis, S. W., Seppenwoolde, J. H., Mateus, V. A. P., Bakker, C. J. G., Krijger, G. C., Storm, G., Zonnenberg, B. A., Van Het Schip, A. D., Koning, G. A., Nijsen, J. F. W. Lanthanide-loaded liposomes for multimodality imaging and therapy. *Cancer Biotherapy and Radiopharmaceuticals* **21**, 520-527 (2006).

127 Ong, L. C., Gnanasammandhan, M. K., Nagarajan, S., Zhang, Y. Upconversion: Road to El dorado of the fluorescence world. *Luminescence* **25**, 290-293 (2010).

128 Kostova, I. Lanthanides as anticancer agents. *Current Medicinal Chemistry - Anti-Cancer Agents* **5**, 591-602 (2005).

129 Chatterjee, D. K., Gnanasammandhan, M. K., Zhang, Y. Small upconverting fluorescent nanoparticles for biomedical applications. *Small* **6**, 2781-2795 (2010).

130 Stefanakis, D., Ghanotakis, D. F. Synthesis and characterization of gadolinium nanostructured materials with potential applications in magnetic resoance imaging, neutron-capture therapy and targeted drug delivery. *Journal of Nanoparticle Research* **12**, 1285-1297 (2010).

131 Kobayashi, H., Kawamoto, S., Bernardo, M., Brechbiel, M. W., Knopp, M. V., Choyke, P. L. Delivery of gadolinium-labeled nanoparticles to the sentinel lymph node: Comparison of the sentinel node visualization and estimations of intra-nodal gadolinium concentration by the magnetic resonance imaging. *Journal of Controlled Release* **111**, 343-351 (2006).

132 Zhang, C., Li, C., Peng, C., Chai, R., Huang, S., Yang, D., Cheng, Z., Lin, J. Facile and controllable synthesis of monodisperse CaF_2 and CaF_2:Ce^{3+}/Tb^{3+} hollow spheres as efficient luminescent materials and smart drug carriers. *Chemistry - A European Journal* **16**, 5672-5680 (2010).

133 Carling, C. J., Nourmohammadian, F., Boyer, J. C., Branda, N. R. Remote-Control Photorelease of Caged Compounds Using Near-Infrared Light and Upconverting Nanoparticles. *Angewandte Chemie International Edition* **49**, 3782 –3785 (2010).

134 Trewyn, B. G., Giri, S., Slowing, I. I., Lin, V. S. Y. Mesoporous silica nanoparticle based controlled release, drug delivery, and biosensor systems. *Chemical Communications*, 3236-3245 (2007).

135 Giri, S., Trewyn, B. G., Lin, V. S. Y. Mesoporous silica nanomaterial-based biotechnological and biomedical delivery systems. *Nanomedicine* **2**, 99-111 (2007).

136 Vivero-Escoto, J. L., Slowing, I. I., Lin, V. S. Y., Trewyn, B. G. Mesoporous silica nanoparticles for intracellular controlled drug delivery. *Small* **6**, 1952-1967 (2010).

137 Tallury, P., Payton, K., Santra, S. Silica-based multimodal/multifunctional nanoparticles for bioimaging and biosensing applications. *Nanomedicine* **3**, 579-592 (2008).

138 Yang, P., Quan, Z., Li, C., Lian, H., Huang, S., Lin, J. Fabrication, characterization of spherical $CaWO_4$:Ln @MCM-41(Ln = Eu^{3+}, Dy^{3+}, Sm^{3+}, Er^{3+}) composites and their applications as drug release systems. *Microporous and Mesoporous Materials* **116**, 524-531 (2008).

139 Huang, S., Li, C., Yang, P., Zhang, C., Cheng, Z., Fan, Y., Lin, J. Luminescent $CaWO_4$:Tb^{3+}-loaded mesoporous silica composites for the immobilization and release of lysozyme. *European Journal of Inorganic Chemistry*, 2655-2662 (2010).

140 Yang, P., Quan, Z., Lu, L., Huang, S., Lin, J., Fu, H. MCM-41 functionalized with YVO_4:Eu^{3+}: A novel drug delivery system. *Nanotechnology* **18** (2007).

141 Yang, P., Quan, Z., Lu, L., Huang, S., Lin, J. Luminescence functionalization of mesoporous silica with different morphologies and applications as drug delivery systems. *Biomaterials* **29**, 692-702 (2008).

142 Yang, P., Huang, S., Kong, D., Lin, J., Fu, H. Luminescence functionalization of SBA-15 by YVO_4:Eu^{3+} as a novel drug delivery system. *Inorganic Chemistry* **46**, 3203-3211 (2007).

143 Yang, Y., Qu, Y., Zhao, J., Zeng, Q., Ran, Y., Zhang, Q., Kong, X., Zhang, H. Fabrication of and Drug Delivery by an Upconversion Emission Nanocomposite with Monodisperse LaF_3:Yb,Er Core / Mesoporous Silica Shell Structure. *European Journal of Inorganic Chemistry*, 5195–5199 (2010).

144 Kong, D., Fan, Y., Zhang, C., Lin, J. Mesoporous silica-coated $NaYF_4$: Yb^{3+}, Er^{3+} particles for drug release. *Journal of nanoparticles Research* **12**, 663-673 (2010).

145 Yang, P., Quan, Z., Hou, Z., Li, C., Kang, X., Cheng, Z., Lin, J. A magnetic, luminescent and mesoporous core-shell structured composite material as drug carrier. *Biomaterials* **30**, 4786-4795 (2009).

146 Gai, S., Yang, P., Li, C., Wang, W., Dai, Y., Niu, N., Lin, J. Synthesis of magnetic, up-conversion luminescent, and mesoporous core-shell-structured nanocomposites as drug carriers. *Advanced Functional Materials* **20**, 1166-1172 (2010).

147 Baughman, R. H., Zakhidov, A. A. & de Heer, W. A. Carbon nanotubes - the route toward applications. *Science* **297**, 787-792 (2002).

148 Tasis, D., Tagmatarchis, N., Bianco, A., Prato, M. Chemistry of carbon nanotubes. *Chemical Reviews* **106**, 1105-1136, doi:10.1021/cr050569o (2006).

149 Lin, Y., Taylor, S., Li, H. P., Fernando, K. A. S., Qu, L. W., Wang, W., Gu, L. R., Zhou, B., Sun, Y. P. Advances toward bioapplications of carbon nanotubes. *Journal of Materials Chemistry* **14**, 527-541, doi:10.1039/b314481j (2004).

150 Shi, D., Lian, J., Wang, W., Liu, G., He, P., Dong, Z., Wang, L., Ewing, R. C. Luminescent Carbon Nanotubes by Surface Functionalization. *Advanced Materials* **18**, 189-193 (2006).

151 Fan, Y., Yang, P., Huang, S., Jiang, J., Lian, H., Lin, J. Luminescent and mesoporous europium-doped bioactive glasses (MBG) as a drug carrier. *Journal of Physical Chemistry C* **113**, 7826-7830 (2009).

152 Yang, P., Quan, Z., Li, C., Kang, X., Lian, H., Lin, J. Bioactive, luminescent and mesoporous europium-doped hydroxyapatite as a drug carrier. *Biomaterials* **29**, 4341-4347 (2008).

153 Zhang, C., Li, C., Huang, S., Hou, Z., Cheng, Z., Yang, P., Peng, C., Lin, J. Self-activated luminescent and mesoporous strontium hydroxyapatite nanorods for drug delivery. *Biomaterials* **31**, 3374-3383 (2010).

154 Swetha, M., Sahithi, K., Moorthi, A., Srinivasan, N., Ramasamy, K., Selvamurugan, N. Biocomposites containing natural polymers and hydroxyapatite for bone tissue engineering. *International Journal of Biological Macromolecules* **47**, 1-4 (2010).

155 Nagarwal, R. C., Kant, S., Singh, P. N., Maiti, P., Pandit, J. K. Polymeric nanoparticulate system: A potential approach for ocular drug delivery. *Journal of Controlled Release* **136**, 2-13 (2009).

156 Kumari, A., Yadav, S. K. & Yadav, S. C. Biodegradable polymeric nanoparticles based drug delivery systems. *Colloids and Surfaces B: Biointerfaces* **75**, 1-18 (2010).

157 Tjong, S. C. Structural and mechanical properties of polymer nanocomposites. *Materials Science and Engineering R: Reports* **53**, 73-197 (2006).

158 Rieter, W. J., Pott, K. M., Taylor, K. M. L., Lin, W. Nanoscale Coordination Polymers for Platinum-Based Anticancer Drug Delivery. *Journal of the American Chemical Society* **130**, 11584–11585 (2008).

159 Wang, C., Cheng, L., Liu, Z. Drug delivery with upconversion nanoparticles for multi-functional targeted cancer cell imaging and therapy. *Biomaterials* **32**, 1110-1120 (2011).

160 Bechet, D., Couleaud, P., Frochot, C., Viriot, M. L., Guillemin, F., Barberi-Heyob, M. Nanoparticles as vehicles for delivery of photodynamic therapy agents. *Trends in Biotechnology* **26**, 612-621 (2008).

161 Chatterjee, D. K., Fong, L. S., Zhang, Y. Nanoparticles in photodynamic therapy: An emerging paradigm. *Advanced Drug Delivery Reviews* **60**, 1627-1637 (2008).

162 Zhang, P., Steelant, W., Kumar, M., Scholfield, M. Versatile Photosensitizers for Photodynamic Therapy at Infrared Excitation. *Journal of the American Chemical Society* **129**, 4526-4527 (2007).

163 Guo, Y., Kumar, M., Zhang, P. Nanoparticle-Based Photosensitizers under CW Infrared Excitation. *Chemistry of Materials* **19**, 6071–6072 (2007).

164 Chatterjee, D. K., Yong, Z. Upconverting nanoparticles as nanotransducers for photodynamic therapy in cancer cells. *Nanomedicine* **3**, 73-82 (2010).

165 Qian, H. S., Guo, H. C., Ho, P. C. L., Mahendran, R., Zhang, Y. Mesoporous-silica-coated up-conversion fluorescent nanoparticles for photodynamic therapy. *Small* **5**, 2285-2290 (2009).

166 Guo, H., Qian, H., Idris, N. M. & Zhang, Y. Singlet oxygen-induced apoptosis of cancer cells using upconversion fluorescent nanoparticles as a carrier of photosensitizer. *Nanomedicine* **6**, 486–495 (2010).

167 Davis, M. E. The first targeted delivery of siRNA in humans via a self-assembling, cyclodextrin polymer-based nanoparticle: From concept to clinic. *Molecular Pharmaceutics* **6**, 659-668 (2009).

168 Jiang, S., Zhang, Y., Lim, K. M., Sim, E. K. W., Ye, L. NIR-to-visible upconversion nanoparticles for fluorescent labeling and targeted delivery of siRNA. *Nanotechnology* **20** (2009).

169 Jiang, S., Zhang, Y. Upconversion nanoparticle-based FRET system for study of siRNA in live cells. *Langmuir* **26**, 6689-6694 (2010).

170 Kenny, G. D., Kamaly, N., Kalber, T. L., Brody, L. P., Sahuri, M., Shamsaei, E., Miller, A. D., Bell, J. D. Novel multifunctional nanoparticle mediates siRNA tumour delivery, visualisation and therapeutic tumour reduction *in vivo*. *Journal of Controlled Release* **149**, 111–116 (2011).

171 Li, C., Penet, M. F., Wildes, F., Takagi, T., Chen, Z., Winnard, P. T., Artemov, D., Bhujwalla, Z. M. Nanoplex Delivery of siRNA and Prodrug Enzyme for Multimodality Image Guided Molecular Pathway Targeted Cancer Therapy. *ACS Nano* **4**, 6707–6716 (2010).

172 Rüttinger, D., Vollmar, B., Wanner, G. A., Messmer, K. *In vivo* assessment of hepatic alterations following gadolinium chloride-induced Kupffer cell blockade. *Journal of Hepatology* **25**, 960-967 (1996).

173 Roland, C. R., Naziruddin, B., Mohanakumar, T. & Wayne Flye, M. Gadolinium blocks rat kupffer cell calcium channels: Relevance to calcium-dependent prostaglandin E2 synthesis and septic mortality. *Hepatology* **29**, 756-765 (1999).

174 Lee, C. M., Yeoh, G. C., Olynyk, J. K. Differential effects of gadolinium chloride on Kupffer cells *in vivo* and *in vitro*. *The International Journal of Biochemistry & Cell Biology* **36**, 481-488 (2004).

175 Mizgerd, J. P., Molina, R. M., Stearns, R. C., Brain, J. D., Warner, A. E. Gadolinium induces macrophage apoptosis. *Journal of Leukocyte Biology* **59**, 189-195 (1996).

176 Epstein, H., Berger, V., Levi, I., Eisenberg, G., Koroukhov, N., Gao, J., Golomb, G. Nanosuspensions of alendronate with gallium or gadolinium attenuate neointimal hyperplasia in rats. *Journal of Controlled Release* **117**, 322-332 (2007).

177 Chen, J., Patil, S., Seal, S., McGinnis, J. F. Rare earth nanoparticles prevent retinal degeneration induced by intracellular peroxides. *Nature Nanotechnology* **1**, 142-150 (2006).

178 Man, N., Yu, L., Yu, S. H., Wen, L. P. Rare earth oxide nanocrystals as a new class of autophagy inducers. *Autophagy* **6**, 310-311 (2010).

179 Jun, Y. W., Choi, J. S., Cheon, J. Shape control of semiconductor and metal oxide nanocrystals through nonhydrolytic colloidal routes. *Angewandte Chemie - International Edition* **45**, 3414-3439 (2006).

180 Tao, A. R., Habas, S., Yang, P. Shape control of colloidal metal nanocrystals. *Small* **4**, 310-325 (2008).

181 Xia, Y., Xiong, Y., Lim, B., Skrabalak, S. E. Shape-controlled synthesis of metal nanocrystals: Simple chemistry meets complex physics. *Angewandte Chemie - International Edition* **48**, 60-103 (2009).

182 Yi, G. S., Chow, G. M. Synthesis of hexagonal-phase $NaYF_4$:Yb,Er and NaYF 4:Yb,Tm nanocrystals with efficient up-conversion fluorescence. *Advanced Functional Materials* **16**, 2324-2329 (2006).

183 Chen, Z., Chen, H., Hu, H., Yu, M., Li, F., Zhang, Q., Zhou, Z., Yi, T., Huang, C. Versatile synthesis strategy for carboxylic acid-functionalized upconverting nanophosphors as biological labels. *Journal of the American Chemical Society* **130**, 3023-3029 (2008).

184 Hu, H., Yu, M., Li, F., Chen, Z., Gao, X., Xiong, L., Huang, C. Facile epoxidation strategy for producing amphiphilic up-converting rare-earth

nanophosphors as biological labels. *Chemistry of Materials* **20**, 7003-7009 (2008).

185 Yi, G. S., Chow, G. M. Water-soluble $NaYF_4$:Yb,Er(Tm)/$NaYF_4$/polymer core/shell/shell nanoparticles with significant enhancement of upconversion fluorescence. *Chemistry of Materials* **19**, 341-343 (2007).

186 Wang, L., Yan, R., Huo, Z., Zeng, J., Bao, J., Wang, X., Peng, Q., Li, Y. Fluorescence resonant energy transfer biosensor based on upconversion-luminescent nanoparticles. *Angewandte Chemie - International Edition* **44**, 6054-6057 (2005).

187 Stöber, W., Fink, A., Bohn, E. Controlled growth of monodisperse silica spheres in the micron size range. *Journal of Colloid and Interface Science* **26**, 62-69 (1968).

188 Burns, A., Ow, H., Wiesner, U. Fluorescent core-shell silica nanoparticles: Towards "lab on a particle" architectures for nanobiotechnology. *Chemical Society Reviews* **35**, 1028-1042 (2006).

189 Li, Z., Zhang, Y. Monodisperse silica-coated polyvinyl-pyrrolidone/NaYF4 nanocrystals with multicolor upconversion fluorescence emission. *Angewandte Chemie - International Edition* **45**, 7732-7735 (2006).

190 Selvan, S. T., Patra, P. K., Ang, C. Y., Ying, J. Y. Synthesis of silica-coated semiconductor and magnetic quantum dots and their use in the imaging of live cells. *Angewandte Chemie - International Edition* **46**, 2448-2452 (2007).

191 Qian, H. S., Zhang, Y. Synthesis of hexagonal-phase core-shell $NaYF_4$ nanocrystals with tunable upconversion fluorescence. *Langmuir* **24**, 12123-12125 (2008).

192 Selvan, S. T., Patra, P. K., Ang, C. Y., Ying, J. Y. Synthesis of silica-coated semiconductor and magnetic quantum dots and their use in the imaging of live cells. *Angewandte Chemie - International Edition* **46**, 2448-2452 (2007).

193 *http://en.wikipedia.org/wiki/Bragg%27s_law*.

194 *http://en.wikipedia.org/wiki/X-ray_photoelectron_spectroscopy*.

195 Lee, S. C., Jerry S. H., Zhang, M., Magnetic nanoparticles in MR imaging and drug delivery. *Advanced Drug Delivery Reviews* **60**, 1252-1265 (2008).

196 Li, C., Wang, F., Zhu, J., Yu, J. C. $NaYF_4$:Yb,Tm/CdS composite as a novel near-infrared-driven photocatalyst. *Applied Catalysis B: Environmental* **100**, 433-439 (2010).

197 Ungun, B., Prud'homme, R. K., Budijono, S. J., Shan, J., Lim, S. F., Ju, Y., Austin, R. Nanofabricated upconversion nanoparticles for photodynamic therapy. *Optics Express* **17**, 80-86 (2009).

198 Mulder, W. J. M., Griffioen, A. W., Strijkers, G. J., Cormode, D. P., Nicolay, K., Fayad, Z. A. Magnetic and fluorescent nanoparticles for multimodality imaging. *Nanomedicine* **2**, 307-324 (2007).

199 Mialon, G., Gohin, M., Gacoin, T., Boilot, J. P. High temperature strategy for oxide nanoparticle synthesis. *ACS Nano* **2**, 2505-2512 (2008).

200 Heer, S., Lehmann, O., Haase, M., Güdel, H. U. Blue, green, and red upconversion emission from lanthanide-doped $LuPO_4$ and $YbPO_4$ nanocrystals in a transparent colloidal solution. *Angewandte Chemie - International Edition* **42**, 3179-3182 (2003).

201 Meiser, F., Cortez, C., Caruso, F. Biofunctionalization of fluorescent rare-earth-doped lanthanum phosphate colloidal nanoparticles. *Angewandte Chemie - International Edition* **43**, 5954-5957 (2004).

202 Wang, F., Liu, X. Upconversion multicolor fine-tuning: Visible to near-infrared emission from lanthanide-doped $NaYF_4$ nanoparticles. *Journal of the American Chemical Society* **130**, 5642-5643 (2008).

203 Niu, W., Wu, S., Zhang, S., Li, L. Synthesis of colour tunable lanthanide-ion doped $NaYF_4$ upconversion nanoparticles by controlling temperature. *Chemical Communications* **46**, 3908-3910 (2010).

204 Li, Z., Zhang, Y., Jiang, S. Multicolor core/shell-structured upconversion fluorescent nanoparticles. *Advanced Materials* **20**, 4765-4769 (2008).

205 Norek, M., Kampert, E., Zeitler, U., Peters, J. A. Tuning of the size of Dy_2O_3 nanoparticles for optimal performance as an MRI contrast agent. *Journal of the American Chemical Society* **130**, 5335-5340 (2008).

206 Vander, E. L., Roch, A., Gillis, P., Laurent, S., Botteman, F., Bulte, J. W. M., Muller, R. N. Dy-DTPA derivatives as relaxation agents for very high field MRI: The beneficial effect of slow water exchange on the transverse relaxivities. *Magnetic Resonance in Medicine* **47**, 1121-1130 (2002).

207 Yasuo, S., Yoshitaka, F. Effect of Dy^{3+} on the luminescence of Y_3OCL_7: Yb^{3+}, Er^{3+}. *Japanese Journal of Applied Physics* **10**, 891-901 (1971).

208 Ohwaki, J., Wang, Y. 1.3 um to visible upconversion in Dy^{3+}-and Er^{3+}-codoped $BaCl_2$ phosphor. *Applied Physics Letters* **65**, 129-131 (1994).

209 Tkachuk, A., Ivanova, S., Isaenko, L., Yelisseyev, A., Krupke, W., Payne, S., Solarz, R., Nostrand, M., Page, R., Payne, S. Spectrospcopic study of Dy^{3+} and Yb^{3+} doped double chloride and double fluoride crystals for telecommunication amplifers and IR lasers. *Part of the 18th congress of the international commision for optics: Opticas for the next millennium San Francisco, SPIE*, 660-661 (1999).

210 Vetrone, F., Naccache, R., Mahalingam, V., Morgan, C. G.,Capobianco, J. A. The active-core/active-shell approach: a strategy to enhance the upconversion luminescence in lanthanide-doped nanoparticles. *Advanced Functional Materials* **19**, 1-6 (2009).

211 Jiang, D., Cao, L., Su, G., Liu, W., Qu, H., Sun, Y., Dong, B. Synthesis and luminescence properties of ZnS: Mn/ZnS core/shell nanorod structures. *Journal of Materials Science-Materials in Electronics* **44**, 2792-2795 (2009).

212 Kömpe, K., Borchert, H., Storz, J., Lobo, A., Adam, S., Möller, T., Haase, M. Green-Emitting $CePO_4$:Tb/$LaPO_4$ Core-Shell Nanoparticles with 70 % Photoluminescence Quantum Yield. *Angewandte Chemie-International Edition* **42**, 5513-5516 (2003).

213 Vetrone, F., Naccache, R., Mahalingam, V., Morgan, C. G.,Capobianco, J. A. The active-core/active-shell approach: A strategy to enhance the upconversion luminescence in lanthanide-doped nanoparticles. *Advanced Functional Materials* **19**, 2924-2929 (2009).

214 Abdul, J. R., Zhang, Y. Biocompatibility of silica coated NaYF4 upconversion fluorescent nanocrystals. *Biomaterials* **29**, 4122-4128 (2008).

215 Na, H. B., Song, I. C., Hyeon, T. Inorganic Nanoparticles for MRI Contrast Agents. *Advanced Materials* **21**, 2133-2148 (2009).

216 Kim, J., Piao, Y., Hyeon, T. Multifunctional nanostructured materials for multimodal imaging, and simultaneous imaging and therapy. *Chemical Society Review* **38**, 372-390 (2009).

217 Louie, A. Multimodality Imaging Probes: Design and Challenges. *Chemical Review* **110**, 3146-3195 (2010).

218 Nahrendorf, M., Sosnovik, D., Weissleder, R. MR-optical imaging of cardiovascular molecular targets. *Basic Research in Cardiology* **103**, 87-94, (2008).

219 Frullano, L., Meade, T. J. Multimodal MRI contrast agents. *Journal of Biological Inorganic Chemistry* **12**, 939-949 (2007).

220 Basilion, J. P., Yeon, S., Botnar, R. Magnetic Resonance Imaging: Utility as a Molecular Imaging Modality. *Current Topics in Development Biology* **70**, 1-33 (2005).

221 Hermann, P., Kotek, J., Kubicek, V., Lukes, I. Gadolinium(iii) complexes as MRI contrast agents: ligand design and properties of the complexes. *Dalton Transactions*, 3027-3047 (2008).

222 Bl é, F. X., Schmidt, P., Cannet, C., Kneuer, R., Karmouty-Quintana, H., Bergmann, R., Coote, K., Danahay, H., Zurbruegg, S., Gremlich, H. U., Beckmann, N. In vivo assessments of mucus dynamics in the rat lung using a Gd-Cy5.5-bilabeled contrast agent for magnetic resonance and optical imaging. *Magnnetic Resonance in Medicine* **62**, 1164-1174 (2009).

223 Li, Z., Zhang, Y., Shuter, B., Muhammad Idris, N. Hybrid Lanthanide Nanoparticles with Paramagnetic Shell Coated on Upconversion Fluorescent Nanocrystals. *Langmuir* **25**, 12015-12018 (2009).

224 Wang, D., He, J., Rosenzweig, N., Rosenzweig, Z. Superparamagnetic Fe_2O_3 Beads−CdSe/ZnS Quantum Dots Core−Shell Nanocomposite Particles for Cell Separation. *Nano Lett.* **4**, 409-413 (2004).

225 Huang, C. C., Su, C. H., Li, W. M., Liu, T. Y., Chen, J. H., Yeh, C. S. Bifunctional Gd_2O_3/C Nanoshells for MR Imaging and NIR Therapeutic Applications. *Advanced Functional Materials* **19**, 249-258 (2009).

226 Wang, F., Tan, W. B., Zhang, Y., Fan, X., Wang, M. Luminescent nanomaterials for biological labelling. *Nanotechnology* **17**, R1-R13 (2006).

227 Lauffer, R. B. Paramagnetic metal complexes as water proton relaxation agents for NMR imaging: theory and design. *Chemical Reviews* **87**, 901-927, (1987).

228 Bottrill, M., Kwok, L., Long, N. J. Lanthanides in magnetic resonance imaging. *Chemical Society Reviews* **35**, 557-571 (2006).

229 Bae, K. H., Kim, Y. B., Lee, Y., Hwang, J. Y., Park, H., Park, T. G. Bioinspired synthesis and characterization of gadolinium-labeled magnetite nanoparticles for dual contrast T_1- and T_2-weighted magnetic resonance imaging. *Bioconjugate Chemistry* **21**, 505-512 (2010).

230 Choi, J. S., Lee, J. H., Shin, T. H., Song, H. T., Kim, E. Y., Cheon, J. Self-confirming "aND" logic nanoparticles for fault-free MRI. *Journal of the American Chemical Society* **132**, 11015-11017 (2010).

231 Corot, C., Robert, P., Idée, J. M., Port, M. Recent advances in iron oxide nanocrystal technology for medical imaging. *Advanced Drug Delivery Reviews* **58**, 1471-1504 (2006).

232 Seo, W. S., Lee, J. H., Sun, X., Suzuki, Y., Mann, D., Liu, Z., Terashima, M., Yang, P. C., McConnell, M. V., Nishimura, D. G., Dai, H. FeCo/graphitic-shell nanocrystals as advanced magnetic-resonance-imaging and near-infrared agents. *Nature Materials* **5**, 971-976 (2006).

233 Ralph A, H. Multiphoton excitation and efficiency in the Yb^{3+}-R.E.$^{3+}$ (Ho^{3+}, Er^{3+}, Tm^{3+}) systems. *Journal of Luminesence* **1-2**, 778-796 (1970).

234 Boyer, J. C., Vetrone, F., Capobianco, J. A., Speghini, A., Bettinelli, M., Yb^{3+} ion as a sensitizer for the upconversion luminescence in nanocrystalline $Gd_3Ga_5O_{12}$:Ho_3 þ. *Chemical Physics Letters* **390**, 403-407 (2004).

235 Boyer, J. C., Gagnon, J., Cuccia, L. A. & Capobianco, J. A. Synthesis, Characterization, and Spectroscopy of $NaGdF_4$: Ce^{3+}, Tb^{3+}/$NaYF_4$ Core/Shell Nanoparticles. *Chemistry of Materials* **19**, 3358-3360 (2007).

236 Li Z., Zhang, Y., Jiang, S. Multicolor core/shell-structured upconversion fluorescent nanoparticles. *Advanced Materials* **20**, 4765-4769 (2008).

237 Mai, H. X., Zhang, Y. W., Si, R., Yan, Z. G., Sun, L. D., You, L. P., Yan, C. H. High-Quality Sodium Rare-Earth Fluoride Nanocrystals: Controlled Synthesis and Optical Properties. *Journal of the American Chemical Society* **128**, 6426-6436 (2006).

238 Boyer, J. C., Cuccia, L. A., Capobianco, J. A. Synthesis of colloidal upconverting $NaYF_4$: Er^{3+}/Yb^{3+} and Tm^{3+}/Yb^{3+} monodisperse nanocrystals. *Nano Letters* **7**, 847-852 (2007).

239 Boyer, J. C., Vetrone, F., Cuccia, L. A., Capobianco, J. A. Synthesis of colloidal upconverting $NaYF_4$ nanocrystals doped with Er^{3+}, Yb^{3+} and Tm^{3+}, Yb^{3+} via thermal decomposition of lanthanide trifluoroacetate precursors. *Journal of American Chemical Society* **128**, 7444-7445 (2006).

240 Yasuo S., Yoshitaka F. Effect of Dy^{3+} on the luminescence of Y_3OCL_7: Yb^{3+}, Er^{3+}. *Japanese Journal of Applied Physics* **10**, 891-901 (1971).

241 Wang, F., Liu, X. Recent advances in the chemistry of lanthanide-doped upconversion nanocrystals. *Chemical Society Reviews* **38**, 976-989 (2009).

242 Fan, H., Leve, E. W., Scullin, C., Gabaldon, J., Tallant, D., Bunge, S., Boyle, T., Wilson, M. C., Brinker, C. J. Surfactant-Assisted Synthesis of Water-Soluble and Biocompatible Semiconductor Quantum Dot Micelles. *Nano Letters* **5**, 645-648 (2005).

243 Viswanathan, S., Kovacs, Z., Green, K. N., Ratnakar, S. J., Sherry, A. D. Alternatives to Gadolinium-Based Metal Chelates for Magnetic Resonance Imaging. *Chemical Reviews* **110**, 2960-3018 (2010).

244 Vander Elst, L., Roch, A., Gillis, P., Laurent, S., Botteman, F., Bulte, J. W. M., Muller, R. N. Dy-DTPA derivatives as relaxation agents for very high field MRI: The beneficial effect of slow water exchange on the transverse relaxivities. *Magnetic Resonance in Medecine.* **47**, 1121-1130 (2002).

245 Norek, M., Kampert, E., Zeitler, U., Peters, J. A. Tuning of the size of Dy_2O_3 nanoparticles for optimal performance as an MRI contrast agent. *Journal of American Chemical Society* **130**, 5335-5340 (2008).

246 Das, G. K., Zhang, Y., D'Silva, L., Padmanabhan, P., Heng, B. C., Chye Loo, J. S., Selvan, S. T., Bhakoo, K. K., Yang Tan, T. T. Single-phase Dy_2O_3:Tb^{3+} nanocrystals as dual-modal contrast agent for high field magnetic resonance and optical imaging. *Chemistry of Materials* **23**, 2439-2446 (2011).

247 Norek, M., Peters, J. A. MRI contrast agents based on dysprosium or holmium. *Progress in Nuclear Magnetic Resonance Spectroscopy* **59**, 64-82 (2011).

248 Caravan, P. Strategies for increasing the sensitivity of gadolinium based MRI contrast agents. *Chemical Society Reviews* **35**, 512-523 (2006).

249 Caravan, P., Ellison, J. J., McMurry, T. J., Lauffer, R. B. Gadolinium(III) chelates as MRI contrast agents: Structure, dynamics, and applications. *Chemical Reviews* **99**, 2293-2352 (1999).

250 Helm, L. Optimization of gadolinium-based MRI contrast agents for high magnetic-field applications. *Future Medicinal Chemistry* **2**, 385-396 (2010).

251 Bridot, J. L., Faure, A. C., Laurent, S., Rivière, C., Billotey, C., Hiba, B., Janier, M., Josserand, V., Coll, J. L., Elst, L. V., Muller, R., Roux, S., Perriat, P., Tillement, O. Hybrid Gadolinium Oxide Nanoparticles: Multimodal Contrast Agents for *in vivo* Imaging. *Journal of American Chemical Society* **129**, 5076-5084 (2007).

252 Das, G. K., Heng, B. C., Ng, S. C., White, T., Loo, J. S. C., D'Silva, L., Padmanabhan, P., Bhakoo, K. K., Selvan, S. T., Tan, T. T. Y. Gadolinium Oxide Ultranarrow Nanorods as Multimodal Contrast Agents for Optical and Magnetic Resonance Imaging. *Langmuir* **26**, 8959-8965, (2010).

253 Evanics, F., Diamente, P. R., van Veggel, F. C. J. M., Stanisz, G. J., Prosser, R. S. Water-Soluble GdF_3 and GdF_3/LaF_3 NanoparticlesPhysical Characterization and NMR Relaxation Properties. *Chemistry of Materials* **18**, 2499-2505, (2006).

254 Gossuin, Y., Hocq, A., Vuong, Q. L., Disch, S., Hermann, R. P., Gillis, P. Physico-chemical and NMR relaxometric characterization of gadolinium hydroxide and dysprosium oxide nanoparticles. *Nanotechnology* **19**, 475102 (2008).

255 Jun, Y. W., Lee, J. H., Cheon, J. Chemical Design of Nanoparticle Probes for High-Performance Magnetic Resonance Imaging. *Angewandte Chemie Internation Edition* **47**, 5122-5135 (2008).

256 Gong, J., Zhao, H., Liu, T., Ling, R., Xu, J. Value of MRCP using oral Gd-DTPA as negative contrast materials in diagnosis of atypical juxtapapillary duodenal diverticulum. *Clinical Imaging* **33**, 361-364 (2009).

257 Kim, J., Piao, Y. & Hyeon, T. Multifunctional nanostructured materials for multimodal imaging and simultaneous imaging and therapy. *Chemical Society Reviews* **38**, 372-390 (2009).

258 Medintz, I. L., Uyeda, H. T., Goldman, E. R., Mattoussi, H. Quantum dot bioconjugates for imaging, labelling and sensing. *Nature Materials* **4**, 435-446, (2005).

259 Michalet, X., Pinaud, F. F., Bentolila, L. A., Tsay, J. M., Doose, S., Li, J. J., Sundaresan, G., Wu, A. M., Gambhir, S. S., Weiss, S. Quantum dots for live cells, in vivo imaging, and diagnostics *Science* **307** 538-544 (2005).

260 Shang, L., Yin, J., Li, J., Jin, L., Dong, S. Gold nanoparticle-based near-infrared fluorescent detection of biological thiols in human plasma. *Biosensors and Bioelectronics* **25**, 269-274 (2009).

261 Guo, R., Zhang, L., Qian, H., Li, R., Jiang, X., Liu, B. Multifunctional nanocarriers for cell imaging, drug delivery, and near-IR photothermal therapy. *Langmuir* **26**, 5428-5434 (2010).

262 Wu, X., He, X., Wang, K., Xie, C., Zhou, B., Qing, Z. Ultrasmall near-infrared gold nanoclusters for tumor fluorescence imaging in vivo. *Nanoscale* **2**, 2244-2249 (2010).

263 Welsher, K., Liu, Z., Daranciang, D., Dai, H. Selective probing and imaging of cells with single walled carbon nanotubes as near-infrared fluorescent molecules. *Nano Letters* **8**, 586-590 (2008).

264 Kim, J. H., Heller, D. A., Jin, H., Barone, P. W., Song, C., Zhang, J., Trudel, L. J., Wogan, G. N., Tannenbaum, S. R., Strano, M. S. The rational design of nitric oxide selectivity in single-walled carbon nanotube near-infrared fluorescence sensors for biological detection. *Nature Chemistry* **1**, 473-481 (2009).

265 He, X., Chen, J., Wang, K., Qin, D., Tan, W. Preparation of luminescent Cy5 doped core-shell SFNPs and its application as a near-infrared fluorescent marker. *Talanta* **72**, 1519-1526 (2007).

266 Lee, C. H., Cheng, S. H., Wang, Y. J., Chen, Y. C., Chen, N. T., Souris, J., Chen, C. T., Mou, C. Y., Yang, C. S., Lo, L. W. Near-infrared mesoporous silica nanoparticles for optical imaging: Characterization and in vivo biodistribution. *Advanced Functional Materials* **19**, 215-222 (2009).

267 Santra, S., Wang, K., Tapec, R., Tan, W. Development of novel dye-doped silica nanoparticles for biomarker application. *Journal of Biomedical Optics* **6**, 160-166 (2001).

268 Chou, P. T., Chen, C. Y., Cheng, C. T., Pu, S. C. , Wu, K. C., Cheng, Y. M., Lai, C. W., Chou, Y. H., Chiu, H. T.. Spectroscopy and femtosecond dynamics of type-II CdTe/CdSe core–shell quantum dots. *ChemPhysChem* **7**, 222-228, (2006).

269 Chen, W., Joly, A. G., McCready, D. E. Upconversion luminescence from CdSe nanoparticles. *Journal of Chemical Physics* **122**, 1-7 (2005).

270 Allen, P. M., Bawendi, M. G. Ternary I−III−VI Quantum Dots Luminescent in the Red to Near-Infrared. *Journal of the American Chemical Society* **130**, 9240-9241 (2008).

271 Ferńe, M. J., Jensen, P., Rubinsztein-Dunlop, H. Unconventional photoluminescence upconversion from PbS quantum dots. *Applied Physics Letters* **91** (2007).

272 Jakubek, Z. J., DeVries, J., Lin, S., Ripmeester, J., Yu, K. Exciton recombination and unconverted photoluminescence in colloidal CdSe quantum dots. *Journal of Physical Chemistry C* **112**, 8153-8158 (2008).

273 Kim, S. W., Zimmer, J, P., Ohnishi, S,, Tracy, J, B., Frangioni, J, V., Bawendi, M, G. Engineering InAsxP1-x/InP/ZnSe III−V Alloyed Core/Shell Quantum Dots for the Near-Infrared. *Journal of the American Chemical Society* **127**, 10526-10532 (2005).

274 Li, X., Liu, B., Li, Z., Li, Q., Zou, Y., Liu, D., Li, D., Zou, B., Cui, T., Zou, G. Photoluminescence up-conversion of CdSe/ZnS core/shell quantum dots under high pressure. *Journal of Physical Chemistry C* **113**, 4737-4740 (2009).

275 Nguyen, T. L., Spizzirri, P., Wilson, G., Mulvaney, P. Tunable light emission using quantum dot-coated upconverters. *Chemical Communications*, 174-176 (2008).

276 Ouyang, J., Ripmeester, J. A., Wu, X., Kingston, D., Yu, K., Joly, A. G., Chen, W. Upconversion luminescence of colloidal CdS and ZnCdS semiconductor quantum dots. *Journal of Physical Chemistry C* **111**, 16261-16266 (2007).

277 Wang, X., Yu, W. W., Zhang, J., Aldana, J., Peng, X., Xiao, M. Photoluminescence upconversion in colloidal CdTe quantum dots. *Physical Review B* **68**, 125318 (2003).

278 Yan, C., Dadvand, A., Rosei, F., Perepichka, D. F. Near-IR photoresponse in new up-converting CdSe/$NaYF_4$:Yb,Er nanoheterostructures. *Journal of the American Chemical Society* **132**, 8868-8869 (2010).

279 Reich, G. Near-infrared spectroscopy and imaging: Basic principles and pharmaceutical applications. *Advanced Drug Delivery Reviews* **57**, 1109-1143, (2005).

280 Ntziachristos, V., Bremer, C., Weissleder, R. Fluorescence imaging with near-infrared light: New technological advances that enable in vivo molecular imaging. *European Radiology* **13**, 195-208 (2003).

281 Chen, W., Joly, A. G., McCready, D. E. Upconversion luminescence from CdSe nanoparticles. *The Journal of chemical physics* **122**, 224708 (2005).

282 Joly, A. G., Chen, W., McCready, D. E., Malm, J. O., Bovin, J. O. Upconversion luminescence of CdTe nanoparticles. *Physical Review B - Condensed Matter and Materials Physics* **71**, 1-9 (2005).

283 Wang, J., Lin, M., Yan, Y., Wang, Z., Ho, P. C., Kian, P. L. CdSe/AsS core-shell quantum dots: Preparation and two-photon fluorescence. *Journal of the American Chemical Society* **131**, 11300-11301 (2009).

284 Valakh, M. Y., Korsunska, N. O., Sadofyev, Yu G., Strelchuk, V. V., Semenova, G. N., Borkovska, L. V., Artamonov, V. V., Vuychik, M. V. Anti-Stokes photoluminescence and structural defects in CdSe/ZnSe nanostructures. *Materials Science and Engineering B* **101**, 255-258 (2003).

285 Poles, E., Selmarten, D. C., Mićić, O. I., Nozik, A. J. Anti-Stokes photoluminescence in colloidal semiconductor quantum dots. *Applied Physics Letters* **75**, 971-973 (1999).

286 Joly, A. G., Chen, W., Roark, J., Zhang, J. Z. Temperature dependence of up-conversion luminescence and photoluminescence of $Mn^{2+<}$ in ZnS:Mn^{2+} nanoparticles. *Journal of Nanoscience and Nanotechnology* **1**, 295-301 (2001).

287 Driessen, F. A. J. M. High-efficiency energy up-conversion at GaAs-$GaInP_2$ interfaces. *Applied Physics Letters* **67**, 2813 (1995).

288 Su, Z. P., Teon, K. L., Yu, P. Y., Uchida, K. Mechanisms of photoluminescence upconversion at the GaAs/ordered $GaLnP_2$ interface. *Solid State Communications* **99**, 933-936 (1996).

289 Bünzli, J. C. G., Piguet, C. Taking advantage of luminescent lanthanide ions. *Chemical Society Reviews* **34**, 1048-1077 (2005).

290 Li, Z., Zhang, Y., Jiang, S. Multicolor core/shell-structured upconversion fluorescent nanoparticles. *Advanced Materials* **20**, 4765-4769 (2008).

291 Yi, G. S., Chow, G. M. Colloidal LaF_3:Yb,Er, LaF_3:Yb,Ho and LaF_3:Yb,Tm nanocrystals with multicolor upconversion fluorescence. *Journal of Materials Chemistry* **15**, 4460-4464 (2005).

292 Yin, A., Zhang, Y., Sun, L., Yan, C. Colloidal synthesis and blue based multicolor upconversion emissions of size and composition controlled monodisperse hexagonal $NaYF_4$: Yb,Tm nanocrystals. *Nanoscale* **2**, 953-959 (2010).

293 Wang, F., Liu, X. Upconversion Multicolor Fine-Tuning: Visible to Near-Infrared Emission from Lanthanide-Doped $NaYF_4$ Nanoparticles. *Journal of the American Chemical Society* **130**, 5642-5643, doi:10.1021/ja800868a (2008).

294 Bednarkiewicz, A., Nyk, M., Samoc, M., Strek, W. Up-conversion FRET from Er^{3+}/Yb^{3+}:$NaYF_4$ nanophosphor to CdSe quantum dots. *Journal of Physical Chemistry C* **114**, 17535-17541 (2010).

295 Ostermayer, F. W., van der Ziel, J. P., Marcos, H. M., Van Uitert, L. G., Geusic, J. E. Frequency Upconversion in YF_3: Yb^{3+},Tm^{3+}. *Physical Review B* **3**, 2698 (1971).

296 Yin, A., Zhang, Y., Sun, L., Yan, C. Colloidal synthesis and blue based multicolor upconversion emissions of size and composition controlled monodisperse hexagonal $NaYF_4$: Yb,Tm nanocrystals. *Nanoscale* **2**, 953-959 (2010).

297 David F., Underwood, T. K., Rosenthal, S. J. Ultrafast carrier dynamics in CdSe nanocrystals determined by femtosecond fluorescence upconversion spectroscopy. *Journal of Physical Chemistry B* **105** (2001).

298 Chen, J., Guo, C., Wang, M., Huang, L., Wang, L., Mi, C., Li, J., Fang, X., Mao, C., Xu, S. Controllable synthesis of NaYF4:Yb,Er upconversion nanophosphors and their application to *in vivo* imaging of Caenorhabditis elegans. *Journal of Materials Chemistry* **21**, 2632-2638 (2011).

299 Hribar, K. C., Lee, M. H., Lee, D., Burdick, J. A. Enhanced release of small molecules from near-infrared light responsive polymer-nanorod composites. *ACS Nano* **5**, 2948-2956 (2011).

300 Kennedy, L. C., Bickford, L. R., Lewinski, N. A., Coughlin, A. J., Hu, Y., Day, E. S., West, J. L., Drezek, R. A. A new era for cancer treatment: Gold-nanoparticle-mediated thermal therapies. *Small* **7**, 169-183 (2011).

301 Tong, L., Zhao, Y., Huff, T. B., Hansen, M. N., Wei, A., Cheng, J. X. Gold nanorods mediate tumor cell death by compromising membrane integrity. *Advanced Materials* **19**, 3136-3141 (2007).

302 Wang, C., Chen, J., Talavage, T., Irudayaraj, J. Gold Nanorod/Fe3O4 nanoparticle "nano-pearl- necklaces" for simultaneous targeting, dual-mode imaging, and photothermal ablation of cancer cells. *Angewandte Chemie - International Edition* **48**, 2759-2763 (2009).

303 Lu, W., Singh, A. K., Khan, S. A., Senapati, D., Yu, H., Ray, P. C. Gold nano-popcorn-based targeted diagnosis, nanotherapy treatment, and in situ monitoring of photothermal therapy response of prostate cancer cells using surface-enhanced raman spectroscopy. *Journal of the American Chemical Society* **132**, 18103-18114 (2010).

304 Kang, H., Trondoli, A. C., Zhu, G., Chen, Y., Chang, Y. J., Liu, H., Huang, Y. F., Zhang, X., Tan, W. Near-infrared light-responsive core-shell nanogels for targeted drug delivery. *ACS Nano* **5**, 5094-5099 (2011).

305 Anpo, M., Takeuchi, M. The design and development of highly reactive titanium oxide photocatalysts operating under visible light irradiation. *Journal of Catalysis* **216**, 505-516 (2003).

306 Rozhkova, E. A., Ulasov, I., Lai, B., Dimitrijevic, N. M., Lesniak, M. S., Rajh, T. A High-performance nanobio photocatalyst for targeted brain cancer therapy. *Nano Letters* **9**, 3337-3342 (2009).

307 Song, Y. Y., Schmidt-Stein, F., Bauer, S., Schmuki, P. Amphiphilic TiO2 nanotube arrays: An actively controllable drug delivery system. *Journal of the American Chemical Society* **131**, 4230-4232 (2009).

308 Bogdan, N., Vetrone, F., Ozin, G. A., Capobianco, J. A. Synthesis of ligand-free colloidally stable water dispersible brightly luminescent lanthanide-doped upconverting nanoparticles. *Nano Letters* **11**, 835-840 (2011).

309 Heer, S., Kömpe, K., Güdel, H. U., Haase, M. Highly efficient multicolour upconversion emission in transparent colloids of lanthanide-doped $NaYF_4$ nanocrystals. *Advanced Materials* **16**, 2102-2105 (2004).

310 Li, C., Wang, F., Zhu, J., Yu, J. C. NaYF4:Yb,Tm/CdS composite as a novel near-infrared-driven photocatalyst. *Applied Catalysis B: Environmental* **100**, 433-439 (2010).

311 Derfus, A. M., Chan, W, C. W., Bhatia, S. N. Probing the cytotoxicity of semiconductor quantum dots. *Nano Letters* **4**, 11-18 (2003).

312 Kennedy, L. C., Bickford, L. R., Lewinski, N. A., Coughlin, A. J., Hu, Y., Day, E. S., West, J. L., Drezek, R. A. A new era for cancer treatment: gold-nanoparticle-mediated thermal therapies. *Small* **7**, 169-183 (2011).

313 Kho, Y. K., Iwase, A., Teoh, W. Y., Mädler, L., Kudo, A., Amal, R. Photocatalytic H_2 evolution over TiO_2 nanoparticles. the synergistic effect of anatase and rutile. *The Journal of Physical Chemistry C* **114**, 2821-2829, doi:10.1021/jp910810r (2010).

314 Zhu, P., Tan, M., Huang, R. L., Tan, C., Chong, H., Pal, M., Lam, C., Boukamp, P., Pan, J., Tan, S., Kersten, S., Li, H., Ding, J., Tan, N. Angiopoietin-like 4 Protein Elevates the Prosurvival Intracellular O_2:H_2O_2 Ratio and Confers Anoikis Resistance to Tumors. *Cancer Cell* **19**, 401-415 (2011).

315 Shrestha, N. K., Macak, J. M., Schmidt-Stein, F., Hahn, R., Mierke, C. T., Fabry, B., Schmuki, P. Magnetically guided titania nanotubes for site-selective photocatalysis and drug release. *Angewandte Chemie International Edition* **48**, 969-972 (2009).

316 Choi, J. S., Lee, J. H., Shin, T. H., Song, H., Kim, E. Y., Cheon, J. Self-confirming "AND" logic nanoparticles for fault-free MRI. *Journal of the American Chemical Society* **132**, 11015-11017 (2010).

317 Laura C. K., Lissett R. B, N. A. L., Andrew J. C., Hu, Y., Day, E. S., West J. L., Drezek, R. A. A New Era for Cancer Treatment: Gold-Nanoparticles-Mediated Thermal Therapies. *Small* **7**, 169-183 (2011).

318 Drynda, A., Deinet, N., Braun, N., Peuster, M. Rare earth metals used in biodegradable magnesium-based stents do not interfere with proliferation of smooth muscle cells but do induce the upregulation of inflammatory genes. *Journal of Biomedical Materials Research - Part A* **91**, 360-369 (2009).